

FORMING LIMIT IMPROVEMENT OF AZ31 MAGNESIUM SHEET

FORMING LIMIT IMPROVEMENT OF AZ31 MAGNESIUM SHEET AT ROOM TEMPERATURE USING PRESTRAIN ANNEALING

By

CHENHUI NIU, B. Eng

A Thesis

Submitted to the School of Graduate Studies

In Partial Fulfillment of the Requirements

For the Degree of

Masters of Applied Science

McMaster University

©Copyright by Chenhui Niu, 2014

Master of Applied Science
(Mechanical Engineering)

McMaster University
Hamilton, Ontario

TITLE:

FORMING LIMIT IMPROVEMENT OF
AZ31 MAGNESIUM SHEET AT ROOM
TEMPERATURE USING PRESTRAIN
ANNEALING

AUTHOR:

Chenhui Niu

SUPERVISOR:

Dr. Mukesh K. Jain, Professor,
Department of Mechanical Engineering

NUMBER OF PAGES:

xiii, 107

ABSTRACT

The formability of automotive magnesium sheet at room temperature is limited due to its HCP crystalline structure with limited slip systems. To improve the formability at room temperature, a new method of pre-strain annealing and subsequent forming (PASF) has been assessed. Uniaxial tensile tests are conducted on fully annealed AZ31 sheets as well as on a range of pre-strain annealed samples at an annealing temperature of 250°C . The test data is used to characterize improvements to tensile elongations as well as changes in the work hardening behaviour arising from the PASF process as well as for prediction of forming limit diagrams.

The formability improvements from PASF process are further assessed by conducting interrupted hemispherical punch stretching tests at room temperature, annealing, and then continuing the dome stretching process to fracture. Several different specimen geometries are tested to analyze the punch load versus punch displacement characteristics. Further, the tests are used to construct the room temperature forming limit diagrams (FLD) of fully annealed sheets as well as PASF process dome samples. The improvement in limit strain by PASF process is strongly dependent on the pre-strain, annealing temperature and time. An improvement of 20% in limit strain values could be achieved with one annealing step under optimized conditions of annealing and pre-straining. Experimental FLDs are also compared with theoretical FLDs based on well-known Marciniak-Kuczynski (M-K) analysis and an existing anisotropic yield

criterion with appropriate modifications for anisotropic characteristics and changes in the work hardening behavior of AZ31 sheet from the PASF process. The M-K theory is also used to calculate FLD of AZ31 sheet at 300°C and compared with an existing FLD determined in the McMaster Metal Forming Laboratory. Domes test samples are also examined by optical metallography to rationalize the differences in fracture behavior of fully annealed and PASF samples.

ACKNOWLEDGEMENTS

I wish to express my sincerest gratitude to my supervisor Dr. Mukesh Jain for his inspiring advice, patient instruction and motivational encouragement. I am greatly thankful to Dr. Mike Bruhis and Ms. Connie Barry for their laboratory assistance with many heat treatments. Many thanks also go to General Motors of Canada and McMaster University for research funding and financial support.

I would like to thank the Mechanical Engineering technical staff members Jim McLaren and Michael Lee for their patience and assistance in helping me with machining of the test specimens. I am also thankful to the Materials Science Engineering technical staff members, Doug Culley and Xiaogang Li, for their assistance in microstructural analysis. Many thanks to my colleagues Guowei Zhou, Peng Zhang and Hadi Noori in the metal forming research group for their support and selfless help.

Finally, special thanks to my parents and my wife for their understanding, support and encouragement.

TABLE OF CONTENTS

ABSTRACT	III
ACKNOWLEDGEMENTS	V
CHAPTER 1 INTRODUCTION	1
1.1 BACKGROUND	1
1.2 LITERATURE REVIEW	2
1.2.1 Material	2
1.2.2 Forming Limit Diagram	4
1.2.3 Methods for Prediction of FLCs of Sheet Materials	9
1.3 OBJECTIVES	12
1.4 ORGANIZATION OF THE THESIS	13
CHAPTER 2	
ASSESSMENT OF PASF PROCESS FOR BASIC	
FORMABILITY IMPROVEMENT OF AZ31 MAGNESIUM SHEET AT ROOM TEMPERATURE	
.....	14
2.1 INTRODUCTION	14
2.2 EXPERIMENTAL METHODOLOGY	16
2.2.1 Annealing.....	16
2.2.2 Hemispherical Punch Stretching Tooling (HPS)	17
2.2.3 HPS Test Procedure	19
2.2.4 Limit Dome Height (LDH) Measurement	20
2.2.5 Specimen Preparation for Optical Microscopic Observations	22
2.2.6 Average Grain Size Measurement.....	23
2.3 RESULTS AND DISCUSSION.....	24
2.3.1 Hemispherical Punch Stretching Tests	24
2.3.2 Microstructure Observation.....	27
2.4 SUMMARY	31
CHAPTER 3 EXPERIMENTAL DETERMINATION OF FORMING LIMIT DIAGRAMS OF	
ANNEALED AND PASF PROCESSED AZ31 SHEET	32
3.1 INTRODUCTION	32
3.2 EXPERIMENTAL METHODOLOGY	34
3.2.1 Test Sample Preparation.....	34
3.2.2 Determination of Pre-strain.....	36
3.2.3 Test Equipment and Test Details.....	40
3.2.4 Strain Measurement.....	42
3.2.5 Procedures for FLD Determination.....	45
3.3 RESULTS AND DISCUSSION.....	46
3.3.1 Punch Load Versus Displacement Characteristics	46

3.3.2	<i>FLD of Fully Annealed AZ31 Mg Sheet</i>	52
3.3.3	<i>FLD of PASF Processed AZ31 Mg Sheet</i>	53
3.3.4	<i>Fracture Characteristics</i>	55
3.4	SUMMARY	57
CHAPTER 4 THEORETICAL DETERMINATION OF FLD OF AZ31 SHEET AT ROOM TEMPERATURE		58
4.1	INTRODUCTION	58
4.2	MARCINIAK-KUCZYNSKI (M-K) MODEL	60
4.2.1	<i>Basic Mechanics</i>	60
4.2.2	<i>Yield Model</i>	63
4.2.3	<i>Constitutive Model</i>	64
4.3	DETERMINATION OF M-K MODEL INPUT PARAMETERS	65
4.3.1	<i>Determination of Yield Model Parameter</i>	65
4.3.2	<i>Determination of Constitutive Model Parameters</i>	71
4.3.3	<i>Determination of Surface Roughness</i>	72
4.4	M-K THEORY NUMERICAL IMPLEMENTATION.....	73
4.5	RESULTS AND DISCUSSION.....	78
4.5.1	<i>Effect of Various Parameters on FLD Characteristics</i>	78
4.5.1.1	Effect of Inhomogeneity factor (or f-value).....	78
4.5.1.2	Effect of Groove Orientation	81
4.5.1.3	Effect of r-value	84
4.5.2	<i>FLD Prediction of Fully-annealed AZ31 Mg</i>	86
4.5.3	<i>FLD Prediction of PFSA AZ31 Mg</i>	87
4.6	CONCLUSION	88
CHAPTER 5 THEORETICAL PREDICTION OF FLD OF AZ31 MAGNESIUM SHEET AT HIGHER TEMPERATURES		90
5.1	INTRODUCTION	90
5.2	REVISED CALCULATION FOR HIGH TEMPERATURE FLD DETERMINATION	90
5.3	RESULTS AND DISCUSSION.....	93
5.4	HIGH TEMPERATURE FLC CONCLUSIONS	96
CHAPTER 6 CONCLUSIONS		97
FUTURE WORK		100
REFERENCES		102

LIST OF FIGURES

FIGURE 1.1. A TYPICAL FLD OF STEEL SHEETS [13].	5
FIGURE 1.2. NAKAZIMA TEST SETUP.....	6
FIGURE 1.3. MARCINIAK METHOD TEST SETUP [20].....	7
FIGURE 1.4. FLCs OF AZ31 MG AT DIFFERENT TEMPERATURES DETERMINED FROM (A) KIM [23] AND (B) ANTONISWAMY [24].	9
FIGURE 2.1. A SCHEMATIC OF HEMISPHERICAL PUNCH TESTS.	14
FIGURE 2.2. FURNACE USED FOR ANNEALING OF MATERIAL.....	17
FIGURE 2.3. HPS TEST SET-UP, (A) TOOLING UTILIZED FOR HEMISPHERICAL PUNCH TESTS, AND (B) PRESS WITH HPS TOOLING.	18
FIGURE 2.4. A SCHEMATIC REPRESENTATION FOR EACH MODE OF HEMISPHERICAL PUNCH STRETCHING TESTS, (A) MODE 1, (B) MODE 2, (C) MODE 3, AND (D) MODE 4.....	20
FIGURE 2.5. LDH MEASUREMENT EQUIPMENT DETAILS, (A) SET-UP FOR LDH MEASUREMENT, (B) CLOSE-UP OF THE SPECIMEN AND THE DIAL INDICATOR REGION, AND (C) SCREEN DISPLAY SHOWING DIAL INDICATOR DATA.	21
FIGURE 2.6. A DOME SPECIMEN SHOWING CUT REGIONS FOR MICROSTRUCTURAL EXAMINATION.....	22
FIGURE 2.7. OPTICAL MICROSCOPY (NIKON ECLIPSE LV100) USED FOR MICROSTRUCTURE OBSERVATION.....	23
FIGURE 2.8. MEASUREMENT OF AVERAGE GRAIN SIZE.	24
FIGURE 2.9. TYPICAL HEMISPHERICAL PUNCH STRETCHING SAMPLE.....	24
FIGURE 2.10. LDH FOR ALL HEMISPHERICAL PUNCH STRETCHING TESTS.	25
FIGURE 3.1. FRACTURE OF FULLY ANNEALED AZ31 SPECIMEN IN THE LOCK BEAD REGION PRIOR TO PUNCH STRETCHING. THE SPECIMEN WAS CLAMPED USING THE ORIGINAL LOCK-BEAD DESIGN USING AN EXISTING LDH TOOLING IN THE LABORATORY.....	34
FIGURE 3.2. REVISED LOCK-BEAD GEOMETRY AND THE ALUMINUM INSERT FOR FURTHER SOFTENING OF THE RADIUS OF THE LOCK-BEAD (PHOTOGRAPH).	34
FIGURE 3.3. SPECIMEN DIMENSIONS FOR VARIOUS LDH TESTS (IN MM).	36
FIGURE 3.4. A PERIODIC PATTERN OF SOLID DOTS ELECTROCHEMICALLY ETCHED ON A TEST SPECIMEN.	36
FIGURE 3.5. DEFORMED SPECIMENS WITH PRE-STRAIN VALUE OF 70%, 80% AND 90% (FROM LEFT TO RIGHT). SAMPLES TESTED USING POLYURETHANE PAD BETWEEN BLANK AND PUNCH.	38
FIGURE 3.6. LOAD VERSUS DISPLACEMENT TRACES FOR DIFFERENT PRE-STRAIN VALUES. TWO SETS OF CURVES CORRESPOND TO (I) CONTINUOUS PRE-STRAIN TESTS, AND (II) INTERRUPTED TESTS WHERE THE SAMPLES WERE REMOVED FROM THE PRESS FOR ANNEALING.	38
FIGURE 3.7. RELATIONSHIP BETWEEN PRE-STRAIN AMOUNT AND FAILURE DOME HEIGHT.	

.....	39
FIGURE 3.8. FORMABILITY TEST SET UP; A) INTERLAKEN 150-TON PRESS, AND B) TEST CONFIGURATION.	40
FIGURE 3.9. PHOTOGRAPHS OF VARIOUS AZ31 MG SPECIMENS, (A) SIDE VIEW, (B) TOP VIEW.	41
FIGURE 3.10. ARGUS SYSTEM SET-UP.	42
FIGURE 3.11. ILLUSTRATION OF PHOTOGRAMMETRIC PRINCIPLES FOR FULL-FIELD STRAIN MAPPING [42].	43
FIGURE 3.12. SPECIMEN WITH BAR CODES RECORDED BY ARGUS.	43
FIGURE 3.13. SCHEMATIC DIAGRAM OF THE CAMERA MOVEMENT AROUND THE DOME SPECIMENS.	44
FIGURE 3.14. MAJOR STRAIN MAP OF A FULL DOME SPECIMEN.	45
FIGURE 3.15. A CLASSIFICATION SCHEME FOR THE DOTS IN THE NECK OR FRACTURE REGION OF DOME SAMPLES [43].	46
FIGURE 3.16. PUNCH LOAD VERSUS PUNCH DISPLACEMENT TRACES FROM LDH TESTS OF FULLY ANNEALED AZ31 MG, (A) FULL DOME STRETCHING WITH DIFFERENT LUBRICATION CONDITIONS BETWEEN THE PUNCH AND BLANK, (B) NARROWER SPECIMENS.	48
FIGURE 3.17. DOME HEIGHTS DATA FROM DIFFERENT SPECIMEN GEOMETRIES FOR FULLY ANNEALED AZ31 MG.	49
FIGURE 3.18. A FAILED 76.2 MM SAMPLE. THE AREA IN RED CIRCLE INDICATES THE ANTICLASTIC CURVATURE DEVELOPMENT.	49
FIGURE 3.19. PUNCH LOAD VERSUS PUNCH DISPLACEMENT TRACES FROM LDH TESTS OF PRE-STRAIN ANNEALED AZ31 MG; (A) FULL DOME STRETCHING WITH DIFFERENT LUBRICATION CONDITIONS BETWEEN THE PUNCH AND BLANK, (B) NARROWER SPECIMENS.	51
FIGURE 3.20. COMPARISON OF DOME HEIGHTS DATA FROM DIFFERENT SPECIMEN GEOMETRIES FOR ANNEALED AND PRE-STRAIN ANNEALED AZ31 MG.	52
FIGURE 3.21. FLD AND RESULTING FLC (IN ORANGE) FOR FULLY ANNEALED AZ31 MG SHEET.	53
FIGURE 3.22. FLD AND RESULTING FLC (IN ORANGE) FOR PRE-STRAIN ANNEALED AZ31 MG SHEET.	54
FIGURE 3.23. A COMPARISON OF FLCs BETWEEN FULLY ANNEALED AND PRE-STRAIN ANNEALED SPECIMENS.	54
FIGURE 4.1. SCHEMATIC ILLUSTRATION OF A SHEET WITH AN IMPERFECTION.	62
FIGURE 4.2. SCHEMATIC ILLUSTRATION OF GROOVE ORIENTATION [50].	63
FIGURE 4.3. SPECIMEN DIMENSION FOR TENSILE TESTS (IN MM).	66
FIGURE 4.4. TENSILE TEST SET-UP WITH ARAMIS.	67
FIGURE 4.5. ANISOTROPIC COEFFICIENT R-VALUE VERSUS TRUE MAJOR STRAIN FROM TENSILE TEST OF A FULLY ANNEALED SAMPLE.	68
FIGURE 4.6. ANISOTROPIC COEFFICIENT R-VALUE VERSUS TRUE MAJOR STRAIN FROM	

TENSILE TEST SAMPLES WITH DIFFERENT AMOUNT OF PRE-STRAIN.	70
FIGURE 4.7. THE R-VALUE VERSUS TRUE MAJOR STRAIN FOR 14% PRE-STRAIN MATERIAL. BLUE DIAMOND SYMBOLS ARE FOR EXPERIMENTAL RESULTS AND THE RED LINE IS FOR A FIT USING SIGMOIDAL FUNCTION.	70
FIGURE 4.8. TRUE STRESS VERSUS TRUE STRAIN FROM TENSILE TEST SAMPLES WITH DIFFERENT AMOUNT OF PRE-STRAIN.	71
FIGURE 4.9. TRUE STRESS-STRAIN TENSILE RESPONSE FOR FULLY ANNEALED MATERIAL. DOTS ARE FOR EXPERIMENTAL RESULTS AND THE LINE IS FOR CORRELATIONS USING VOCE MODEL.	72
FIGURE 4.10. MEASUREMENTS OF SURFACE ROUGHNESS.	73
FIGURE 4.11. FLOW CHART FOR THE CALCULATIONS OF THEORETICAL FLDS FOR FULLY ANNEALED MATERIAL.	75
FIGURE 4.12. FLOW CHART FOR THE CALCULATIONS OF THEORETICAL FLDS FOR PRE-STRAIN ANNEALED MATERIAL.	77
FIGURE 4.13. TRUE STRAIN VERSUS TIME FOR FULLY ANNEALED MATERIAL. DATA POINT INDICATED BY DOT LINES IS TAKEN AT 90% TIME OF TENSILE TEST.	78
FIGURE 4.14. CALCULATED FLD FOR SAME MATERIAL CONSTANTS BUT ALTERNATIVE F-VALUE.	80
FIGURE 4.15. INFLUENCE OF F-VALUE ON FLD IN (A) EQUI-BIAXIAL TENSION LOADING PATH FROM MARCINIAK [20], AND (B) TENSION-COMPRESSION SIDE FROM LIAN ET AL. [49].	81
FIGURE 4.16. CALCULATED FLD FOR SAME MATERIAL CONSTANTS BUT ALTERNATIVE ORIENTATION OF GROOVE (θ).	83
FIGURE 4.17. VARIATION OF MAJOR STRAIN WITH ORIENTATION OF GROOVE (θ) AT DIFFERENT STRESS RATIO (α).	83
FIGURE 4.18. SLIP-PLANE AROUND A MODE-I CRACK FOR (A) PLANE STRESS AND (B) PLANE STRAIN. IT IS TO BE NOTED THAT THE SHEET THICKNESS IS NOT TO SCALE [64].	84
FIGURE 4.19. CALCULATED FLD FOR SAME MATERIAL CONSTANTS BUT ALTERNATIVE R-VALUE.	85
FIGURE 4.20. INFLUENCE OF R-VALUE ON FLD IN EQUI-BIAXIAL TENSION LOADING PATH FROM MARCINIAK [20].	85
FIGURE 4.21. A COMPARISON BETWEEN CALCULATED AND EXPERIMENTAL FLDS OF FULLY ANNEALED AZ31 MG SHEET.	87
FIGURE 4.22. A COMPARISON BETWEEN CALCULATED AND EXPERIMENTAL FLDS OF PASF PROCESSED AZ31 MG SHEET.	88
FIGURE 5.1. YIELD LOCI OF AZ31 AT 300 °C . TRIANGLE SYMBOLS ARE FOR EXPERIMENTAL RESULTS AND LINES ARE FOR CALCULATED RESULTS.	91
FIGURE 5.2. TRUE STRESS-STRAIN TENSILE RESPONSE FOR FULLY ANNEALED MATERIAL. DOTS ARE FOR EXPERIMENTAL RESULTS AND THE LINE IS FOR FIT SHIDA'S EQUATION.	93

FIGURE 5.3. A COMPARISON BETWEEN CALCULATED AND EXPERIMENTAL FLDS OF AZ31

MG SHEET AT 300°C 94

FIGURE 5.4. CALCULATED FLD FOR SAME MATERIAL CONSTANTS BUT ALTERNATIVE

TEMPERATURES AND STRAIN RATES. 96

LIST OF TABLES

FIGURE 1.1. A TYPICAL FLD OF STEEL SHEETS [13].	5
FIGURE 1.2. NAKAZIMA TEST SETUP.....	6
FIGURE 1.3. MARCINIAK METHOD TEST SETUP [20].....	7
FIGURE 1.4. FLCS OF AZ31 MG AT DIFFERENT TEMPERATURES DETERMINED FROM (A) KIM [23] AND (B) ANTONISWAMY [24].	9
TABLE 3.1. SUMMARY OF LIMIT STRAINS AT VARIOUS LOADING PATHS FOR BOTH FULLY ANNEALED AND PRE-STRAIN ANNEALED AZ31 MG SHEET	55
TABLE 3.2. HIGH MAGNIFICATION IMAGES FROM FRACTURE AND SAFE AREAS.	56
TABLE 5.1. THE VARIATION OF M-VALUE WITH STRAIN RATE AND TRUE STRAIN [79].....	95

LIST OF SYMBOLS

$\bar{\sigma}$	effective true strain
$\sigma_{11}, \sigma_{22}, \sigma_{33}$	true normal stress components in three directions
τ_{12}	true shear stress component
a_1, a_2, a_3	material constants in Voce law
ϵ_w	strain increment in width direction
ϵ_t	strain increment in thickness direction
$\bar{\epsilon}$	effective true strain
$\epsilon_1, \epsilon_2, \epsilon_3$	true strain components in three directions
$\Delta\epsilon_1, \Delta\epsilon_2, \Delta\epsilon_3$	true strain increments in three directions
a_2, b_2, c_2	material constants in sigmoidal function
f	imperfection factor (M-K analysis)
t_0	initial sheet thickness
R_{pv}	peak-to-valley surface roughness
$a_3, b_3, c_3, d_3, e_3, g_3, h_3, m, n$	material constants in Shida`s equation

CHAPTER 1

INTRODUCTION

1.1 Background

Thin gauge formable steel and aluminum sheet constitute a large majority of materials for automotive stamping applications. High strength thin gauge steels and low density aluminum sheets are both being increasingly utilized for weight reduction and consequently to reduce fuel consumption and greenhouse gas emissions. In recent years, there is increasing interest in magnesium sheet as it offers even more weight reduction possibility due to its lower density and higher specific strength compared to both steel and aluminum [1, 2]. Among various wrought magnesium alloys, AZ31 Mg sheet, is most commonly available today. Various research groups around the world are engaged in assessing the processing, microstructure and mechanical properties, including the forming behaviour, of this sheet material. It is now well known that this material has limited formability at room temperature due to its hexagonally closed packed (HCP) crystal structure which offers limited possibility of accommodating large plastic strains of forming operation by dislocation slip. Therefore, much of the research has focussed on high temperature formability of AZ31 sheet. Since cost and formed part quality remain significant impediment to acceptance of AZ31-like wrought magnesium sheet materials, the present study is largely focused on room temperature formability assessment and enhancement of AZ31 magnesium sheet.

1.2 Literature Review

1.2.1 Material

At room temperature, HCP magnesium sheet exhibits poor formability due to limited number of independent active slip systems, where only two basal-slips and one non-basal slip system (twinning) are active. Furthermore, the c/a ratio of Mg is such that deformation is accommodated by twinning and basal slip rather than the prismatic slip. Twinning is a shear deformation process with movement of several unbroken atomic layers and occurs to a limited extent within the grain. Compared to dislocation slip, where fewer atomic bonds are broken, twinning reduces ductility by breaking more atomic bonds [3].

When the temperature is high enough (greater than 200°C), the critical resolved shear stress for non-basal slips system is decreased significantly. Therefore, additional non-basal slips are active, which results in significantly higher formability [4-12]. Presently, magnesium alloys are mainly formed at high temperature (well above 200°C). However, forming at room temperature has some remarkable advantages, such as saving in energy, easier lubrication, higher productivity, and better surface finish.

As the process costs and part quality remain significant issues at high temperature, there is considerable interest in pursuing lower temperature forming methods for Mg sheet. However, before a suitable and commercially viable method for forming Mg sheet at lower temperatures below 150°C can be developed, a basic understanding of the

underlying mechanisms and their relationship to formability limiting processes such as strain localization for a range of strain paths encountered in practice is needed. Grain structure and forming process optimization through well controlled and novel experiments hold the promise of expanding the forming capability of Mg to lower temperatures.

Many researchers have experimentally studied the response of materials to the amount of prior deformation and annealing temperature by following changes in yield strength, tensile strength, uniform and total elongation, and microstructural parameters such as recrystallized grain size. Strength properties of materials typically decrease with rising annealing temperature whereas the plastic properties or ductility of the material improves. Pre-form annealing is a process where a panel is partially formed and then annealed at a pre-determined temperature to eliminate cold work (or strain hardening) from the first step. This intermediate shape with recovered microstructure is subsequently formed to the final shape using the same die. This process has been demonstrated as a feasible process for an aluminum door panel that could not be formed in a single continuous operation. This process will be referred to as Preform Annealing and Subsequent Forming (PASF) process in the rest of this thesis. Such an approach, in principle, can be applied to improve the formability of Mg sheet at ambient temperatures.

In terms of large strain deformation behavior, some data has started to appear in the open literature on true stress versus true strain curves and strain rate sensitivity of AZ31 sheet from uniaxial and hydraulic bulge tests at a range of temperatures (including below

200 °C) and strain rates. Stress-strain curves and strain rate sensitivity are both rather sensitive to grain size, strain rate and temperature as observed for many superplastic materials. Macroscopic strains in the range of 0.25 have been attained for AZ31 at 150 °C (although the value drops to 0.15 at 50 °C). AZ31 alloy tubes deformed at room temperature have yielded strains up to 0.08. The data in the form of LDH and FLD is still scarce at temperatures below 200 °C . In general, however, the LDH and FLDs decrease with a reduction in temperature, and with an increase in strain rate, as typically observed in many wrought sheet materials.

1.2.2 Forming Limit Diagram

While tensile test is a good indicator of formability under uni-axial loading condition, a forming limit diagram (FLD) can describe formability of material under the variety of strain conditions. FLD, also known as forming limit curve (FLC), is perhaps the most accepted measure of formability of sheet materials and is being increasingly used in stamping die design and forming trials to predict excessive thinning or splits in the formed part. By constructing a plot of major versus minor principle strains at the onset of material localized thinning (i.e., necking) under a range of forming conditions such as uniaxial, biaxial and plane strain stretching and drawing, a forming limit curve can be constructed. A schematic of typical forming limit diagram for steel sheet is shown in Figure 1.1. While material can be formed safely with strain conditions below the FLC, it may result in failure to form material with strain state lies above the FLC.

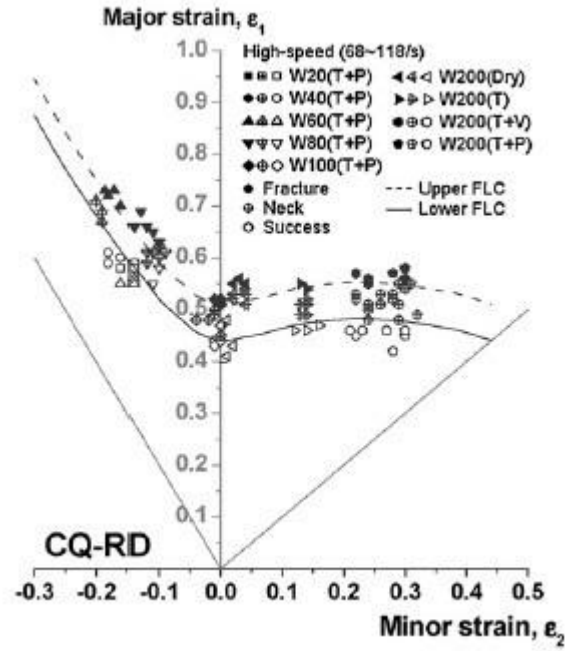


Figure 1.1. A typical FLD of steel sheets [13].

The FLD concept was first developed by Keeler and Backofen in 1964 [14]. By plotting experimental results as two principal strains in Cartesian coordinate system, Keeler and Backofen constructed the right side of FLD ($\epsilon_2 > 0$). This idea was extended by Goodwin in 1968 [15], where the left side of FLD ($\epsilon_2 < 0$) was completed. Since the work of Keeler et al. and Goodwin, many other attempts had been made to obtain experimental FLDs of range of industrially useful sheet materials. Also, the procedure for determining the FLDs has been studied extensively and in recent years much standardization of the test procedure has occurred leading to an ISO standard around FLD related testing and establishment of FLC curves from localized strain region on the sample surface [16]. The ISO standard is based on the work of Hecker [17] and Nakazima [18] who utilized a hemispherical punch, a clamped blank in circular upper and lower

dies with a hole and various specimen geometries to achieve various strain paths to generate the FLD. In Nakazima test, specimens were machined into different width, and then stretched to fracture by using a hemispherical punch (Figure 1.2). By varying the widths of specimen, limit strains locating in the left side of FLD could be obtained. For limit strains in right side of FLD, it could be obtained from full size specimens with different lubrication conditions.

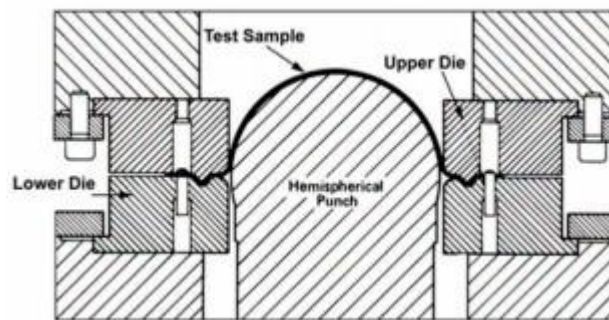


Figure 1.2. Nakazima test setup

The in-plane method to determine FLD was firstly introduced by Marciniak in 1973 [19]. Different from the Hecker and Nakazima methods, where the area of analysis was hemispherical dome, Marciniak test (Figure 1.3) utilized a flat circular punch to deform specimens. A double-blank specimen with the punch side blank consisting of a hole (the so-called driver blank) and the other side consisting of a test blank was utilized. The driver blank was typically made from a more formable material compared to the test blank. This feature combined with the presence of the hole allowed the material of the driver blank to flow outward from the hole and suppress the strain localization or failure of the driver blank and only the failure in the test blank occurred. Additionally, the failure

of the test blank was avoided at the punch profile radius (i.e., in the curved region of the test blank) resulting in the so-called in-plane failure of the sheet under biaxial stretching conditions. As in the case of Hecker's test method, a range of test blank geometries were employed to attain the different strain paths and to construct the entire left and right sides of FLC. Since the region of large strain was kept in flat portion of the test blank during the forming process, deformation could be measured by a single camera, which could not be achieved by Hecker method.

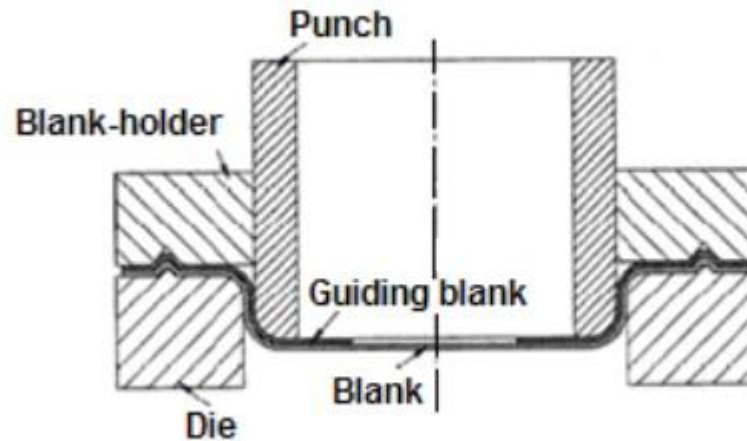


Figure 1.3. Marciniak method test setup [20].

Comparing the two methods of determining experimental FLD, it was widely believed that the forming limits determined from out-of-plane method were higher than those limits from in-plane method. This was caused by the different understandings on these two methods. For the in-plane method, it is generally believed that the localized necking occurs earlier in the unsupported region of the material. For the out-of-plane method of Hecker, however, the hemispherical punch supported dome region of the

deformed blank delays the onset of strain localization giving rise to higher forming limit strains [21].

As stated earlier, much of the work on AZ31 magnesium sheet has been carried out at temperature well above the room temperature where it exhibits good formability and can be used to produce many automotive body panels and other components [22]. In the present work, however, the effort has primarily focused on obtaining room temperature FLD, both experimentally and via the use of a predictive model. Therefore, a brief review of the literature on experimental FLD determination and its prediction for AZ31 sheet is in order. Kim [23] determined the FLCs of AZ31 Mg sheet at various temperatures from 100°C to 300°C as well as at room temperature (Figure 1.4(a)) by the Nakazima test. The results clearly indicate much lower FLCs at room temperature. However, significant improvements in the plane strain limit (or FLD_0 value) as well as over position of FLC do occur at temperature as low as 100°C . It is to be noted that the FLCs in their work do not quite cover the entire strain state up to equi-biaxial tension. Subsequently, Antoniswamy [24] obtained FLDs of AZ31 Mg in the temperatures range 250°C to 450°C by bulge and tensile tests as shown in Figure 1.4(b). The FLCs are highly simplified as they are based on 3 data points corresponding to uniaxial, plane strain and equi-biaxial (bulge) tests. Comparing the FLCs from Kim's and Antoniswamy's work at 300°C , substantial differences are observed in the shape and position of the right side of FLD. Other experimental and predictions of FLC of AZ31 at room temperature in the literature have presented the biaxial tension side of the FLD as a horizontal line to the right of FLD_0

point. Therefore, no consistent results with regard to room temperature FLD of AZ31 sheet are available in the literature.

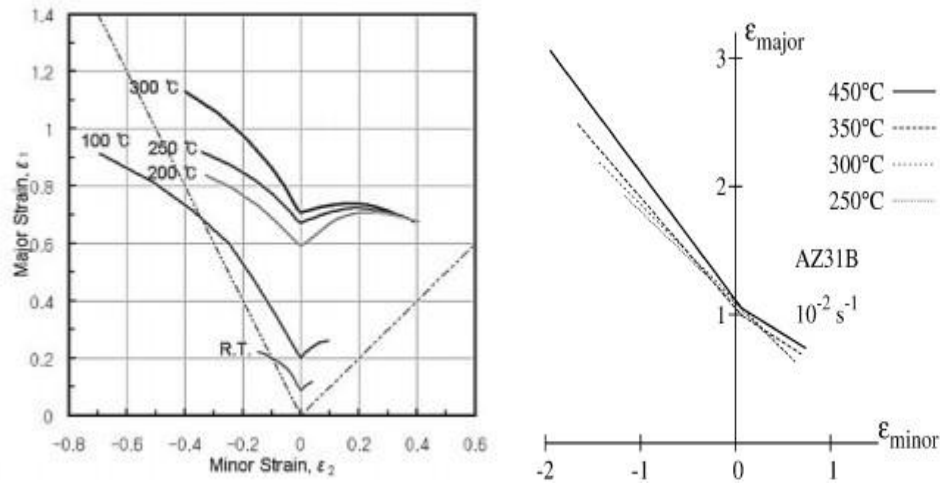


Figure 1.4. FLCs of AZ31 Mg at different temperatures determined from (a) Kim [23] and (b) Antoniswamy [24].

1.2.3 Methods for Prediction of FLCs of Sheet Materials

Due to increased experimental effort and cost of determining FLDs of sheet materials, much effort has been devoted in the literature towards FLD prediction from basic sheet material mechanical properties and applicable constitutive relationship (stress-strain) and yield function of the material. Numerical prediction is attractive not just in terms of overall cost and effort but also because the calculation process can eliminate influence of experimental uncertainties of measurement and analysis [16]. On the other hand, the predictive models still lack suitable material models and accurate mechanics of hemispherical punch stretching process including the punch-sheet contact

conditions arising from sheet and punch surface topography and friction. Consequently, deviations in FLC prediction and experiments are observed even for extensively studied steels and aluminum alloys [25]. Models, however, do offer an opportunity for quite valuable systematic parametric studies of the effect of various material and process parameters on the shape and position of FLCs.

Currently, there are two major methods developed to predict theoretical FLD, finite element method (FEM) and Marciniak-Kuczynski method. The FEM method involves using commercial finite element software such as ABAQUS or DYNA3D to simulate the experimental hemispherical punch stretching process for the various specimen geometries and lubrication conditions until the onset of necking (or fracture), so the corresponding limit strain could be obtained [26]. The data is analyzed in a manner similar to the experiments to yield the FLC. The other more common Marciniak-Kuczynski (or M-K) method is less rigorous and makes many simplifying assumptions. For example, it assumes the existence of a through-thickness groove or imperfection in the starting sheet material and treats the deformation process as an in-plane deformation [20]. In recent years, M-K method has been combined with the FE method to simulate test conditions similar to the experiments [27]. More on the M-K method is discussed in Chapters 4 and 5. However, differences still persist in predicted and experimental FLCs due to limitations of the constitutive model employed as well as from tribological conditions (or friction) assumed at the punch sheet interface in the analysis. Crystal plasticity based approach (in combination with M-K method or FE method) has also been employed for FLC

predictions with varying level of success again due to its inability to suitably incorporate experimental tests conditions such as out of plane deformation and punch-sheet tribological conditions [28, 29]. There is very limited room temperature or high temperature predictive FLCs for AZ31 available in the literature.

In spite of the many limitations of the M-K method as noted above, it is employed in the present work to predict the room temperature and 300 °C FLC of AZ31 sheet. The objective is to see to what extent the experimental FLC curves can be predicted based on this rather efficient and extensively studied method. When choosing between independent FE and M-K methods, the advantage of FEM method results in more accurate results. However, since more factors are included, much more input data is required as well as suitable constitutive materials need to be implemented in the FE code for analysis, which can raise the cost and effort significantly. Furthermore, the FEM method takes much longer time than the M-K method to complete the many simulations that are needed for generating the entire FLC. To compute FLD by a commercial FEM code, one needs to start with implementation of a suitable constitutive model of large deformation into the commercial code (if it does not already exist, which is typically the case for AZ31 sheet), followed by meshing each of the specimen test geometries to create several individual FE models, one for each specimen geometry [26]. For M-K method, one only needs to write one code for computing and the analysis is carried out for a large continuum domain rather than in the discrete and multiple domains of the FE method. While in the FEM method considerable effort is required to simulate and analyze the results to obtain a pair

of limit strains, it is only a matter of few hours for the M-K method to generate the entire FLC. The M-K methodology will be discussed further in detail in Chapters 4 and 5.

1.3 Objectives

A general objective of this present work was to assess the formability of AZ31 Mg. The formability assessment work focuses on studying the effects of pre-forming, annealing, and subsequent forming (i.e., PASF) process with different annealing conditions on the formability of AZ31 Mg at room temperature.

The first objective was to utilize simple yet realistic forming experiments to explore the promise of PASF process. By conducting hemispherical punch tests and comparing limit dome heights, the optimum forming and annealing condition to maximize formability of AZ31 Mg at room temperature could be determined.

The second general objective was to construct detailed experimental FLDs of fully annealed and PASF processed AZ31 Mg at room temperature. This objective was addressed by conducting hemispherical punch tests with different sizes of specimens, and by measuring the major and minor limit strains along different loading paths from the different specimen geometries for the two different ‘processing’ conditions. By comparing the experimental FLCs, one could assess formability improvement from the PASF process, if any.

The last general objective was to study the M-K theory and modify it to calculate theoretical FLDs of AZ31 Mg at room temperature with fully annealed, PASF condition,

and at 300°C . By comparing experimentally determined FLDs and calculated FLDs, the modified M-K theory could be assessed for AZ31.

1.4 Organization of the Thesis

The thesis is organized as follows. It starts with basic assessment of formability of AZ31 Mg sheet at room temperature in Chapter 2. During this process, the optimum PASF conditions to improve formability of AZ31 Mg at room temperature were determined. Chapter 3 presents the work on experimental determination of FLDs of annealed and PASF processed materials. A comparison of FLDs is then made to assess improvement in formability from the PASF process. Chapter 4 presents the details of the modified M-K method for room temperature prediction of FLDs of annealed and PASF processed materials. A comparison of the experimental and predicted FLD is then provided. Further modifications to the M-K method to account for high temperature deformation behaviour of AZ31 sheet are presented in Chapter 5. The new M-K methodology is then utilized to predict the FLD of AZ31 sheet at 300°C . The thesis then presents the conclusion of the research work in Chapter 6.

CHAPTER 2

ASSESSMENT OF PASF PROCESS FOR BASIC FORMABILITY IMPROVEMENT OF AZ31 MAGNESIUM SHEET AT ROOM TEMPERATURE

2.1 Introduction

Hemispherical punch stretching test is perhaps the most common method of assessing the formability of sheet materials. In this test, a sheet is clamped over a circular die opening and stretched using a hemispherical punch that moves perpendicular into clamped sheet and through the circular die opening (Figure 2.1). Dome height at fracture is taken as a measure of formability.

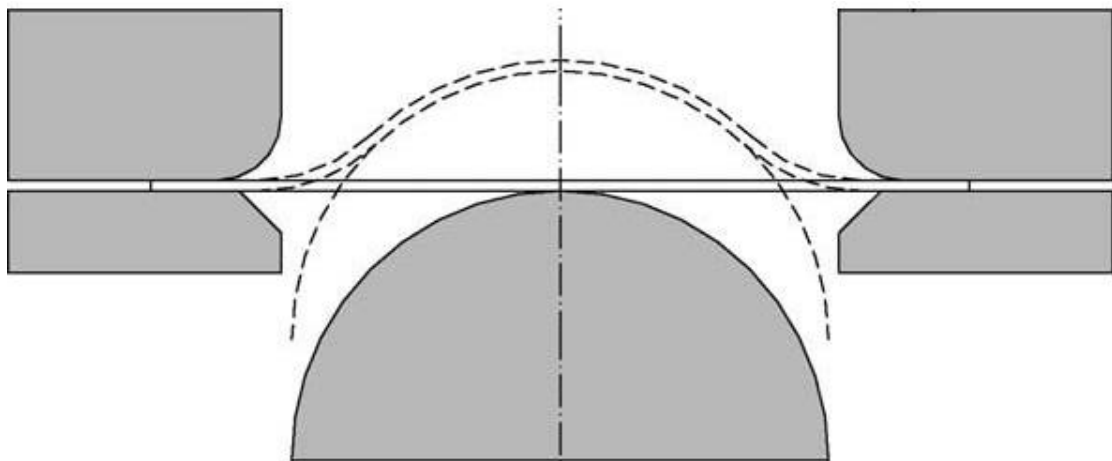


Figure 2.1. A schematic of hemispherical punch tests.

Annealing is one of the most common methods to improve the formability of AZ31 Mg sheet. It involves heating a material to above its critical annealing temperature,

maintaining a suitable temperature, and then cooling to room temperature. Annealing can induce ductility, soften material by significantly reducing dislocation or twin density, relieve internal stresses, refine the structure by making it homogeneous, and improve cold working properties. Since the annealing temperature is one of the most critical factors in annealing, the primary goal of hemispherical punch tests was to test sheet material subjected to various annealing treatments to determine the optimal annealing temperatures to deform magnesium alloy AZ31 at room temperature.

In a previously published paper [30], it has been suggested that reverse stretching of aluminum alloy AA5754-O increases the limit dome height in biaxial stretching mode of deformation. The reverse stretching used in the above paper was a two-step forming process. In the first step, a flat specimen was first formed into a hemispherical dome to a pre-determined height. In the second step, the specimen was reversed (i.e., turned upside down so that punch faced the dome surface from the other direction) and then the deformation was continued till the curvature of the specimen was completely reversed and subsequently onset of necking or failure of the specimen was observed. In the present study, there was interest in assessing the potential of the above two-step punch stretching on AZ31 Mg for improving formability. Thus hemispherical punch stretching tests with pre-stretching (step 1), intermediate annealing and subsequent stretching (step 2) have been conducted to evaluate biaxial tensile stretchability of AZ31 Mg sheet. In order to compare all the possible situations, both forward and reverse stretching were applied in step 2.

2.2 Experimental Methodology

2.2.1 Annealing

The annealing process typically consists of three stages: recovery, recrystallization, and grain growth. The first stage of recovery results in softening of the metal through removal of primarily linear defects. In the subsequent stage of recrystallization, new grains nucleate and grow to replace the previously deformed grains. The last stage consists of grain growth where the recrystallized grains start to coarsen and may cause the material to lose a substantial part of its original strength and diminish ductility of the material. Thus, recovery and recrystallization are the two stages that can improve the formability of material, which should be achieved during annealing. On the other hand, grain growth stage may be detrimental to the formability of material, which should be avoided during annealing. Based on this consideration, a temperature range of 250°C - 400°C was selected as a viable annealing temperature range for AZ31 Mg for investigation and annealing temperatures of 250°C , 300°C and 350°C for 30 minutes and 400°C for 2 hours were selected. For the intermediate-annealing temperature, it has been reported that 400°C is too high for annealed AZ31 Mg, which can result in significant grain growth and decrease the formability of material [31]. Thus, specimens pre-annealed at 400°C were subjected to intermediate-annealing at lower temperatures of 250°C , 300°C and 350°C for 30 minutes. For specimens pre-annealed at temperatures 250°C – 350°C , the intermediate-annealing was done at the same

temperature as their pre-annealing temperatures for 30 minutes.

Annealing atmosphere is another factor that affects the quality of the sheet. Since the as-received AZ31 Mg sheet had been covered by a lubrication layer, which could protect the material from oxidization, annealing could be carried out in ambient air atmosphere inside the furnace (see Figure 2.2). This furnace was equipped with temperature control and measurement capability to within $\pm 1^{\circ}\text{C}$.

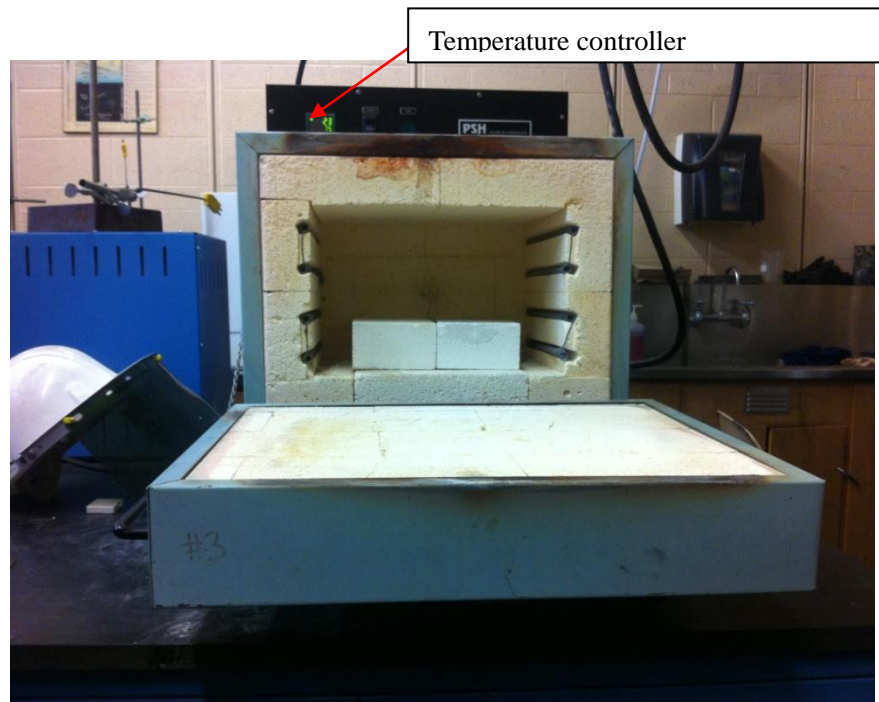


Figure 2.2. Furnace used for annealing of material.

2.2.2 Hemispherical Punch Stretching Tooling (HPS)

HPS tooling available in the laboratory did not allow for reverse stretching of a pre-stretched specimen. Therefore, a new set of tools were designed and fabricated for a small manually operated hand press (Carver laboratory press, load capacity, 25 kips). The

tooling and the press are shown in Figure 2.3 (a) and (b) respectively. Samples tested with this tooling were 127 mm diameter machined disks.

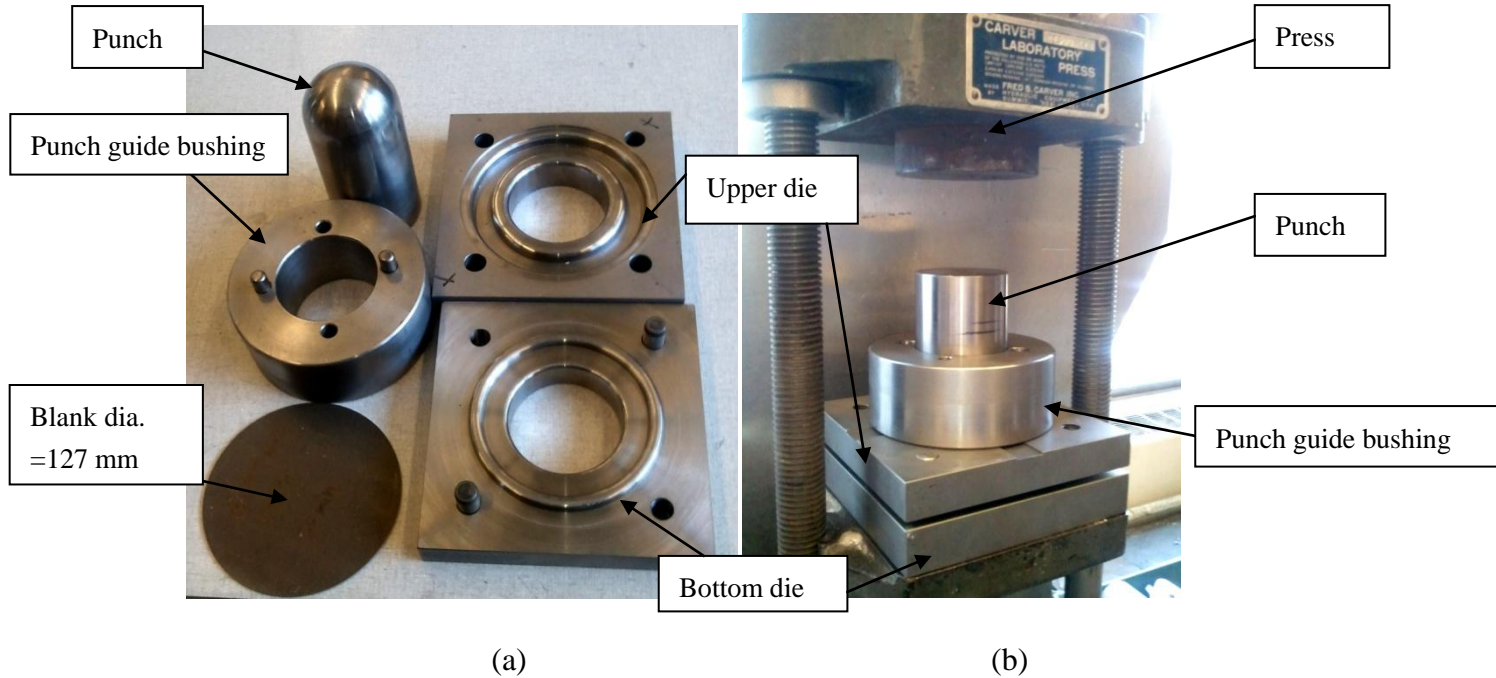


Figure 2.3. HPS test set-up, (a) tooling utilized for hemispherical punch tests, and (b) press with HPS tooling.

To utilize this set of tooling, the first step was to insert a blank in the gap between the upper and lower dies, and place the bottom die on the upper die by aligning the pins in the bottom die with the mating holes in the upper die. The second step was to place the closed dies (without punch) on the press and apply a load of about 22240 N, which resulted in a lock-bead imprint on the blank from the bottom die. A lock bead is utilized to exclude the material outside of the bead in the punch stretching process. The third step involved adding the punch guide bushing to the back side of the upper die, and inserting the punch through the bushing. The last step was to place the whole tooling on the platform of Carver press and operating the press to perform the punch stretching process.

The platform was then pushed upwards during the test so the top flat surface of the punch came in contact with the rigid upper plate of the press and the punch moved downward to stretch the blank into the dome shape. To perform reverse punch stretching, the punch guide bushing was attached to the back side of the bottom die, so the punch could be inserted from the other side and stretch the specimen in reverse direction.

2.2.3 HPS Test Procedure

The hemispherical punch stretching tests were classified into 4 different “modes” as described below:

Mode 1: Annealed blank was stretched in one direction to fracture.

Mode 2: Annealed blank was stretched in one direction to an intermediate dome height (set at 90% of load at fracture in mode 1) then stretched in reverse direction until fracture.

Mode 3: Annealed blank was stretched in one direction to an intermediate dome height (again, 90% of load at fracture in mode 1), annealed at one of 3 temperatures (250°C , 300°C and 350°C) for 30 minutes, and then stretched in reverse direction until fracture.

Mode 4: Annealed blank was stretched in one direction to an intermediate dome height (90% of load at fracture in mode 1), annealed at one of 3 temperatures (250°C , 300°C and 350°C) for 30 minutes, and then stretched in the same direction until fracture.

Schematics of each of the above deformation modes are provided in Figure 2.4.

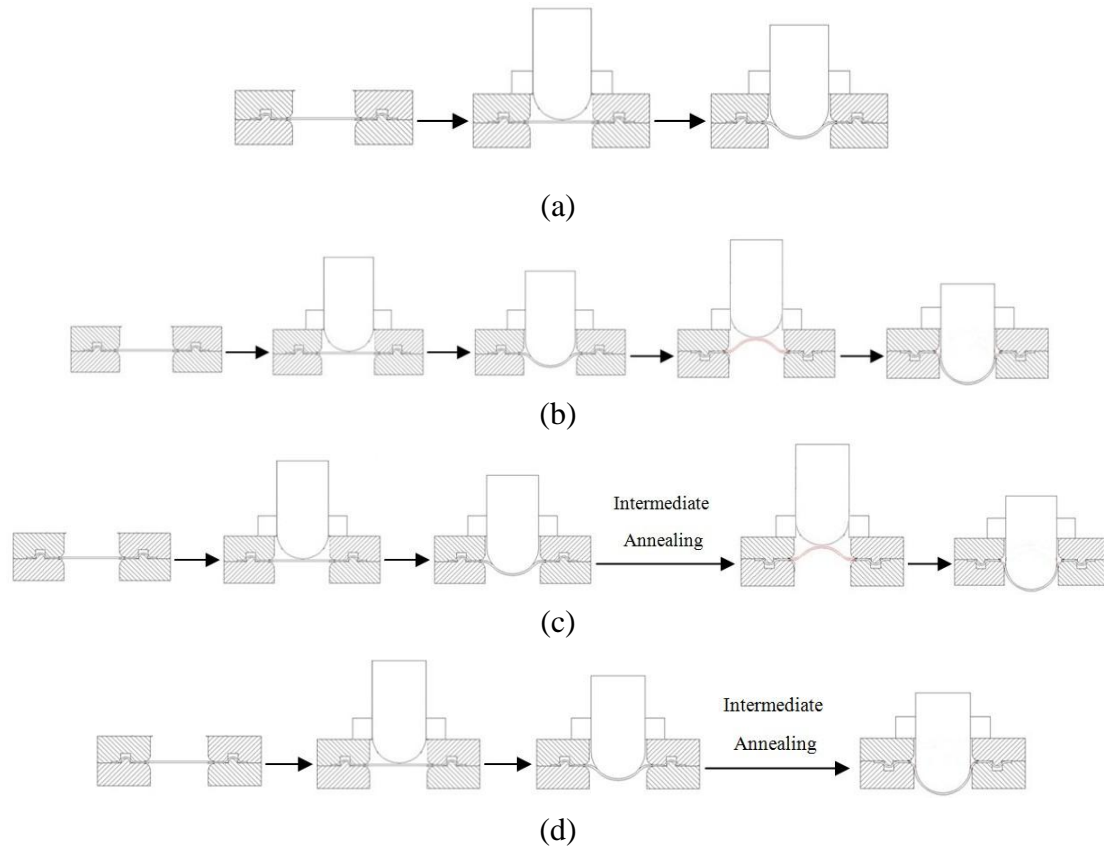
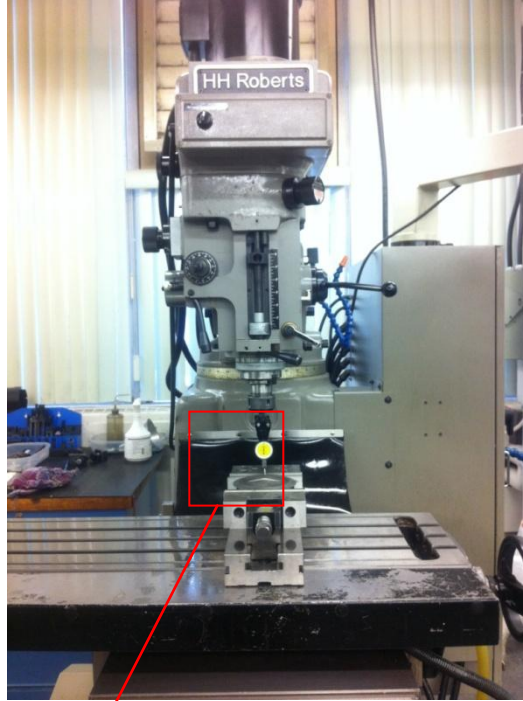


Figure 2.4. A schematic representation for each mode of hemispherical punch stretching tests, (a) mode 1, (b) mode 2, (c) mode 3, and (d) mode 4.

2.2.4 Limit Dome Height (LDH) Measurement

LDH value is perhaps the simplest and quite useful measure of forming performance of sheet materials. To measure the LDH accurately, deformed samples were placed on a milling machine as shown in Figure 2.5 (a). Instead of a milling tool, a micrometer dial indicator was inserted into the tool holder. By moving tip of the dial indicator to bring it into contact with the sample surface, the relative height of the contact point could be read from the digital output screen of the machine as shown in Figure

2.5(c). LDH value was obtained as the difference between the height of the sample at the pole (highest point) and the height of flat region of sample next to the lock bead (lowest point).



(a)



(b)



(c)

Figure 2.5. LDH measurement equipment details, (a) set-up for LDH measurement, (b) close-up of the specimen and the dial indicator region, and (c) screen display showing dial indicator data.

2.2.5 Specimen Preparation for Optical Microscopic Observations

In order to analyze microstructures of the failed samples, each disk was sectioned as shown in Figure 2.6. The slice cut from the sample was cold mounted using a mixture of 25gm epoxy and 3gm hardener. After grinding with silicon carbide discs (600 to 1200 grit in US standard), each sample was polished by 3 μ m and 0.5 μ m cloths with 3 μ m diamond suspension and 0.5 μ m alumina suspensions respectively. After etching with 6% acetic acid (a mixture of 2.1gm picric acid, 3ml acetic acid and 45ml ethanol) for 5 seconds, microstructure of each sample was observed by Nikon Eclipse LV100 optical microscope (Figure 2.7). The microscope had a maximum magnification limit of 100X.

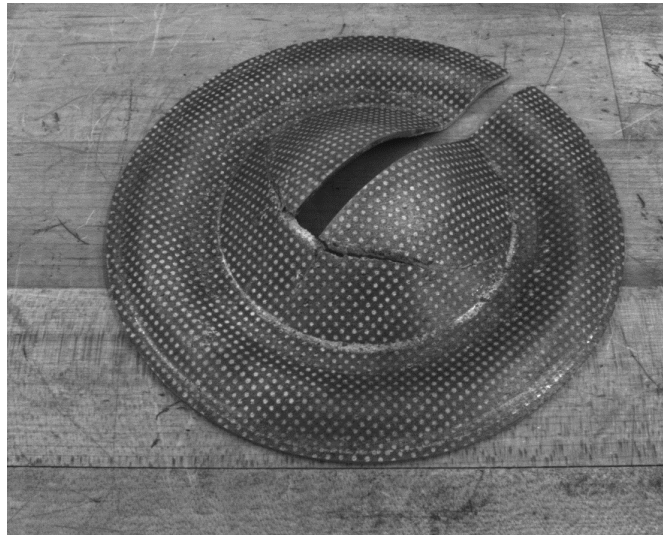


Figure 2.6. A dome specimen showing cut regions for microstructural examination.

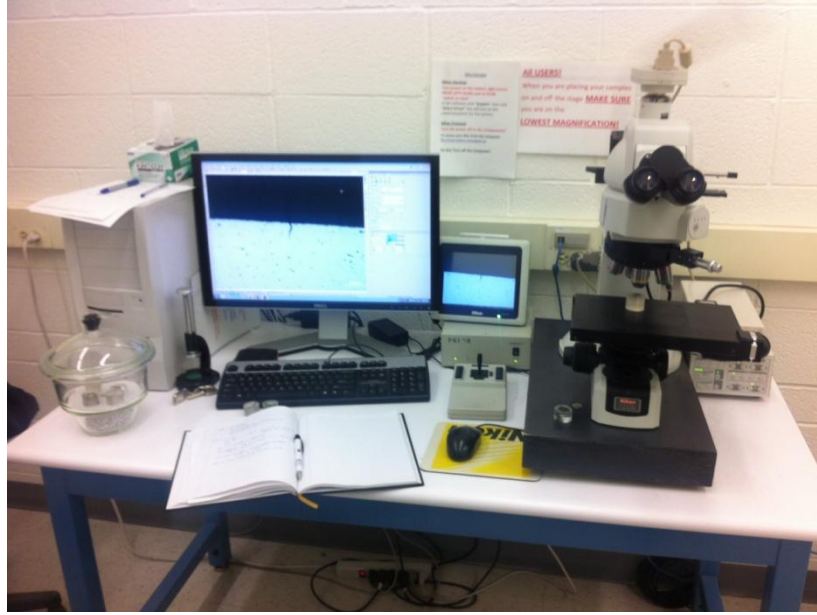


Figure 2.7. Optical microscopy (Nikon Eclipse LV100) used for microstructure observation.

2.2.6 Average Grain Size Measurement

Recorded microstructure images from the optical microscopy were analyzed for grain size. For this purpose, straight lines of length 80 μm were plotted both vertically and horizontally on each microstructure image (Figure 2.8). By counting the number of grains that were intersected by each line, the average grain diameter D was determined from the equation:

$$D = \frac{L}{N}$$

where L equals 1000 μm and N is the number of intercepts which the grain boundary makes with the lines [32].

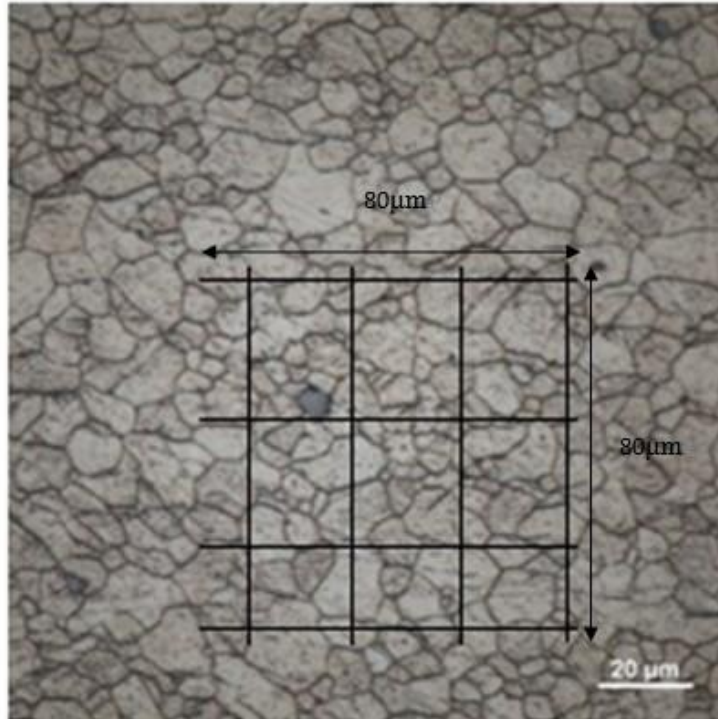


Figure 2.8. Measurement of average grain size.

2.3 Results and Discussion

2.3.1 Hemispherical Punch Stretching Tests

Figure 2.9 shows a typical punch stretched sample. All stretched samples failed by fracture between the pole and the lock bead.

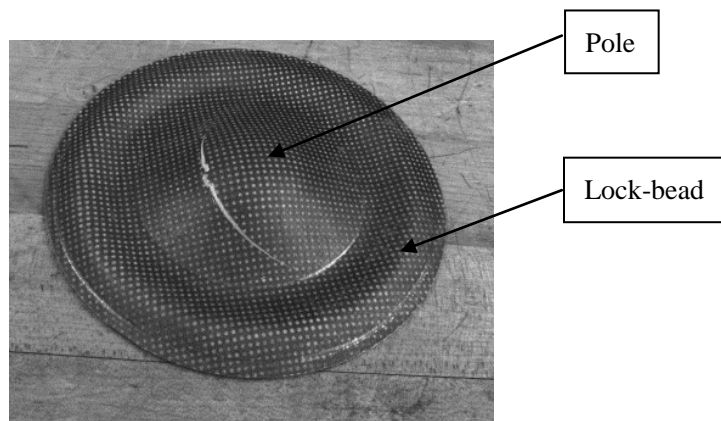


Figure 2.9. Typical hemispherical punch stretching sample.

The results of the hemispherical punch stretching tests are summarized in Table 2.1.

For easier comparison among the different pre-annealing, intermediate-annealing temperatures and deformation modes, the LDH results are also presented as a bar chart in Figure 2.10.

Force applied at fracture for each sample is also presented in Table 2.1. As shown, the force at fracture increased with an increase in the LDH value.

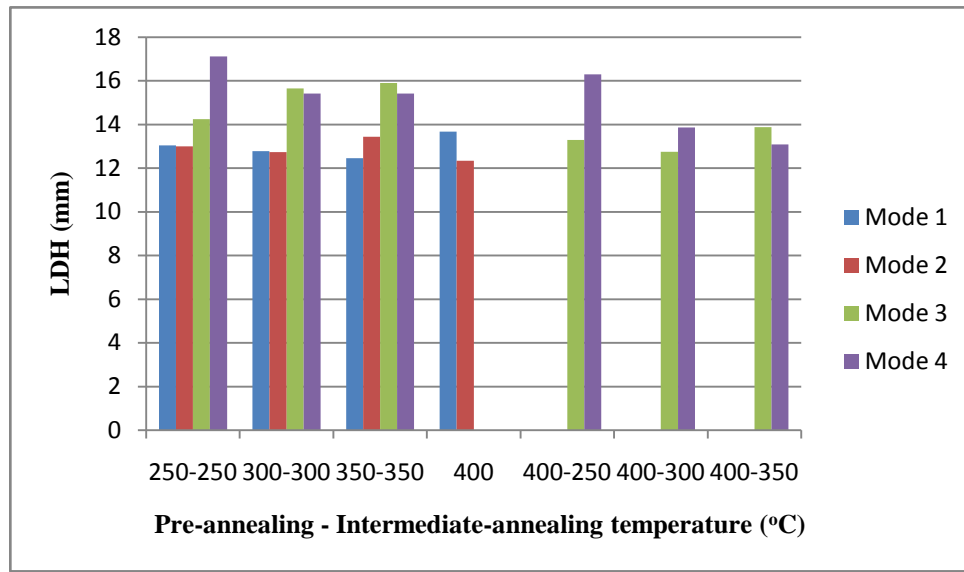


Figure 2.10. LDH for all hemispherical punch stretching tests.

Table 2.1. Hemispherical punch stretching test data for magnesium AZ31.

Pre-annealing Temperature (°C)	Intermediate-annealing Temperature (°C)	Mode 1		Mode 2		Mode 3		Mode 4	
		F _f (kN)	LDH (mm)	F _f (kN)	LDH (mm)	F _f (kN)	LDH (mm)	F _f (kN)	LDH (mm)
250	250	22.69	13.043	21.35	13.005	22.24	14.249	32.03	17.120
300	300	22.24	12.789	21.35	12.738	24.02	15.659	25.35	15.418
350	350	20.46	12.459	22.69	13.437	23.13	15.900	24.02	15.418
400	None	24.91	13.675	16.01	12.344	-	-	-	-
400	250	-	-	-	-	22.24	13.299	30.25	16.297
400	300	-	-	-	-	19.57	12.746	24.02	13.863
400	350	-	-	-	-	23.13	13.884	21.35	13.091

Amongst the samples stretched in mode 1, the one pre-annealed at a temperature of 400°C had the highest LDH value (13.675 mm). However, for samples stretched in mode 2, the one pre-annealed at temperature of 350°C had the highest LDH value (13.437 mm). For one-step punch stretching (mode 1), sample pre-annealed with higher temperature resulted in better formability. For two-step punch stretching without intermediate-annealing, samples pre-annealed in the temperature range 250°C - 350°C showed better formability with an increase in temperature while those pre-annealed above 350°C resulted in reduced formability. The above observations suggest that, for two-step punch stretching, 400°C is too high for any formability improvement in the material. This conclusion was consistent with microstructure observations presented later.

For tests with intermediate-annealing (modes 3 and 4), there was significant increase in the LDH of most samples (pre-annealed below 400°C). This is attributed to the effect of intermediate-annealing on recovery of the microstructure from previous punch stretching. However, samples pre-annealed at 400°C in mode 3 and mode 4 exhibited no significant improvement in their LDH values. Again, this confirmed that pre-annealing at 400°C is not advantageous for formability for two-step stretching with intermediate-annealing (mode 3 and 4) due to significant grain growth.

In the analysis of results of samples stretched in modes 3 and 4, LDH values of samples pre-annealed at 400°C have been compared in order to eliminate effects of different pre-annealing temperatures. In this data set, samples stretched in mode 4 show a decreasing trend with increasing intermediate-annealing temperature, while samples

stretched in mode 3 show variable results with increasing intermediate-annealing temperature. These tendencies illustrate that two-stage stretching in same direction is sensitive to intermediate-annealing temperature, while two-stage reverse stretching is not.

Among LDH results for the different annealing conditions, the largest LDH value resulted from the sample pre-annealed at 250°C , intermediate-annealed at 250°C , and deformed with stretching in the same direction. It was observed that all samples failed rather catastrophically and none could be stopped at the onset of necking. The reason is that AZ31 Mg is more brittle than most formable grades of Al alloy. This could explain why reverse punch stretching could improve the formability of Al alloy but not of AZ31 Mg. For Al alloy, reverse punch stretching enabled a more uniform strain distribution thus delaying the onset of necking and consequently yielding higher LDH values. However, AZ31 Mg, being brittle, failed in bending before necking.

2.3.2 Microstructure Observation

As microstructure is dependent on heat treatment, microstructure images of samples at each of the annealing conditions were recorded and analyzed. Samples stretched in modes 1 and 2 with the same pre-annealing temperature resulted in the same microstructure. Thus, for each annealing condition, only samples stretched in modes 1 and 4 were analyzed for microstructure image. All microstructure images at the location of fracture are shown in Table 2.2 with the average grain size data presented in Table 2.3.

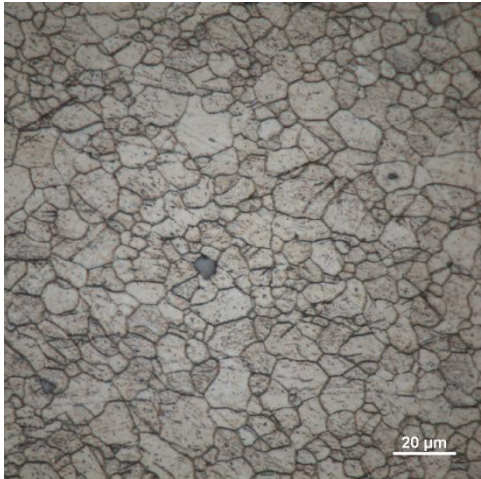
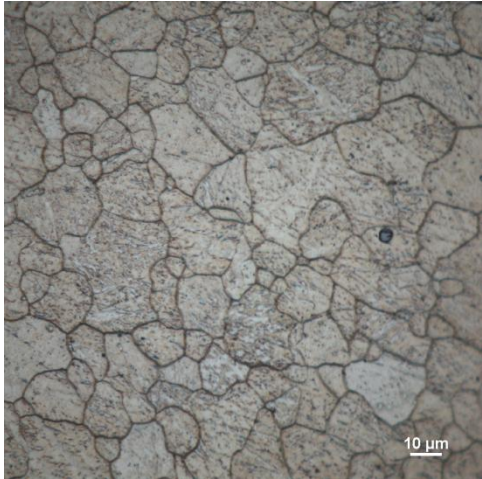
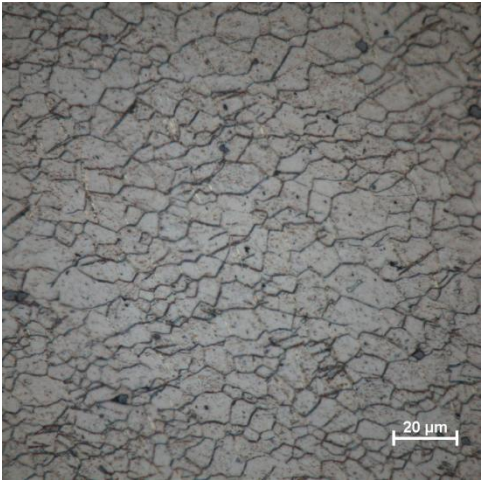
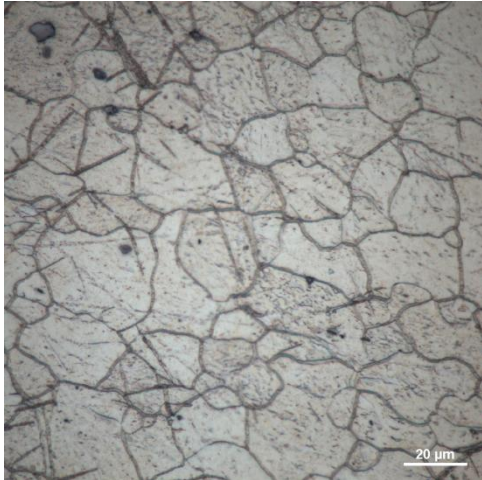
Samples without intermediate-annealing had significantly smaller average grain

size comparing to the intermediate-annealed samples suggesting that grain indeed grew during the annealing process. Another significant difference was the twinning that occurred during HPS process. While some twinning appeared in samples without intermediate-annealing, there was no twinning in the intermediate-annealed samples. This suggests that intermediate-annealing could recover defects (twinning) caused by pre-stretching, which improved the formability of AZ31 sheet.

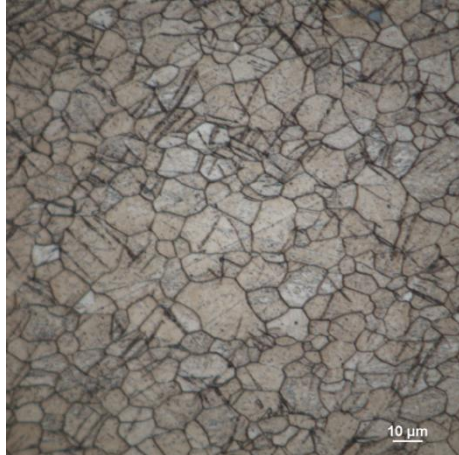
Samples intermediate-annealed at 250°C had the smallest grain size and the most even grain distribution, which resulted in the highest LDH values. This is indicative of the occurrence of grain recrystallization without dramatic grain growth, which made the material stronger and more formable.

Samples intermediate-annealed at 350°C had significantly larger grain size than the other samples. Sample pre-annealed at 400°C and intermediate-annealed at 350°C exhibited significant grain growth and rather large grain sizes compared to the other annealed conditions and resulted in lower LDH values. With pre-annealing at 400°C for 2 hours, grains were fully recrystallized and dramatically grew resulting in lower strength of the material. This also explains why samples with 400°C pre-annealing had smaller LDH values compared to samples stretched in the same mode and intermediate-annealed at the same temperature but pre-annealed at lower temperatures [33-37].

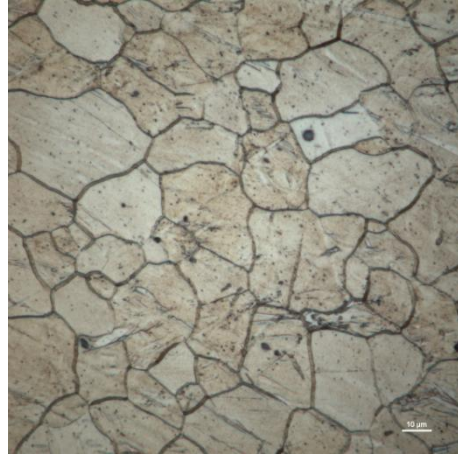
Table 2.2. Microstructure for all samples. The two numbers labeled for each image represent their pre-annealing and intermediate-annealing temperatures.

<p>250 °C - N/A</p> 	<p>250 °C - 250 °C</p> 
<p>300 °C - N/A</p> 	<p>300 °C - 300 °C</p> 

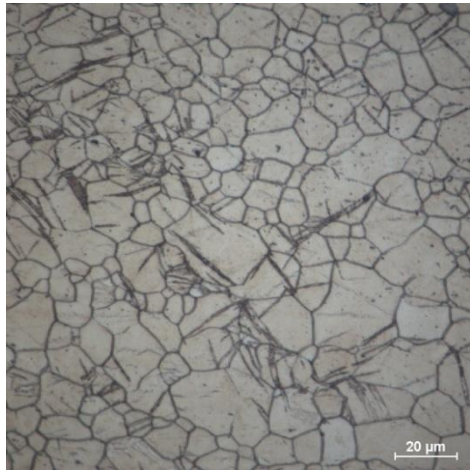
350 °C - N/A



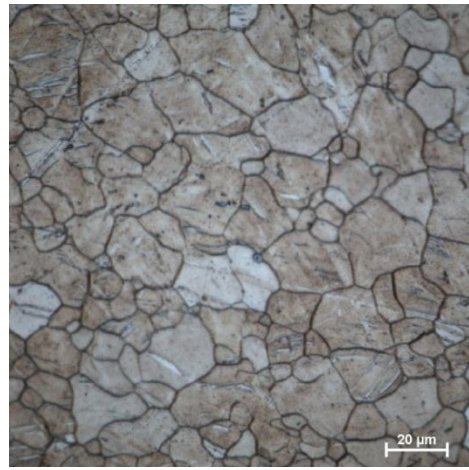
350 °C - 350 °C



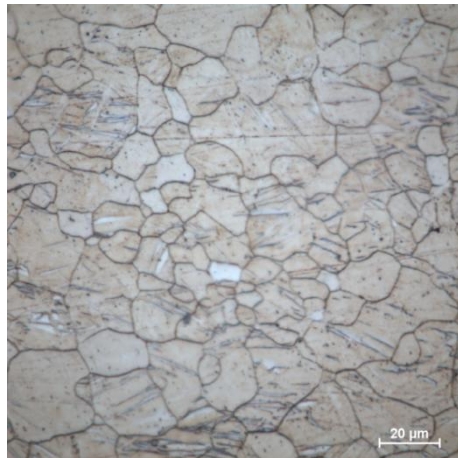
400 °C - N/A



400 °C - 250 °C



400 °C - 300 °C



400 °C - 350 °C

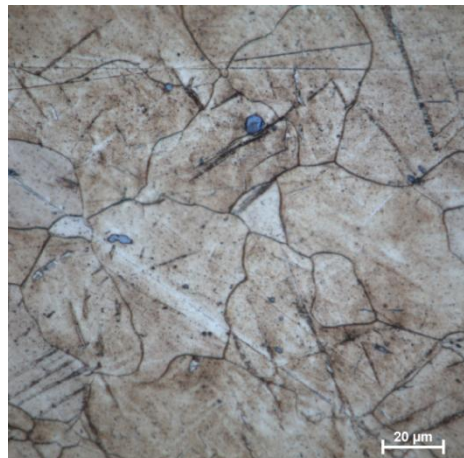


Table 2.3. Measured average grain size of each annealing condition.

Pre-annealing temperature (° C)	Intermediate-annealing temperature (° C)	Average grain size (μm)
250	N/A	7.03
250	250	12.08
300	N/A	8.21
300	300	12.55
350	N/A	8.89
350	350	14.55
400	N/A	9.70
400	250	14.55
400	300	14.55
400	350	30.48

2.4 Summary

A two-step stretching with intermediate-annealing can increase the LDH values of AZ31 sheet significantly. To get maximum LDH, the optimum annealing temperature is 250 ° C , and the optimal method is to impart large pre-strain, intermediate-annealing, and then deform it in the same direction until fracture. There was no significant improvement in LDH values of AZ31 sheet when using the reverse punch stretching method.

The microstructure influences the LDH value significantly. Material with average grain size around 12μm resulted in the maximum LDH value. With 400 ° C annealing following by intermediate-annealing, dramatic grain growth occurred leading to a decreased LDH value.

CHAPTER 3

EXPERIMENTAL DETERMINATION OF FORMING LIMIT DIAGRAMS OF ANNEALED AND PASF PROCESSED AZ31 SHEET

3.1 Introduction

In the last chapter, it was established that the pre-strain annealing and subsequent forming (PASF) process with annealing temperature of 250°C resulted in best formability of AZ31 Mg sheet amongst the 4 different stretching conditions. However, this conclusion was based on hemispherical punch tests on fully clamped circular specimens that were deformed under equi-biaxial loading path. Therefore, further work was continued to assess the performance of PASF process under a broader range of loading paths (biaxial, plane strain and uniaxial). For this purpose, forming limit diagram (FLD) were determined to characterize formability of materials subjected to (i) initial full anneal and (ii) initial full anneal and subsequent anneal after one step of pre-stretching in the form of a full or partial hemispherical domes as discussed below.

The hemispherical punch stretching tests described in Chapter 2 were performed on a small manually operated hand press. Thus there were some limitations to the test. First of all, the stretching speed was not constant due to the manual operation. As AZ31 Mg is strain rate sensitive material, stretching speed could affect the result. Secondly, the load versus displacement data during the deformation process could not be recorded

continuously as no computer control of the test equipment was available. This rather useful data provides not only an assessment of test-to-test reproducibility but also relative formability of sheet materials. Furthermore, as AZ31 Mg was not very ductile at room temperature, the necking in the dome region occurred rather catastrophically. Consequently, the press load needed to be controlled very precisely towards the end of the punch stretching process to stop the test at neck. Last but not least, it was hard to control the pre-strain amount as there was no indicator to show the position of the punch. That was also the reason why the pre-strain amount had been controlled by punch loading but not dome height in the earlier experiments.

For the above reasons, the FLD related dome height testing was carried out on a modern computer-controlled servo-hydraulic forming press (Interlaken Servo-Press 150 Ton). This press was able to provide precise clamping of the sheet in the lock-bead as well as continuous recording of the punch load versus punch displacement traces during the test. However, the existing room temperature tooling for the LDH test for the Servo-Press was designed primarily for aluminum sheet materials and steels. Preliminary LDH experiments using this tooling led to severe fracture of AZ31 sheet at lock-bead in both H24 (strain hardened and partially annealed) and fully annealed conditions as shown in Figure 3.1. Therefore, a new set of upper and lower die plates were designed for AZ31 Mg sheet with a new lock bead design and fabricated as shown in Figure 3.2. These were utilized to conduct LDH tests on gridded blanks to obtain forming limit diagrams.

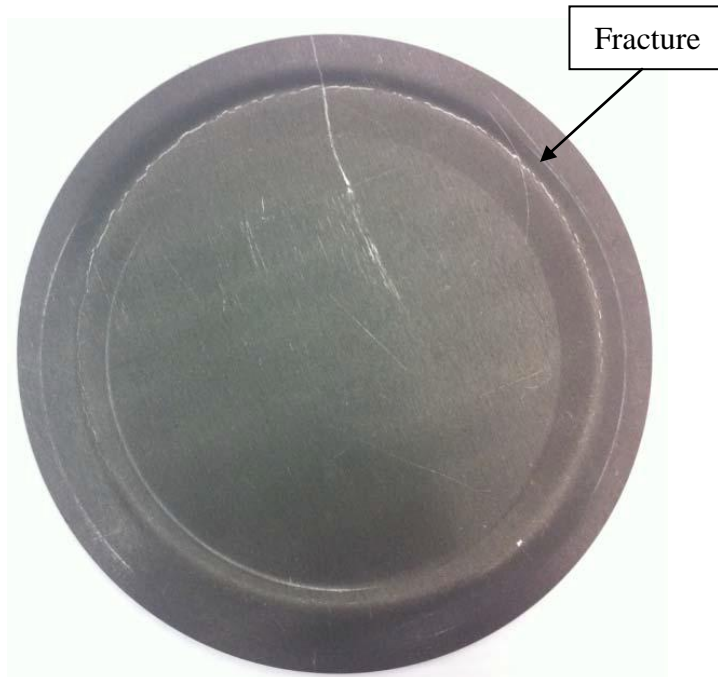


Figure 3.1. Fracture of fully annealed AZ31 specimen in the lock bead region prior to punch stretching. The specimen was clamped using the original lock-bead design using an existing LDH tooling in the laboratory.

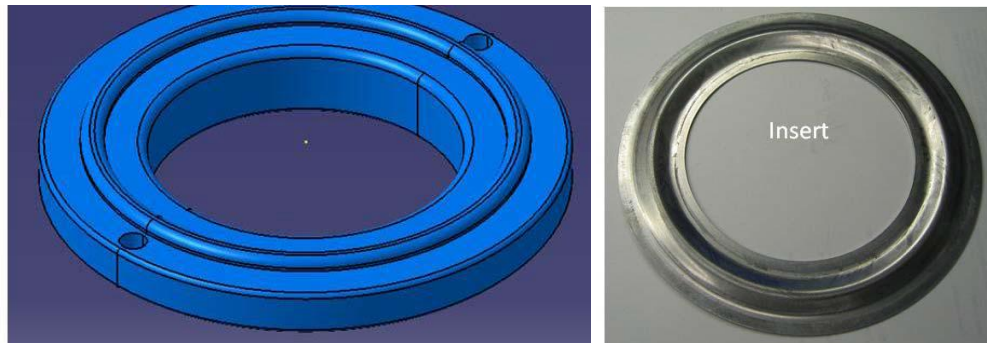


Figure 3.2. Revised lock-bead geometry and the aluminum insert for further softening of the radius of the lock-bead (photograph).

3.2 Experimental Methodology

3.2.1 Test Sample Preparation

The FLDs of AZ31 Mg sheet in the fully annealed and PASF conditions were obtained using the hemispherical punch test tooling proposed by Hecker [17, 38, 39]. The

Hecker method for obtaining FLD uses blank of different widths clamped with a circular lock bead.

Based on the draft ISO standard for the hemispherical punch stretching test, specimens were designed with dimensions shown in Figure 3.3. Specimen widths of 12.7 mm, 50.8 mm, and 76.2 mm (based on standard ASTM B557M-94) in the narrow hour-glass region were used to obtain the strain path in the negative minor strain side of the FLD. Specimen width of 127 mm was used to obtain the strain path closer to the plane strain condition. Circular specimens of 177.8 mm diameter with various lubrication conditions, such as dry, grease, and polyurethane pad between the punch and blank were used to construct the stretch (biaxial tension) side of the FLD (i.e., positive minor strains).

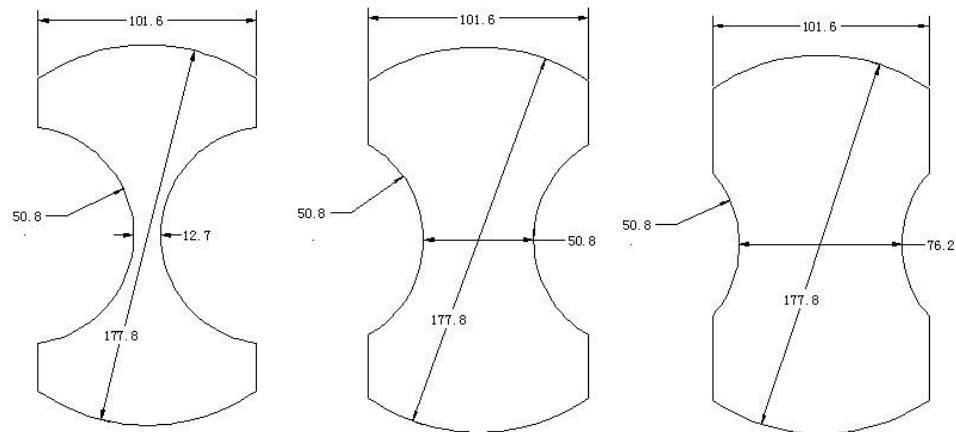


Figure 3.3. Specimen dimensions for various LDH tests (in mm). (Continued on page 36)

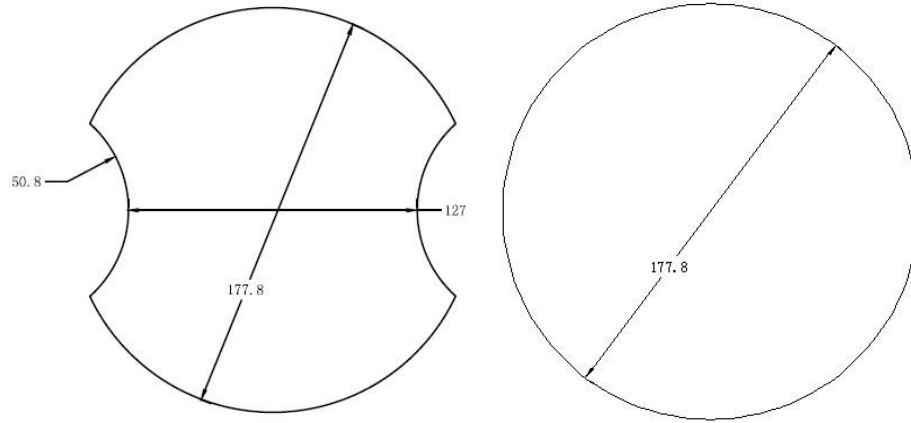


Figure 3.3. Specimen dimensions for various LDH tests (in mm).

A periodic solid dot grid pattern with 2 mm spacing between dots was electrochemically etched using a standard stencil on sheet specimens prior to LDH testing to enable subsequent strain mapping of the dome surface (Figure 3.4).

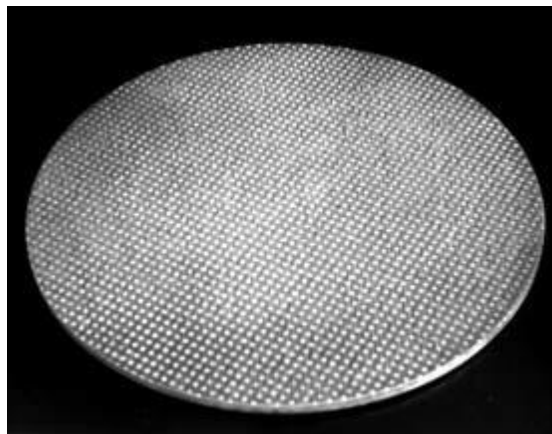


Figure 3.4. A periodic pattern of solid dots electrochemically etched on a test specimen.

3.2.2 Determination of Pre-strain

For FLD of pre-strain annealed AZ31 Mg sheet, the amount of pre-strain is one of the most important variables which could affect the final dome height. The work by

Carter [40] on ZEK100 Mg sheet (similar in composition to AZ31) indicates better formability when the pre-strain amount is large (more than 70% of failure dome height). Thus, 70%, 80% and 90% fracture dome heights were utilized as the pre-strain amounts in the experiments. As the specimen failure location was rather sensitive under bi-axial tension state, the tests were conducted using circular specimens with 38 mm diameter and 2mm thick polyurethane pad placed between blank and top of the punch, which resulted in failure close to the pole of the dome specimen (see Figure 3.5).

The load versus displacement traces are plotted in Figure 3.6. Curves labeled “pre-strain” represent pre-forming loading. After the above pre-forming amounts were reached, the tests were interrupted, and the samples were removed for intermediate-annealing. Curves labeled “pre-strain annealed” represent loading paths of the subsequent stretching. For the pre-formed samples, the load was zero until the punch touched the pre-domed sample at a punch displacement value close to its interrupted value. It is to be noted that the slope of subsequent-stretching curve is higher than the slope of pre-strain curves, which indicates that the material has been softened by the intermediate-annealing. The difference of displacement value between the unloading and reloading points is likely come from the elastic deforming. It could be further verified by measure dome height before and after the annealing.

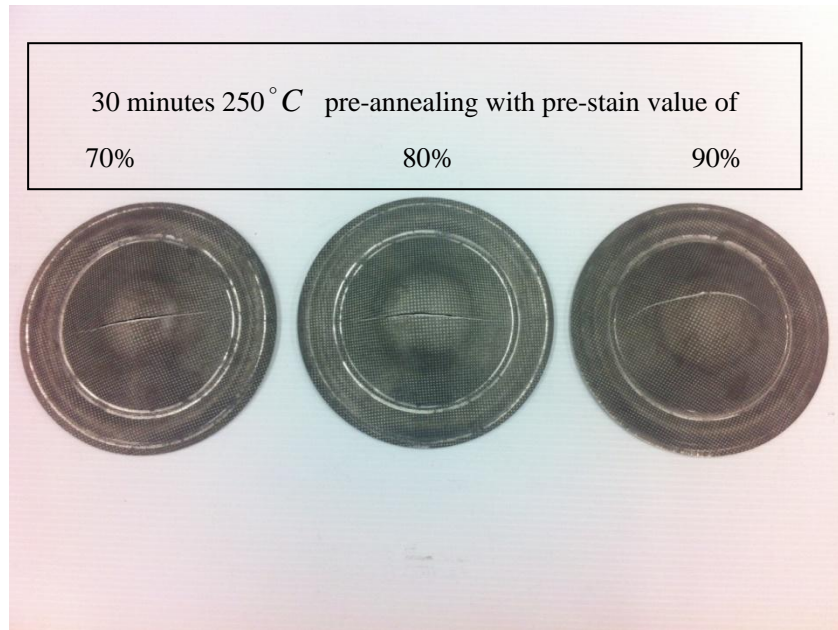


Figure 3.5. Deformed specimens with pre-strain value of 70%, 80% and 90% (from left to right). Samples tested using polyurethane pad between blank and punch.

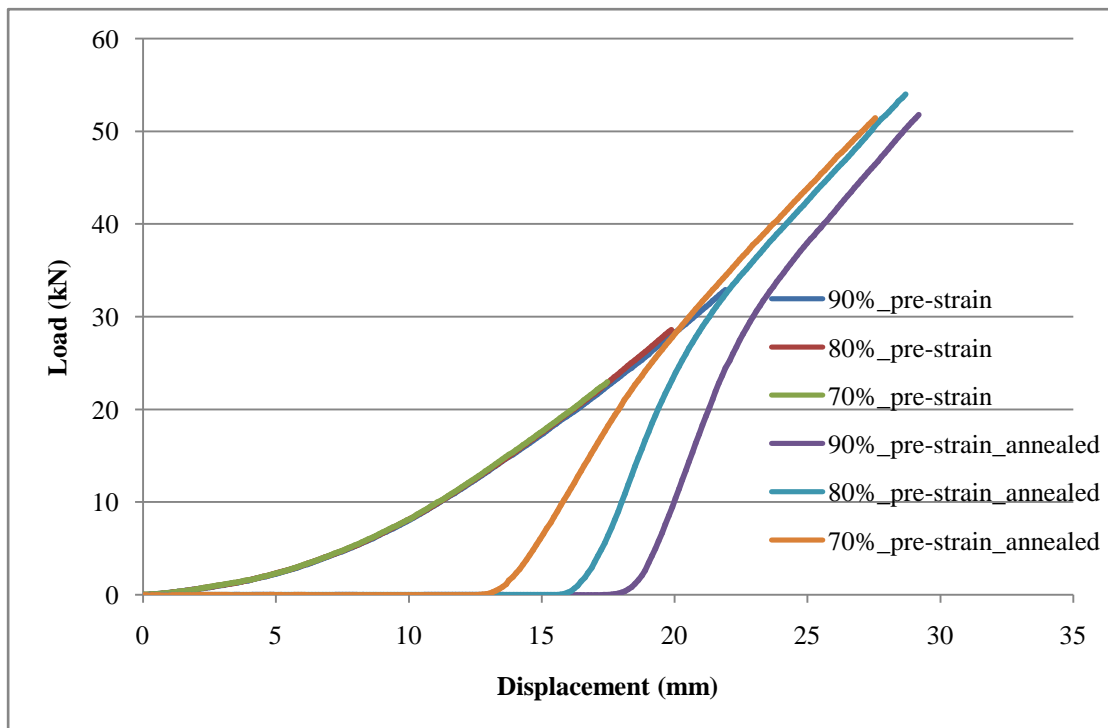


Figure 3.6. Load versus displacement traces for different pre-strain values. Two sets of curves correspond to (i) continuous pre-strain tests, and (ii) interrupted tests where the samples were removed from the press for annealing.

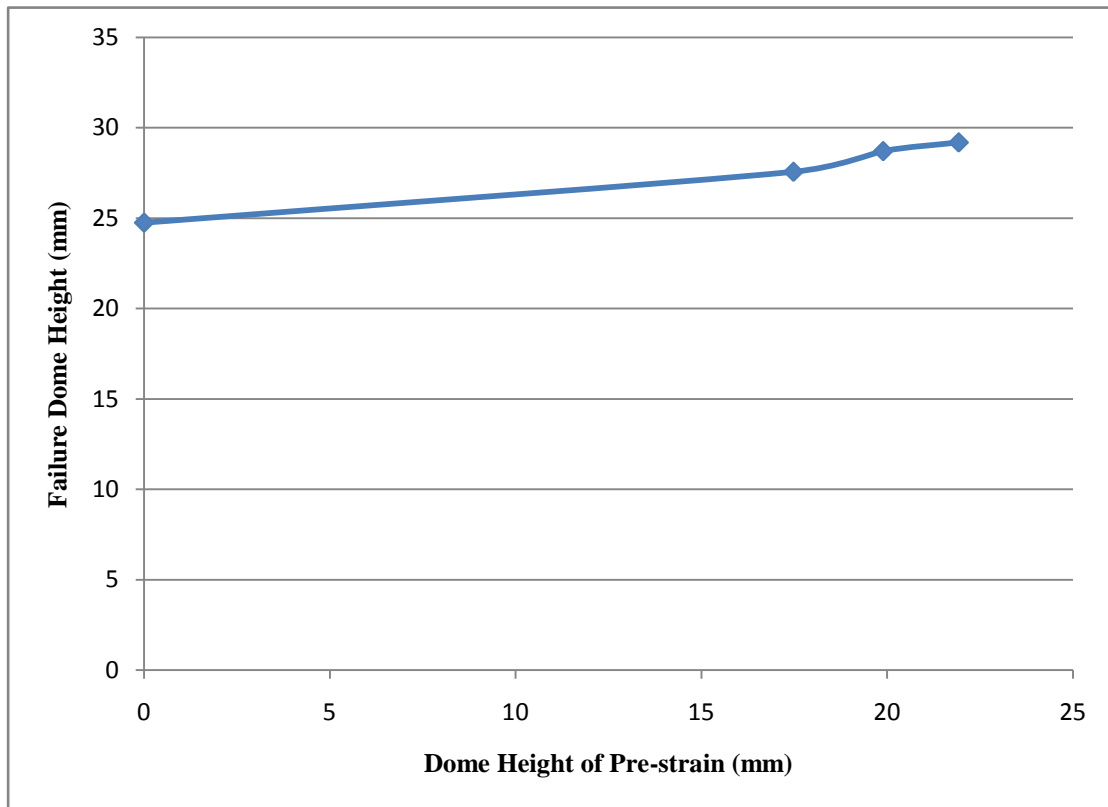


Figure 3.7. Relationship between pre-strain amount and failure dome height.

The effect of the amount of pre-forming on the total formability of material is shown in Figure 3.7. The dome height increased steadily from about 27.5 mm to about 29 mm as the pre-strain was varied from 70% to 90% of the dome height. Therefore, 90% of dome height was selected for all FLD work on pre-stretched materials.

3.2.3 Test Equipment and Test Details

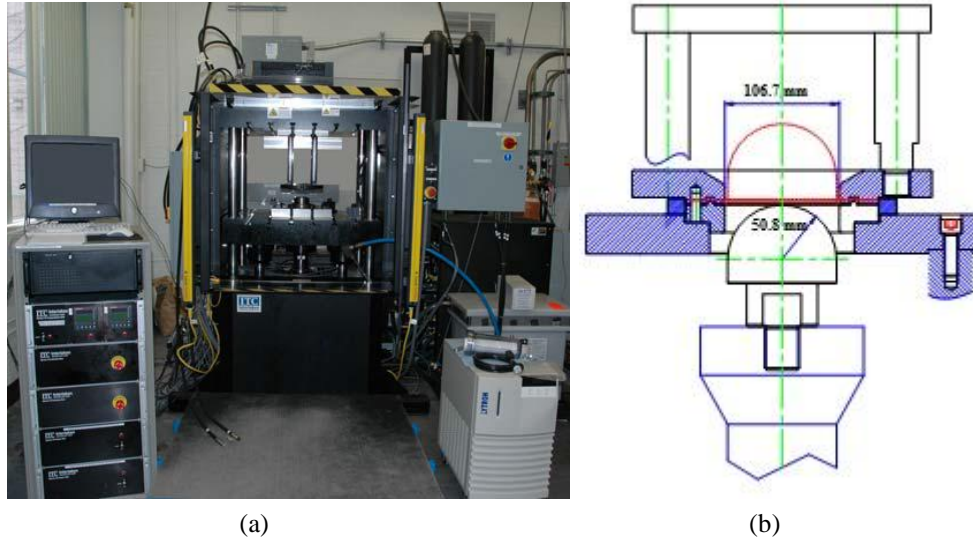


Figure 3.8. Formability test set up; a) Interlaken 150-Ton press, and b) Test configuration.

As mentioned earlier, a new lock bead design was implemented in the LDH tooling to avoid failure of the blank at the lock bead and to ensure no material flow occurred from region of the blank outside of the lock bead into the die. A schematic of the formability test setup is shown in Figure 3.8. The experimental set up consisted of LDH tooling mounted on the test bed of Interlaken 150 Ton double action servo-hydraulic press to carry out the punch stretching experiments. The stretching experiments were performed at a speed of 15 mm/min up to the onset of necking (or fracture, where the neck could not be captured). Punch load versus displacement data was continuously recorded during the test. A 50.8 mm radius hemispherical punch was utilized for the FLD tests. The specimens were clamped by employing a clamping load in the range of 62 kN – 80 kN depending upon specimen geometry. A larger clamping force was applied to the narrower width

specimens.

The various strain paths were achieved by modifying the friction behavior at the punch sheet interface. Three “friction states” used to obtain different strain paths on the bi-axial side were: (i) a high friction state (punch un-lubricated), (ii) an intermediate friction state by using a semisolid lubricant like grease, and (iii) a low friction state by placing a polyurethane pad between the blank and punch. The number of specimens for each strain path varied from 2 to 3. The tests were manually stopped at the onset of necking or at the initiation of fracture. Photographs of various test specimens are shown in Figure 3.9.



(a)



(b)

Figure 3.9. Photographs of various AZ31 Mg specimens, (a) side view, (b) top view.

3.2.4 Strain Measurement

A non-contact (optical) strain mapping system, ARGUS, manufactured by GOM Germany, was utilized to obtain a strain map of the surface of deformed dome specimens. This system consists of a high-resolution CCD camera, a frame grabber card, and the image processing and evaluation software (Figure 3.10). The identification and the calculation of 3D coordinates for each dot used the photogrammetric principle (Figure 3.11). Photogrammetric principle is a science of determining qualitative and quantitative characteristics of objects from the images [41]. The accuracy of the strain calculation is typically in the range of 0.5%.

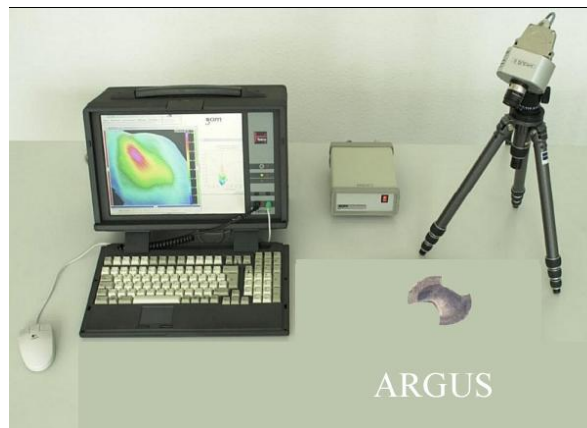


Figure 3.10. ARGUS system set-up.

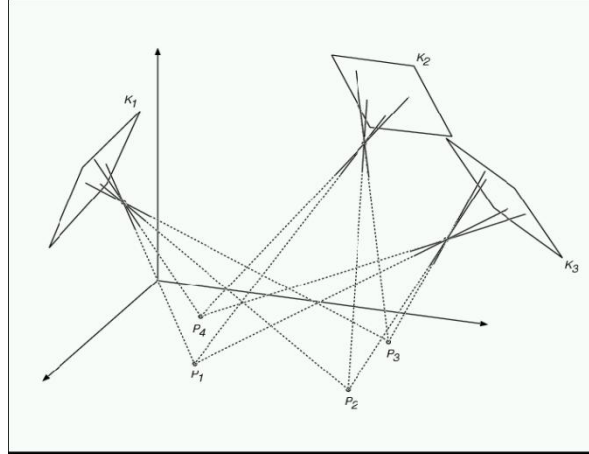


Figure 3.11. Illustration of photogrammetric principles for full-field strain mapping [42].

During the post-test specimen imaging with ARGUS, a scale bar and a series of bar-coded markers were placed around the dome sample as shown in Figure 3.12. The CCD camera captured a series of images of the specimen from the various positions. These images from different perspectives were utilized with dedicated post-processing software in ARGUS.

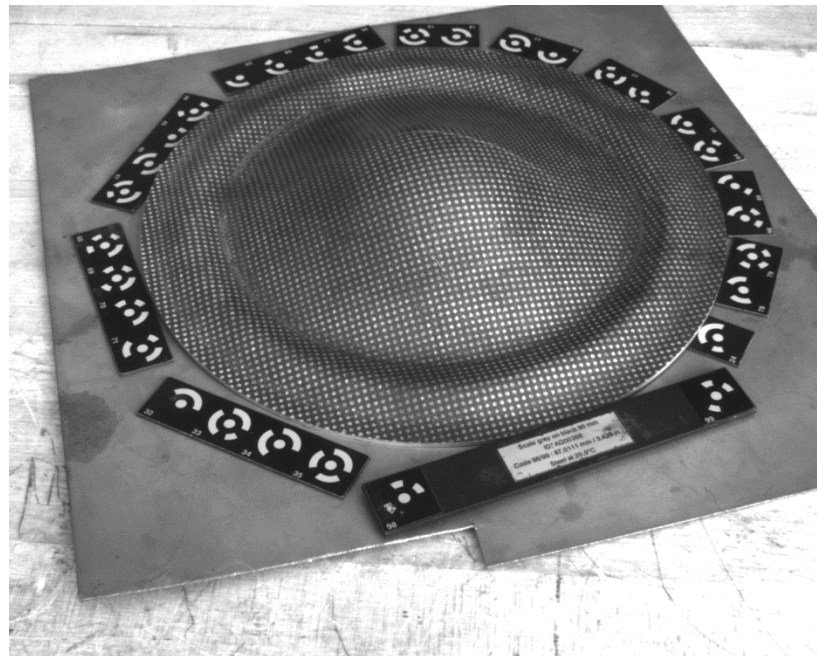


Figure 3.12. Specimen with bar codes recorded by ARGUS.

A schematic diagram of the location of the CCD camera around the sample is shown in Figure 3.13. After recording the images from the different perspectives, the strain calculations were carried out using the post-processing software available with the ARGUS system. The software has a menu driven interface that allows for many options for plotting various 3D strain component in suitable orientations, much like the capability of commercial finite element analysis post-processing packages. A typical major strain map for a full dome sample is shown in Figure 3.14.

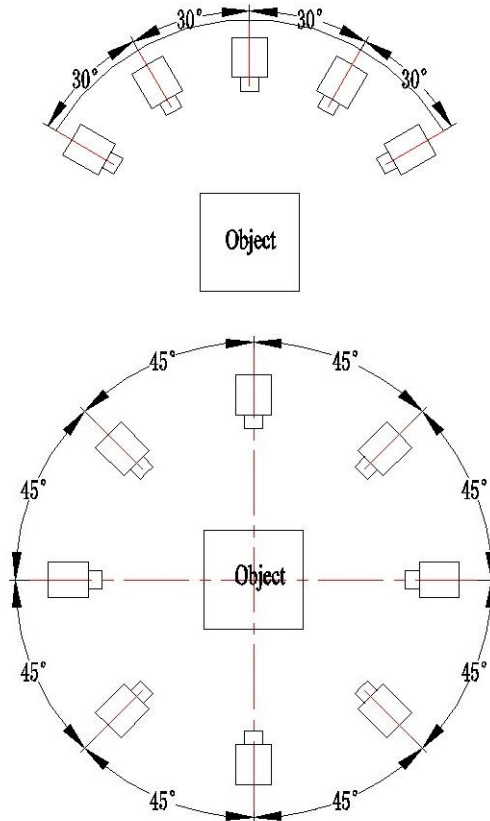


Figure 3.13. Schematic diagram of the camera movement around the dome specimens.

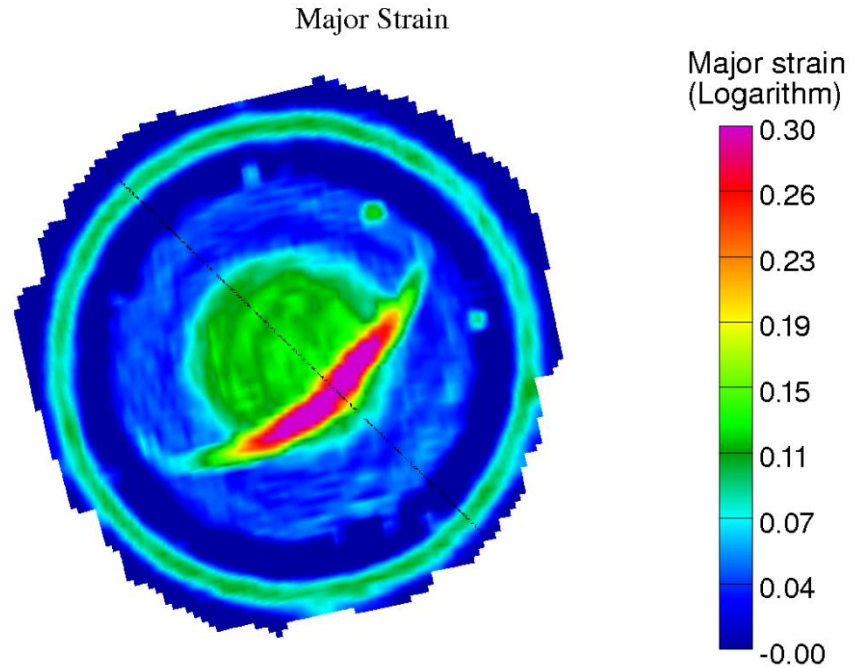


Figure 3.14. Major strain map of a full dome specimen.

3.2.5 Procedures for FLD Determination

To construct FLD, the region around the neck or fracture of each specimen was classified as necked or partially necked, un-necked, and safe (Figure 3.15). The strains were determined from the grid (circular dots) in the vicinity of localized deformation zone or fracture. The major and minor strain data points from all of the test samples of various specimen geometries were then plotted on a single major strain versus minor strain graph. The forming limit curve (FLC) was constructed ("hand drawn") as a lower bound to the necked or fractured grid strain data.

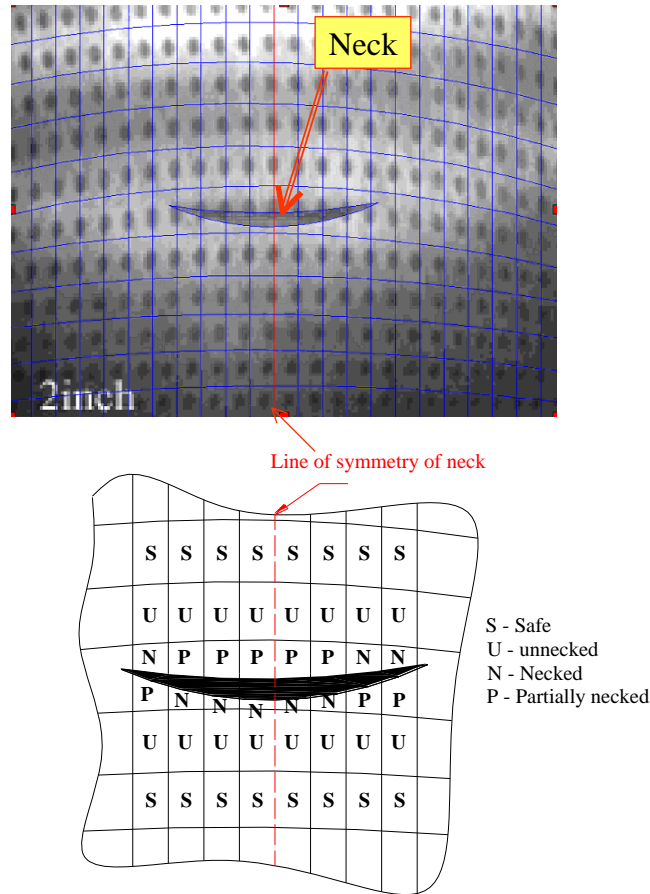


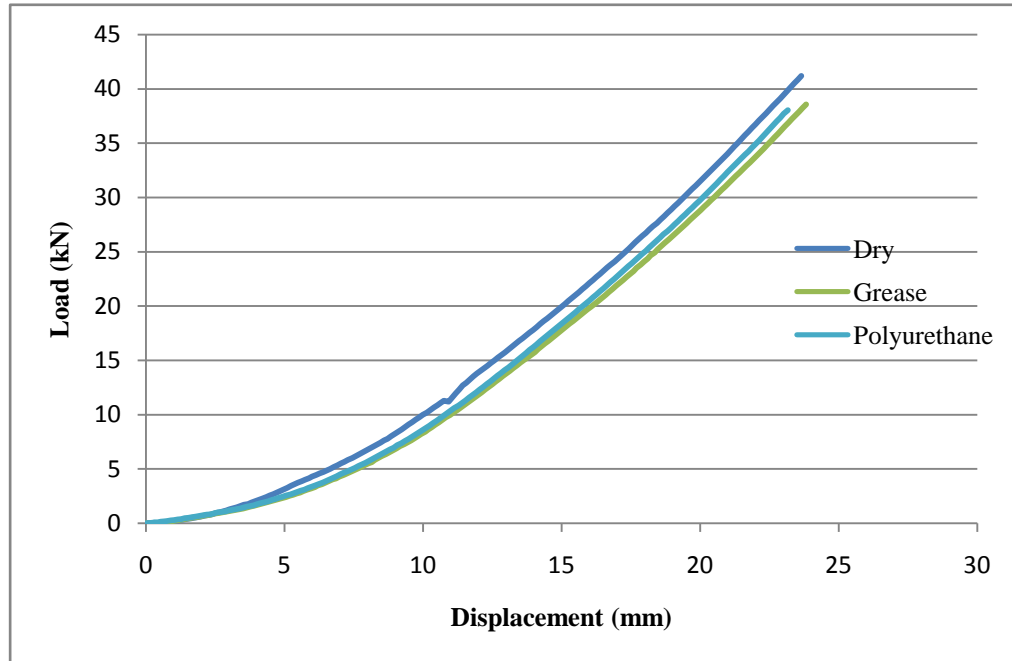
Figure 3.15. A classification scheme for the dots in the neck or fracture region of dome samples [43].

3.3 Results and Discussion

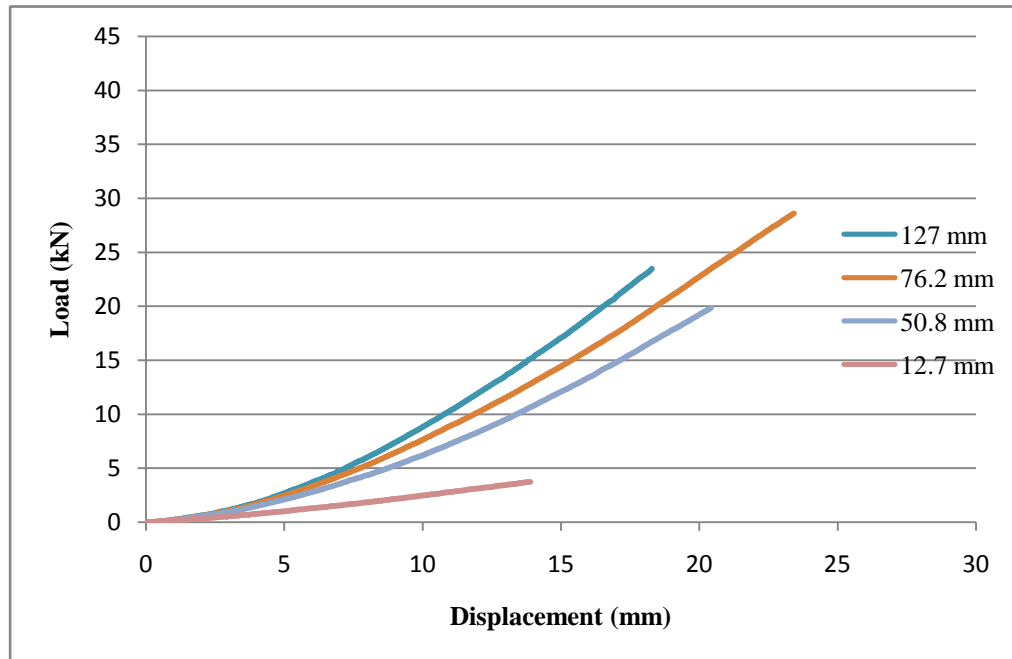
3.3.1 Punch Load Versus Displacement Characteristics

Punch load and corresponding punch displacement results from various fully annealed specimens geometries and lubrication conditions are presented Figure 3.16. This includes some repeat tests as well in Figure 3.16 (a) for full dome specimens. The results for all strain paths (i.e., biaxial tension and tension-compression) are shown in Figure 3.16 (b). As expected, the load and displacement values at dome failure depend on the

lubrication conditions that were used, i.e., dry or no lubricant between sheet and punch, grease and polyurethane pad were used. On average, the use of polyurethane pad did result in failure at the top of the dome and higher punch loads and dome heights. However, variability was observed from test-to-test, perhaps due to some microstructural inhomogeneity in the AZ31 sheet. This was typically more evident on the biaxial side of the forming limit space due to increased damage development from larger hydrostatic stress component. The results for the tension-compression side of Figure 3.16 (b) were consistent with the general trends for most sheet materials, i.e., the punch displacements (or dome heights) was lower in the plane strain state (5 in width specimen) compared to the other narrowest width test specimens, with the exception of 76.2 mm specimen. The dome heights for the different specimens (corresponding to different strain paths) are also shown in the form of a bar chart in Figure 3.17. It was noted that samples with 76.2 mm width have the largest dome height and failure loading force. This phenomenon can not be explained currently. It may be caused by the geometry, as the edge around the narrowest width of sample exhibited anticlastic curvature (Figure 3.18).



(a)



(b)

Figure 3.16. Punch load versus punch displacement traces from LDH tests of fully annealed AZ31 Mg, (a) full dome stretching with different lubrication conditions between the punch and blank, (b) narrower specimens.

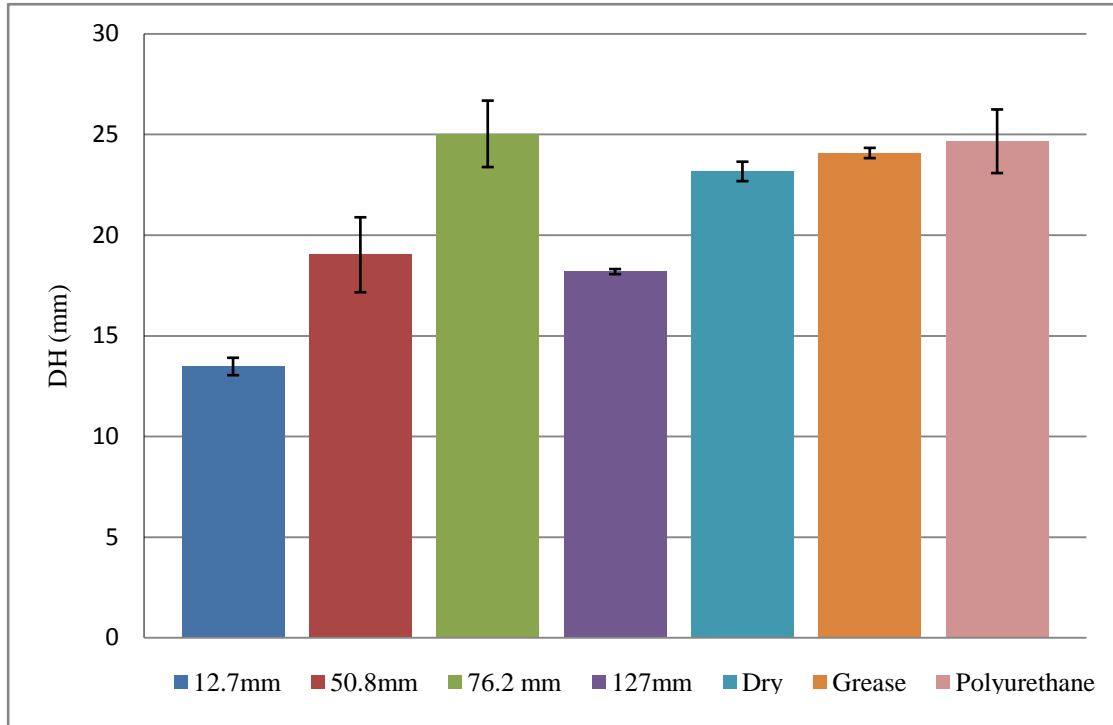


Figure 3.17. Dome heights data from different specimen geometries for fully annealed AZ31 Mg.

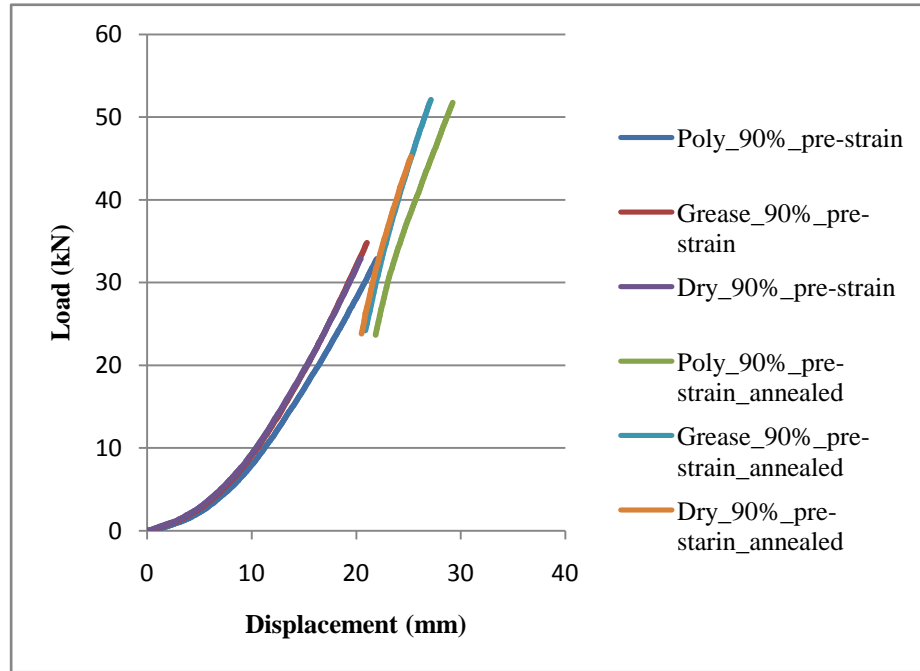


Figure 3.18. A failed 76.2 mm sample. The area in red circle indicates the anticlastic curvature development.

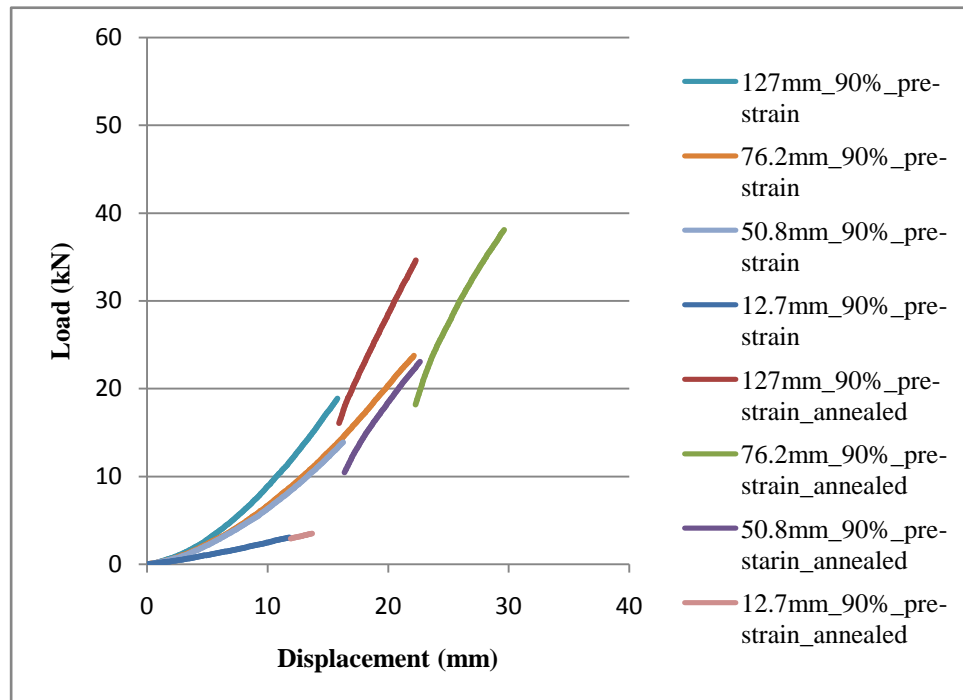
For pre-strain annealed AZ31 Mg, the results in the form of punch load versus displacement traces for the different dimension specimens with different lubrication

conditions are shown in Figure 3.19. The discontinuity corresponds to the pre-strain step when the specimen was removed from the press and annealed. The specimen was placed back into the press after annealing and the stretching continued until the onset of necking or fracture. The drop in the punch load at the intermediate step was indicative of the softening that occurred as a result of intermediate annealing of the specimen. It was also noted that the slope of intermediate step is different from the pre-strain step. If the loading of intermediate step is connected to its corresponding loading path of pre-strain step, it shows an inflection of the slope at the interruption point. The slope of intermediate step is lower than slope of pre-strain step indicative of the softening effect (i.e., increased work hardening effect) of intermediate annealing. A comparison of dome heights for the annealed and pre-strain annealed conditions is shown in Figure 3.20. In the pre-strain procedure, several specimens failed before they could be stretched to 90% of failure dome height. This could be caused by material variability in AZ31. Therefore, the number of specimens for each strain path is limited, so that there is no error bar shown in Figure 3.20. Compared to fully annealed material, the dome heights of pre-strain annealed material was improved by about 20% for most samples (with the exception of 12.7 mm wide sample). This exception may be caused by the geometry issue. As the narrowest width samples necked more significantly than the other geometries, the fracture limit strains measured from for these samples were higher. The limit strains at necking were also higher (as indicated by red square symbols) perhaps due to smaller contact area between the punch and the samples and consequently higher stress and strains in the

vicinity of the neck.



(a)



(b)

Figure 3.19. Punch load versus punch displacement traces from LDH tests of pre-strain annealed AZ31 Mg; (a) full dome stretching with different lubrication conditions between the punch and blank, (b) narrower specimens.

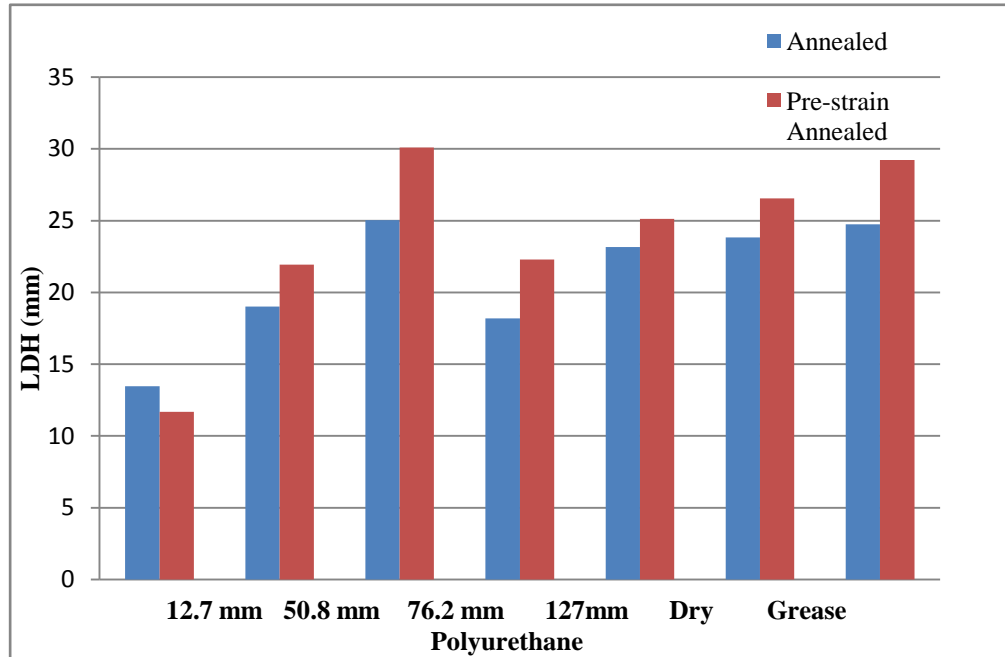


Figure 3.20. Comparison of dome heights data from different specimen geometries for annealed and pre-strain annealed AZ31 Mg.

3.3.2 FLD of Fully Annealed AZ31 Mg Sheet

The room temperature FLD of fully annealed AZ31 Mg sheet is shown in Figure 3.21. It was noted that instead of exhibiting the lowest limit strain at plane strain condition, AZ31 Mg sheet had the lowest formability on the biaxial tension side of FLD, where the major strain and minor strain were 0.07 and 0.013 respectively. At plane strain condition, the limit major strain was about 0.08. The limit strain value at uniaxial was maximum at 0.14, while at equi-biaxial it was 0.114. Similar results have been noted from the numerical predictions of forming limits in Chapter 4. It appears that the shift may be related to material anisotropy of AZ31 (high r value). It was also noted that some safe data and fracture data mixed together. This may be due to the difference in property of material along different orientations (RD and TD).

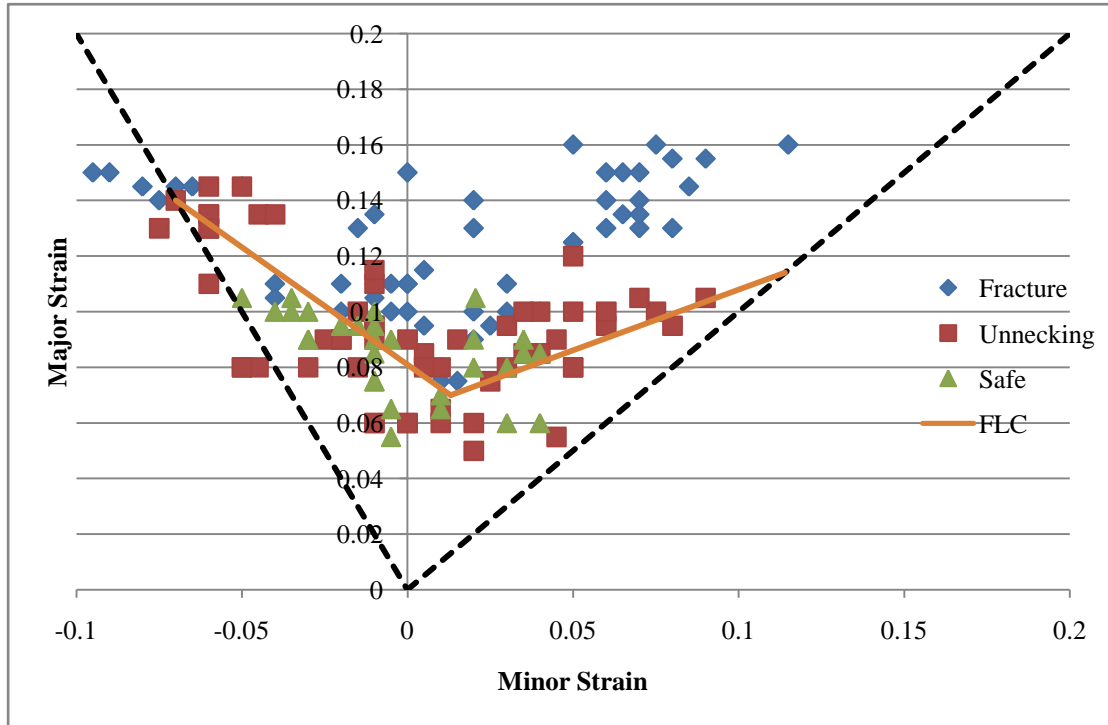


Figure 3.21. FLD and resulting FLC (in orange) for fully annealed AZ31 Mg sheet.

3.3.3 FLD of PASF Processed AZ31 Mg Sheet

Experimentally determined FLD of pre-strain annealed AZ31 Mg sheet is shown in Figure 3.22. Similar to the FLD of fully annealed specimens, the FLD of pre-strain annealed AZ31 Mg exhibited the lowest limit strain at bi-axial loading path, where the major and minor limit strains were 0.1 and 0.02 respectively. The major limit strain in the plane strain condition was slightly higher with a value of 0.116. The major limit strains of 0.18 and 0.195 were attained for equi-biaxial and uniaxial loading paths respectively. A comparison of FLCs from fully annealed and pre-strain annealed specimens is provided in Figure 3.23. As shown, the improvement via the PASF process was slightly more significant for equi-biaxial and uniaxial loading paths compared to the plane strain path.

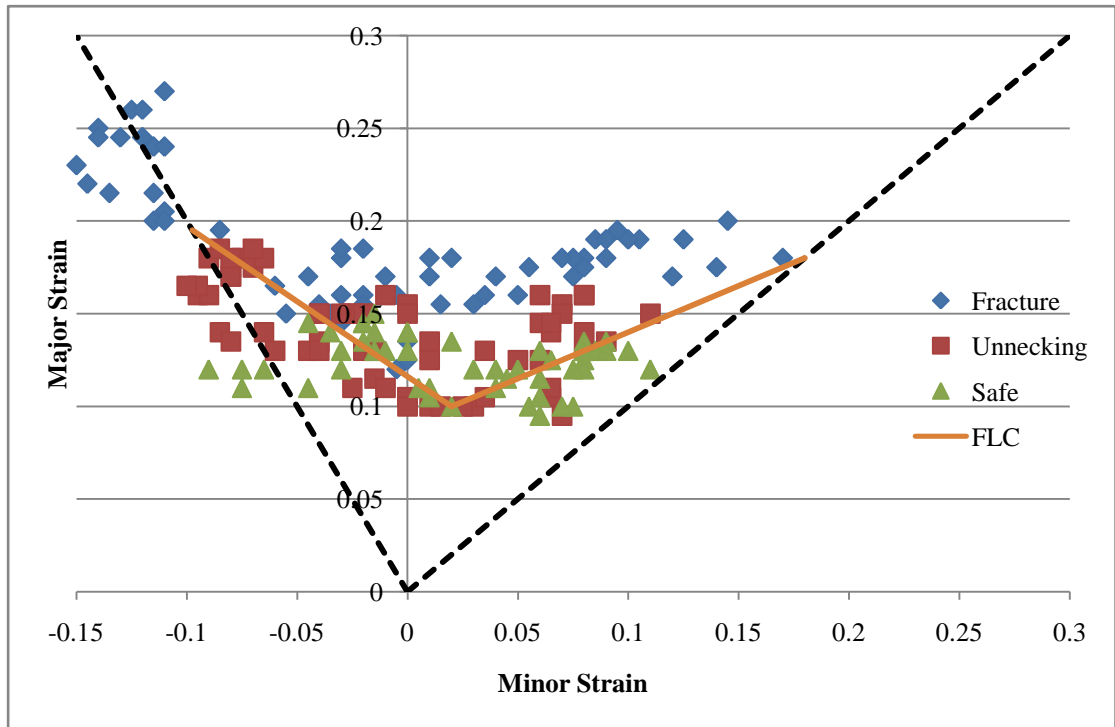


Figure 3.22. FLD and resulting FLC (in orange) for pre-strain annealed AZ31 Mg sheet.

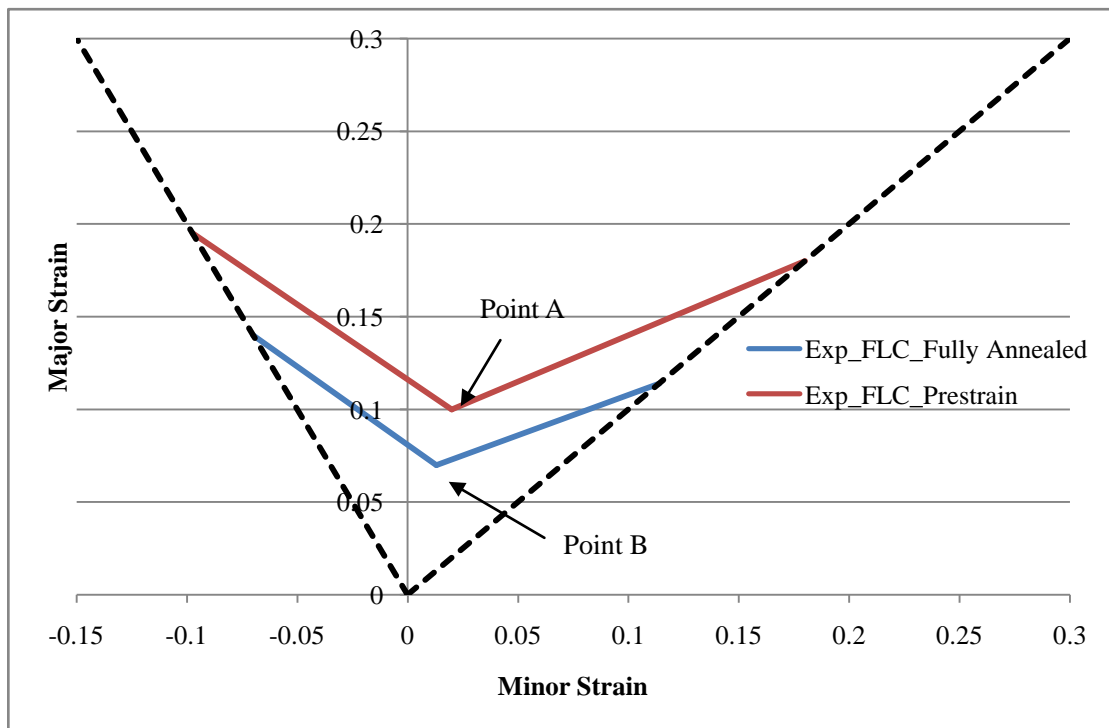


Figure 3.23. A comparison of FLCs between fully annealed and pre-strain annealed specimens.

Table 3.1. Summary of limit strains at various loading paths for both fully annealed and pre-strain annealed AZ31 Mg sheet

Loading Paths	Uniaxial Tension		Plane Strain Tension		Biaxial Tension (Lowest Major Strain)			Equi-biaxial Tension	
	Major Strain	Minor Strain	Major Strain	Minor Strain	Location	Major Strain	Minor Strain	Major Strain	Minor Strain
Fully Annealed	0.14	-0.07	0.08	0	A	0.07	0.013	0.114	0.114
Pre-strain Annealed	0.195	-0.0975	0.116	0	B	0.10	0.02	0.18	0.18

3.3.4 Fracture Characteristics

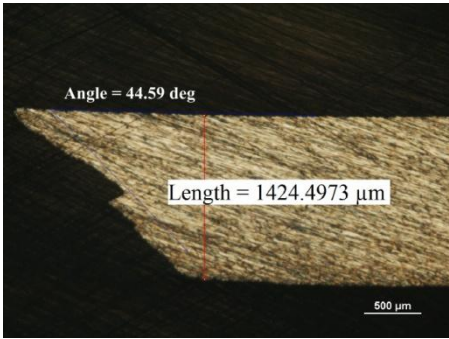
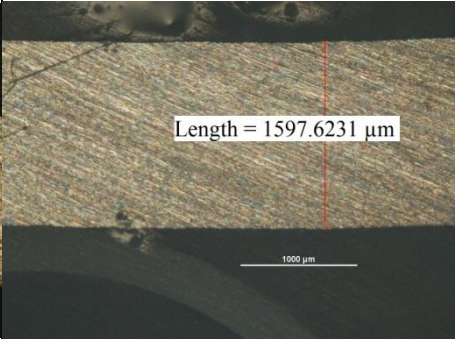
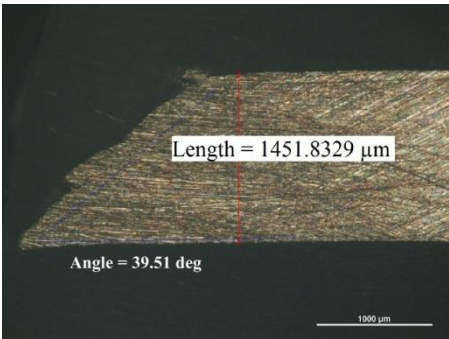
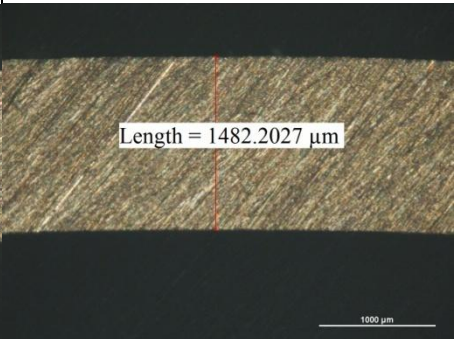
The fracture characteristics varied with different loading paths when fracture edges (through-thickness sections) of deformed dome samples of width 12.7 mm (uniaxial dome) and 127 mm (full dome) were observed optically at a magnification of 5X (see Table 3.2). The thickness and crack angle were also measured by the software and labeled on each image.

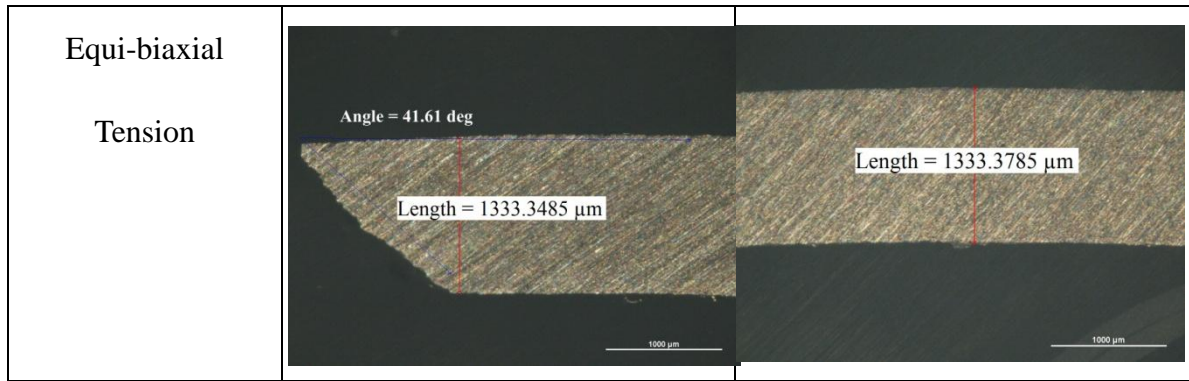
A comparison of thickness in the so-called “safe” region for different loading paths, showed a clear relationship between dome height and thickness. Samples with less dome height were deformed less, therefore resulted in larger thickness values. The sample under uniaxial tension loading path had the least dome height, and therefore yielded a thickness of 1.598 mm, close to the thickness of the initial sheet (1.60 mm). On the other hand, samples tested under plane strain tension and equi-biaxial tension loading paths had larger dome heights, and therefore exhibited lower thickness values of 1.48 mm and 1.33 mm respectively.

A similar comparison of the thicknesses in the vicinity of fracture again showed

strong dependence of the loading path. For uniaxial tension, there was a significant decrease in thickness at fracture due to the necking. However, samples under plane strain tension and equi-biaxial tension had thickness values between fracture and safe areas indicative of lack of necking for these loading paths. The crack angle was a remarkable feature of fracture that was related to the failure characteristic. For the samples under uniaxial tension, where significant necking occurred, a crack angle of 45° was observed. However, for samples subjected to plane strain and equi-biaxial tensions, where almost no necking occurred, a lower crack angle of about 40 degrees was observed.

Table 3.2. High magnification images from fracture and safe areas. (Cont'd on next page)

Loading Paths	Fracture	Safe
Uniaxial Tension		
Plane Strain Tension		



3.4 Summary

The experimental results from forming experiment clearly indicate improvement in the room temperature formability of AZ31 sheet from pre-strain annealing process. The plane strain forming limit was increased from about 0.08 to 0.10 by pre-strain annealing (an improvement of 20%). The limit strain data from the FLDs is consistent with the limiting dome height data. The dome heights at fracture of pre-strain annealed material were improved about 20% compared to the dome heights of fully annealed material.

CHAPTER 4

THEORETICAL DETERMINATION OF FLD OF AZ31 SHEET AT ROOM TEMPERATURE

4.1 Introduction

In the last chapter, experimental FLDs of fully annealed and pre-strain annealed AZ31 Mg sheet were presented. While experimental FLDs are most reliable and preferred for industrial application of die design and stamping failure analysis, theoretically predicted FLDs are often desirable due to experimental cost and time savings, as mentioned earlier in Chapter 1. Punch stretching tests on a large number of samples as presented earlier as well as analysis of experimentally measured strains in the vicinity of the neck are both very time consuming. Also, the cost of experiments is high due to raw material and the need for specialized experimental equipment. Therefore, it is worthwhile to develop a reliable numerical procedure to construct theoretical FLDs of sheet materials. Research related to theoretical prediction of FLDs of automotive steels and aluminum sheet materials have been carried out for more than 5 decades and a reasonable level of accuracy in their prediction has been achieved. However, this is not the case with automotive magnesium sheet materials as these materials are more complex due to their hexagonally close packed (or HCP) crystal structure. In addition, their large deformation and sheet forming behavior is not well understood. Theoretical FLD predictions of AZ31 magnesium sheet at most higher temperatures where the material is more formable have

been reported in the literature. However, very limited and often contradictory theoretical predictions are available at room temperature (see the literature review in Chapter 1). Since the present study is focussed on improving the room temperature formability of AZ31 sheet, a study of the theoretical prediction of FLD of annealed and pre-strain annealed AZ31 sheet at room temperature was considered important.

To construct a theoretical FLD, there are several requirements. Firstly, a suitable material model needs to be chosen from literature (or a new one developed, if such a model is unavailable) for capturing stress and strain states encountered during sheet forming as well as a reliable criterion of localized necking. Secondly, yield criterion and hardening law are required to describe the anisotropic yield and hardening behaviour of AZ31. Marciniak and Kuczynski developed an in-plane forming theory (M-K theory, for short) that encompassed in a utilitarian manner the essential features noted above to calculate the theoretical FLDs of metallic materials [20, 44]. The theory has been improved upon over the years and applied to many metallic materials including numerous steels and aluminum sheet materials. Many of these studies have shown reasonably good agreement for specific sheet materials although work is still continuing to improve theoretical predictions. A few recent papers have reported the use of M-K theory for prediction of FLD of AZ31 at higher temperatures [45, 46]. However, it appears that very few studies have attempted FLD prediction of AZ31 sheet at room temperature due to inherent complexity of characterizing and incorporating the anisotropic yielding and work hardening of AZ31 sheet in the theoretical framework of M-K theory. This chapter

presents an attempt to implement M-K theory towards FLD prediction of annealed and prestrain annealed AZ31 sheet at room temperature. The predictions are compared with the experimental FLD results from the previous chapter.

4.2 Marciniak-Kuczynski (M-K) Model

4.2.1 Basic Mechanics

M-K model is based on the hypothesis of the existence of an imperfection in the sheet metal. The authors in their initial work assumed that sheet metal has geometrical imperfections, such as thickness variation (or groove) within a sheet arising from sheet processing. During the forming process, the imperfection progressively evolves and the plastic deformation of the sheet metal gradually becomes concentrated in it, resulting in necking of the sheet metal. While the initial thickness variation is small, the deformation process in the groove is such that groove region approaches the yield surface first and begins to move along the yield surface to approach a plane strain state. Once the plane strain state in the groove is reached, the strain is highly localized in the groove region and the necking of the sheet specimen follows [47, 48]. This is further described in Figure 4.1 where the specimen consists of two regions: region “a” of uniform initial thickness t_0^a , and region “b” of lower initial thickness t_0^b . The ratio of the initial thicknesses of the two regions is defined as the imperfection factor “f”, where $f = t_0^b / t_0^a$. The model assumes

plane stress state and the specimen is subjected to a constant in-plane loading. Also, the strain components along the groove in the homogeneous and groove regions are assumed to be equal as the deformation proceeds. In other words, a constant ratio of in-plane σ_1 and σ_2 principal stress components (also called stress ratio or σ_2/σ_1) is applied to the specimen. The strain states in the two regions can be analyzed at each incremental stress step, by utilizing the chosen constitutive law and yield function. A certain ratio $\epsilon_1^b/\epsilon_1^a$ of major strains in the homogenous and groove regions is considered as the criterion of necking. When the ratio is too large (infinitely large in theory, but typically greater than 10 in the calculation) the region “b” is considered to be in plane strain state and the groove region “b” of the specimen is considered as “necked”. The corresponding major and minor strains in the homogeneous region “a” are considered as the limit strain of the material for that stress ratio. The M-K analysis is repeated for a range of stress ratios (or equivalently strain ratios or strain paths) covering uniaxial tension to biaxial tension to obtain a complete FLD. A detailed numerical procedure in the form of a flow chart illustrating the implementation of M-K theory is presented later in section 4.4

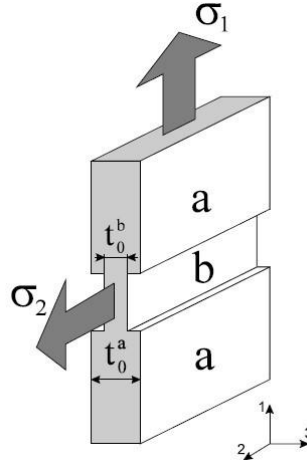


Figure 4.1. Schematic illustration of a sheet with an imperfection.

The initial M-K theory assumed the groove (region “b”) orientation to be perpendicular to the direction of loading. However, it was realized by later researchers that this model could only be truly valid for right side of the FLD (i.e., bi-axial tension side). For the left side of the FLD (negative minor strain region), calculated limit strains showed values consistently higher than the experimental results. Consequently, M-K model was improved upon to calculate left side of the FLD by considering a range of possible orientations of the groove [49]. For a certain loading path (or stress ratio), the limit strain with every orientation of the groove (from 0° to 90°) was calculated and then a major and minor strain pair representing the lowest limit strain value from the M-K calculation was chosen as the limit strain for that specific stress ratio (or strain path), as illustrated by Figure 4.2.

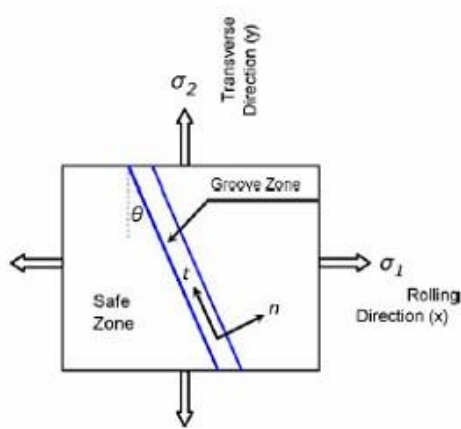


Figure 4.2. Schematic illustration of groove orientation [50].

4.2.2 Yield Model

The yield model or criterion is one of the fundamental components in the M-K based calculation of FLD. The main function of the yield model is to relate stresses (or strains) in different directions to the effective stress (or effective strain) for analysis of stress state (or strain state) in the homogeneous and groove regions. Many yield models have been developed for anisotropic sheet metals over the years [51-55]. However, selection of a particular yield model is dependent on many factors, such as simplicity, accuracy in representing material behavior of a specific alloy, and the effort involved in yield model parameter determination. Considering all of the above factors, Hill's quadratic yield criterion, first published in 1948, has been widely used in the literature. This yield criterion was selected for the present FLD calculation. Very few phenomenological yield criteria have been proposed for automotive magnesium sheet and their validity for sheet forming application is not yet fully known [56]. Also, Hill 1948 criterion is relatively

simple to visualize and implement in the M-K method compared to other proposed yield criteria. Further, Hill 1948 yield criterion includes through-thickness (or normal anisotropy) which can be easily represented with a single parameter plastic strain ratio parameter r that can be readily measured from uniaxial tension tests. As AZ31 sheet has significant anisotropy in the thickness direction [57, 58], Hill 1948 yield criterion was expected to describe its tensile plane stress yield locus ($\sigma_1 > 0, \sigma_2 > 0$), in a reasonable manner. Hill normal anisotropic yield criterion in plane stress state can be expressed as:

$$\bar{\sigma}^2 = \frac{1}{1+r} * [(\sigma_{22} - \sigma_{33})^2 + (\sigma_{11} - \sigma_{33})^2 + r * (\sigma_{11} - \sigma_{22})^2 + 6 * \tau_{12}^2] \quad (4.1)$$

4.2.3 Constitutive Model

The constitutive material model is another essential component in the calculation of FLD. The purpose of constitutive model (also referred to as hardening law) is to mathematically describe the experimentally measured true stress - true strain behavior of the material. Several constitutive material models have been developed for non-linear work hardening sheet materials based on their experimental deformation characteristics. Among them, the Holloman equation (also known as power law) is perhaps the oldest, most popular, and simplest. However, the prediction of power law is not always close to the observed material behavior for many metallic materials and especially for aluminum sheet materials. Another well-known material model is by Voce [59] that has been shown to represent experimental stress-strain curves of many sheet materials rather well. It was therefore assessed and subsequently selected as the constitutive model for AZ31 sheet for

FLD calculations. Voce hardening law in the form of effective stress and effective strain is expressed as,

$$\bar{\sigma} = a_1 + a_2 * \exp(a_3 * \bar{\epsilon}) \quad (4.2)$$

where the a_1 , a_2 and a_3 are non-linear regression fit parameters. It is to be noted that AZ31 sheet exhibits quite different stress-strain characteristics in uniaxial tension and uniaxial compression. Since forming limit determination involves mostly tensile state of deformation, uniaxial tension test data (and not uniaxial compression data) was utilized for the assessment of a suitable constitutive law for M-K analysis.

4.3 Determination of M-K Model Input Parameters

4.3.1 Determination of Yield Model Parameter

To determine the r -value parameter in the normal anisotropy version of Hill 1948 yield criterion, uniaxial tension tests were utilized in conjunction with an optical strain measurement system ARAMIS [42]. Tensile test specimens were machined according to ASTM standard E8 (compact size) with 25.4 mm gauge length, 0.635 mm gauge width, and 0.635 mm fillet radius as depicted in Figure 4.3. All of the samples were machined to be pulled along the rolling direction, and the test speed was set as 1 mm/minute in the computerized test control software.

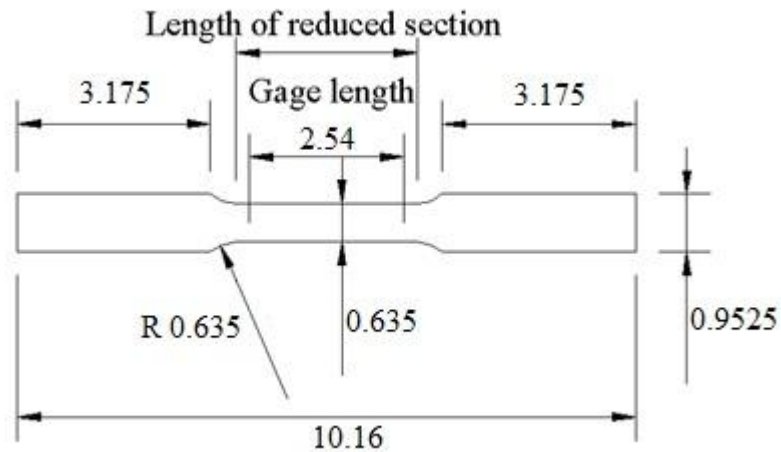


Figure 4.3. Specimen dimension for tensile tests (in mm).

The ARAMIS system utilizes continuously recorded camera images of the gauge region of a deforming uniaxial tensile specimen for so-called full-field strain measurement. The gauge region is pre-applied with a random (or speckle) pattern for strain analysis of the deformed images, and the analysis within the ARAMIS system is based on the well-known digital image correlation (or DIC) method. As shown in Figure 4.4, a high speed camera was positioned in the gauge region of the sample and continuous images with a speed of 1 frame/second were acquired during testing. ARAMIS divides the entire image region into smaller square or rectangular subspaces called facets. A facet size of 15×15 pixels was utilized within ARAMIS software to obtain strain map from the gauge region of the specimen to an accuracy of 0.01%.



Figure 4.4. Tensile test set-up with ARAMIS.

In addition to uniaxial tensile true stress-strain curve from the uniaxial test data, the strains along the axial (ϵ_l) and width (ϵ_w) directions of the test specimen from ARAMIS, along with the assumption of plastic incompressibility ($\epsilon_l + \epsilon_w + \epsilon_t = 0$), were used to obtain the anisotropic coefficient r-value based on the following expression:

$$r = \frac{\epsilon_w}{\epsilon_t} \quad (4.3)$$

where ϵ_w and ϵ_t are true width and thickness strains in the homogeneous gauge region of the test sample. It is to be noted that both the width and thickness strains are negative in uniaxial tension, and therefore, r is a positive value. Also, instantaneous r value during the tensile tests could be calculated and plotted as a function of the axial (or major) strain to appreciate changes in the anisotropic behaviour of the sheet material with increasing deformation. For formable sheet materials, including automotive steels and aluminum

sheets, the r-value increases at first but reaches saturation after some plastic strain. In fact, ASTM-E517 standard calls for using an axial plastic strain of 0.10 to obtain an r-value when the r-value versus axial strain curve for the above sheet material has “flattened”. Unfortunately, the r-value versus axial strain curves for AZ31 sheet did not exhibit shape characteristics of the other well-known materials. The shape of the curve did indeed show “rise” at first like the other materials but then increased with a steady slope and finally rose steeply beyond a r-value of 2 (Figure 4.5).

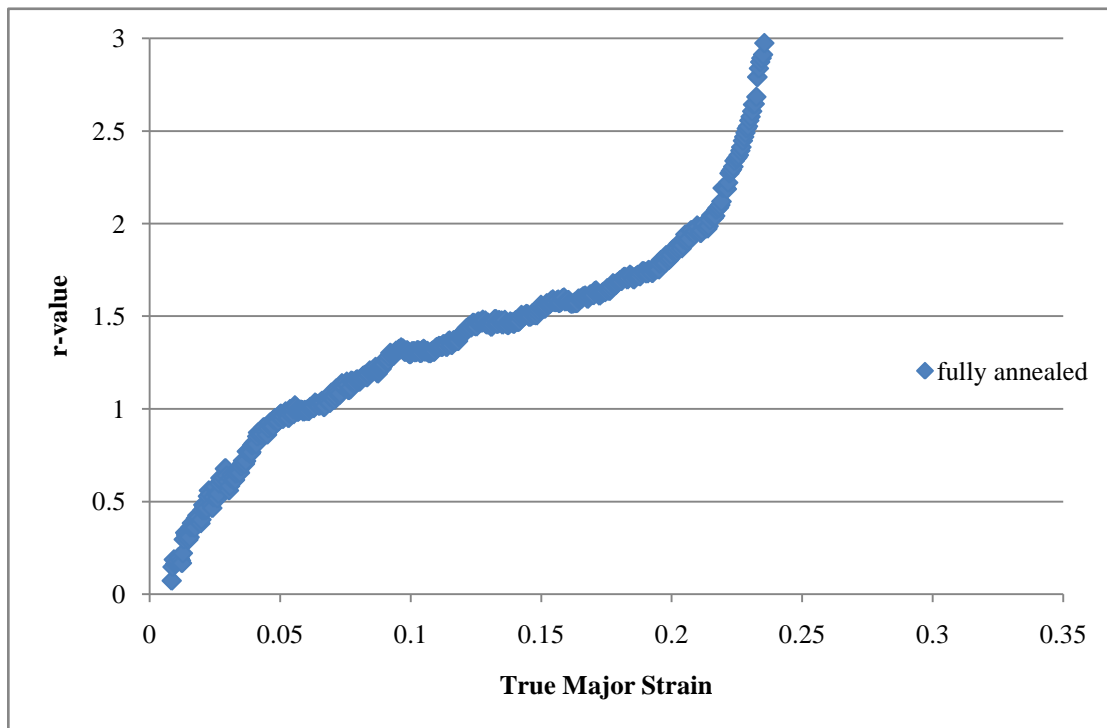


Figure 4.5. Anisotropic coefficient r-value versus true major strain from tensile test of a fully annealed sample.

For the calculation of pre-strain annealed FLD, sheet samples were tested under both fully annealed condition as well as for several different pre-strain amounts (2%, 10%, 14%, 16% 20% and 22%). These tests resulted in r-value versus axial strain curves shown

in Figure 4.6.

These curves show quite similar shapes and follow classic sigmoidal function, which can be expressed as follows:

$$r = \left[\left(\frac{a_2 * b_2 * c_2}{a_2 - \varepsilon_1} - b_2 * c_2 \right) \right]^{\left(\frac{1}{c_2} \right)} \quad (4.4)$$

where a_2 , b_2 , c_2 are fit parameters.

For each pre-strain amount, the r -value versus major strain data was fitted with the above sigmoidal function to determine the fit constants. The quality of the fit for a typical data set corresponding to a pre-strain of 14% in Figure 4.6 is presented in Figure 4.7. An R-square (goodness-of-fit parameter) value of about 0.97 was obtained indicating a good quality of fit.

It has been reported that measured r -value for AZ31 Mg will increase dramatically when the localized necking occurs but in the pre-necking region, r -value stays almost constant [60]. As shown in Figure 4.6, from the present work on AZ31 sheet, the r -value starts to increase dramatically after reaching a value of 2 and in the axial strain range of about 0.20 – 0.3 for the various pre-strains. Therefore, two aspects of the experimental r -value data were applied to the Hill 1948 yield criterion. First, the r -value was not treated as a constant but allowed to vary as a function of strain in the M-K analysis. Second, as soon as the r -value increased to 2, it was assumed to stay constant at 2.

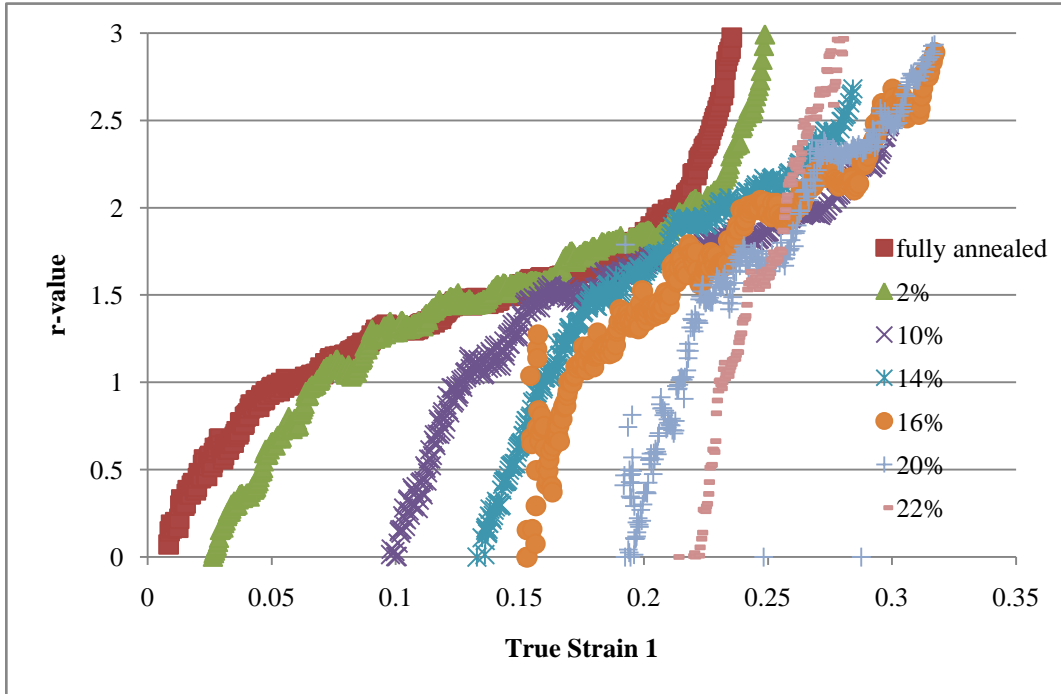


Figure 4.6. Anisotropic coefficient r-value versus true major strain from tensile test samples with different amount of pre-strain.

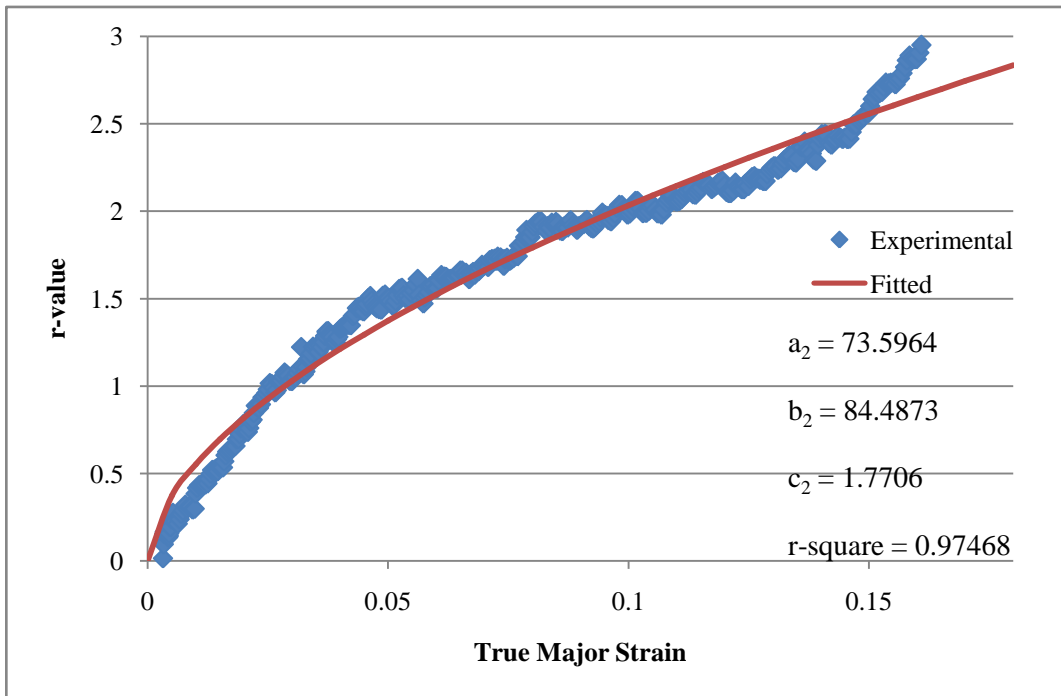


Figure 4.7. The r-value versus true major strain for 14% pre-strain material. Blue diamond symbols are for experimental results and the red line is for a fit using sigmoidal function.

4.3.2 Determination of Constitutive Model Parameters

To determine the constitutive model parameters, tensile tests with different amounts of pre-strain were utilized. The pre-strain amount was varied from 2% to 22%. All the samples were intermediate-annealed at 250 °C for 30 minutes. The recorded stress-versus-strain curves are plotted in Figure 4.8. All of the curves subsequent to pre-strain interruption, labeled with “_2”, were shifted to start from the origin and then fitted with the Voce hardening law to determine the constants. In Figure 4.9, Voce-law fitted stress-strain curve of fully annealed material is plotted along with the experimental results. The elastic component of deformation was neglected and the fitting was carried out in plastic deformation range only. The fit was deemed ‘good’ except for the final stage of curve, where some drop in the stress value could be observed in the experimental data. The R-square value for this fitting was about 0.9991.

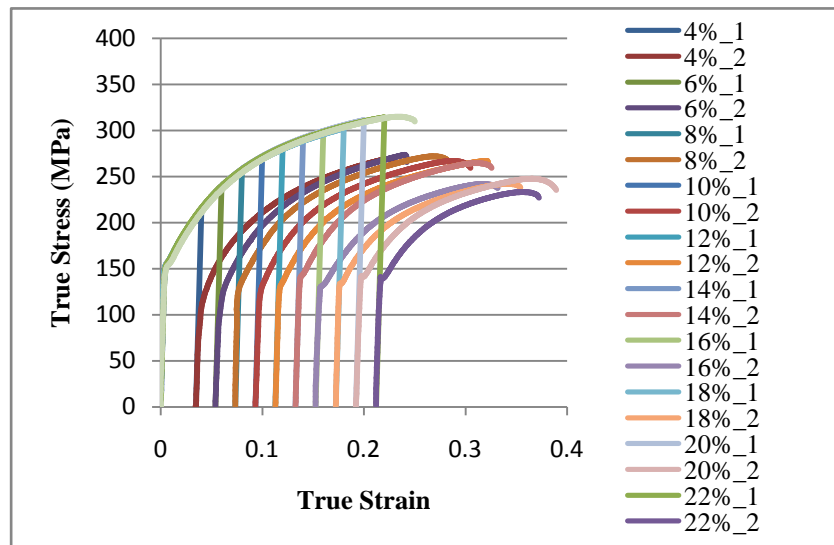


Figure 4.8. True stress versus true strain from tensile test samples with different amount of pre-strain.

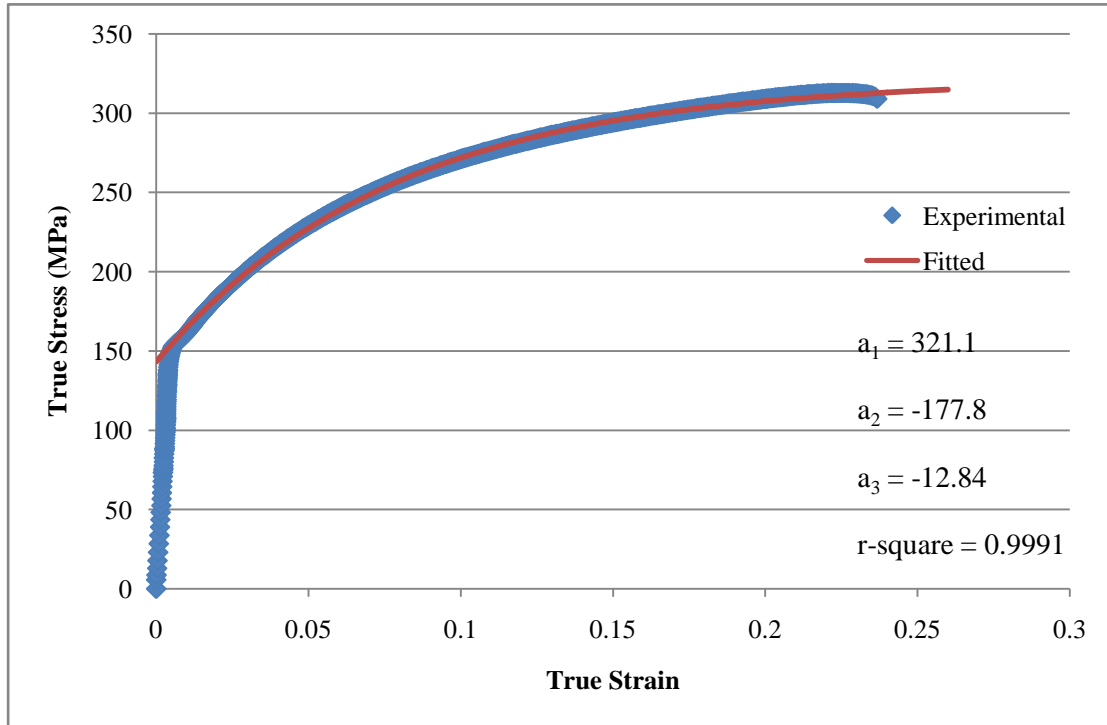


Figure 4.9. True stress-strain tensile response for fully annealed material. Dots are for experimental results and the line is for correlations using voce model.

4.3.3 Determination of Surface Roughness

The imperfection factor (or f-value) is known in the literature to significantly influence the calculated FLD in M-K analysis. To reduce the subjectivity in the selection of f-value no suitable reference in the literature could be obtained for AZ31 sheet. Considering the basic definition of f-value, which is the ratio of initial thicknesses inside the groove and outside the groove, it was decided to utilize the initial peak-to-valley surface roughness (R_{PV}) of the sheet to estimate the f-value [61]. This value could be readily obtained from 3D surface roughness measurement on the undeformed AZ31 sheet surface using a commercial surface roughness measurement system (ZYGO New-View 5000). A sample area of 1 mm^2 was measured and the resolution of the image was 0.01

nm. As shown in Figure 4.10, the R_{PV} value for the initial sheet surface varied in the range 17513 - 37748 nm. This value indicates the maximum difference in thickness of neighbouring regions of the sheet.

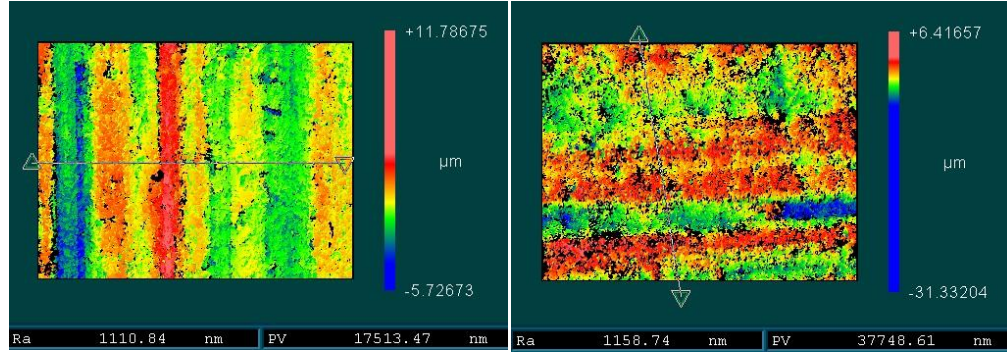


Figure 4.10. Measurements of surface roughness

By assuming the sheet has same surface roughness on both sides, the range of f-value was calculated using the following expression:

$$f = \frac{t_0 - R_{PV}}{t_0} \quad (4.5)$$

The above expression yielded f-values in range 0.952 – 0.978 based on the range of experimentally measured R_{PV} values.

4.4 M-K Theory Numerical Implementation

Since a FLD consists of many pairs of limit strain values each corresponding to a chosen loading path, the procedure of calculating FLD can also be broken into many single step calculations of the limit strain along each loading path (each loading path has a constant stress ratio, α_a , as noted earlier) [62]. In Figure 4.11, it shows a calculation flowchart for determining the room temperature FLD of AZ31 based on model

approximations and data presented in the earlier sub-sections. By imposing a strain increment in direction 1 outside the groove, $\Delta\varepsilon_{1a}$, corresponding strain increments in other directions, both inside and outside the groove, could be calculated according to the so-called flow rule. A flow rule relates plastic strain increment to the stress increment in the classical theory of plasticity. These increments were then added to the previous total strain values inside and outside the groove to obtain the current strain values as shown in the flow chart. It is to be noted that the elastic contributions being very small are neglected in this analysis, so the material has been assumed to be ‘work hardening plastic’. As the calculation proceeds along a specific strain path, the difference in strain increment inside and outside the groove continued to increase. When the ratio of strain increment inside and outside the groove along the 1 direction reached a value of 10, the sample geometry in the model was considered as “necked”, and the current strain state outside was recorded as the limit strain for this loading path. By repeating the above procedure with different stress ratios, limit strains along different loading paths was obtained. By constructing a locus of the pairs of limit strain, FLD of fully annealed material could be obtained.

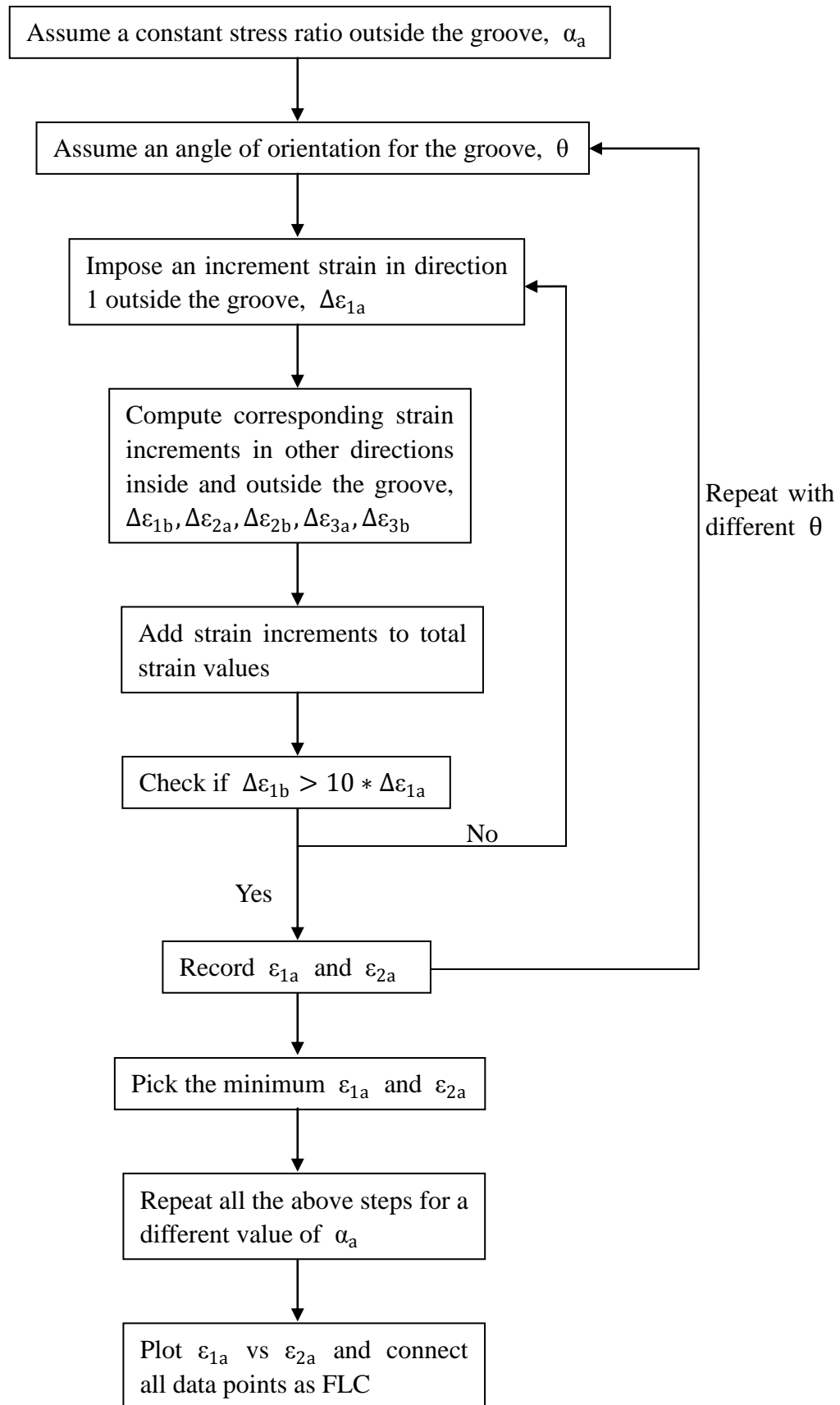


Figure 4.11. Flow chart for the calculations of theoretical FLDs for fully annealed material.

To calculate FLD of pre-strain annealed (or PASF) material, the procedure needed to be revised (Figure 4.12). Firstly, the value of pre-strain amount for each loading path needed to be determined. In the experimental FLD determination process, all specimens were pre-strained to 90% of their failure dome height. As the punch was moved at a constant speed during the test, 90% dome height was considered equivalent to 90% of deformation time. Therefore, the true major strain versus time for tensile test of fully annealed material was plotted as shown in Figure 4.13. By dividing strain at 90% time by strain at failure, the ratio of pre-strain to fracture strain was determined. This calculation was repeated for several set of tensile test data, to yield a consistent value of 0.87. Therefore, 87% of limit strain values was assumed to correspond to a pre-strain with 90% of limit dome height. The effective strain of each loading path was then calculated. In the next calculation step, the limit strain was recalculated to reflect the deformation process after intermediate annealing. In this calculation, material constants were used according to its effective strain amount. For example, if the effective strain equaled a value of 0.1, the material constants from 10% pre-strain data were utilized. Finally, by adding limit strain values of pre-strain and after intermediate-annealing, limit strain value of pre-strain annealed material were obtained. All of above calculations were carried out in Matlab software (version R2010a).

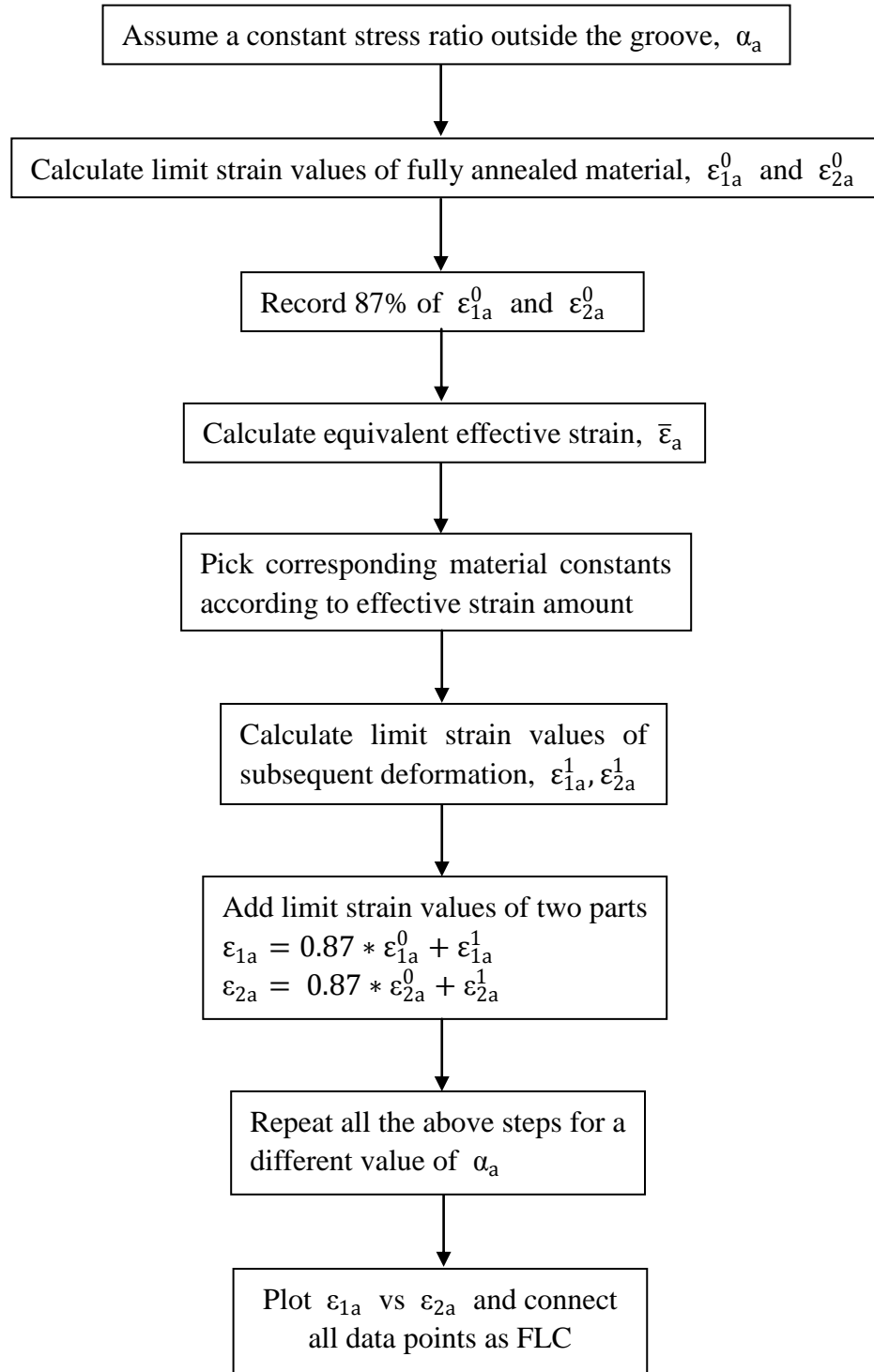


Figure 4.12. Flow chart for the calculations of theoretical FLDs for pre-strain annealed material.

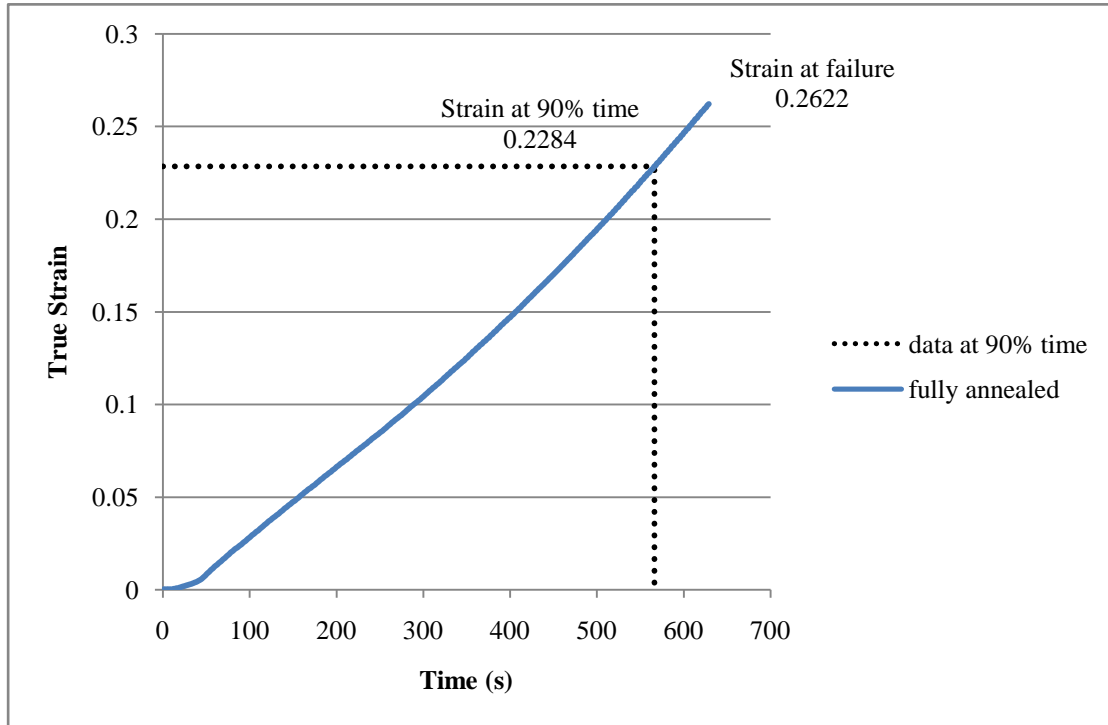


Figure 4.13. True strain versus time for fully annealed material. Data point indicated by dot lines is taken at 90% time of tensile test.

4.5 Results and Discussion

4.5.1 Effect of Various Parameters on FLD Characteristics

4.5.1.1 Effect of Inhomogeneity factor (or f-value)

In general, the FLD calculated based on M-K method had two major characteristics that varied with the choice of input parameters. These were; the value of the plane strain limit (or FLD_0) and shape of the curve (i.e., the average slope of the curves on both sides of the plane strain limit). In this study, the influence of f-value and orientation of groove were primarily explored. FLDs were calculated with the same material constants for yield

and hardening but with different f -values. As shown in Figure 4.14, as the f -value was varied, the biaxial tension side of FLD became more sensitive to f -value than the tension-compression side. The f -value influenced both the shape and level of biaxial tension side of FLD, but influenced only the level of tension-compression side (and not the shape). For example, when f -value was increased from 0.96 to 0.99, the limit strain of uniaxial loading path increased only by 0.04, but the limit strain of equi-biaxial tension loading path increased by more than 0.3.

The influence of f -value on FLD has been also analyzed in previously published work on steels and aluminum alloys. In Figure 4.15(a), Marciniak [20] has summarized relationship between equi-biaxial limit strain and f -value. These results show that the equi-biaxial limit strain value increases with an increase in f -value, and this relationship is more sensitive when f -value is closer to 1. Figure 4.15(b) presents the results of Lian et al. [49] on the influence of f -value on compression-tension side of FLD. The results show that when f -value is increased, the limit strain is also increased. Furthermore, f -value only influences the level of FLD but not the general shape of FLD. These effects of f -value are consistent with what has been studied in our FLD calculations.

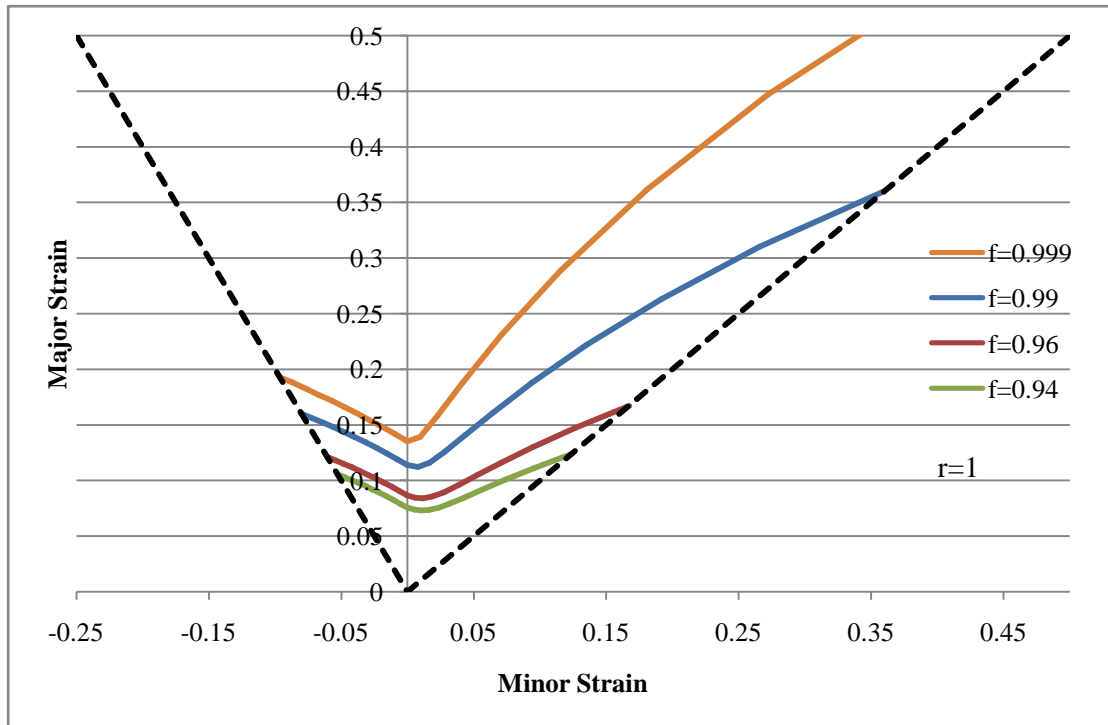


Figure 4.14. Calculated FLD for same material constants but alternative f-value.

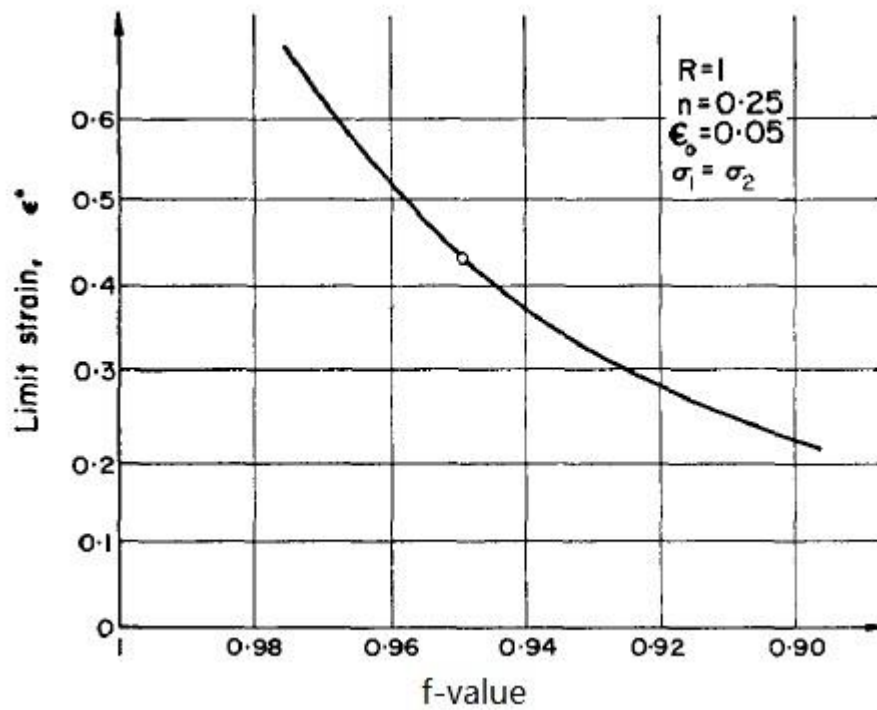
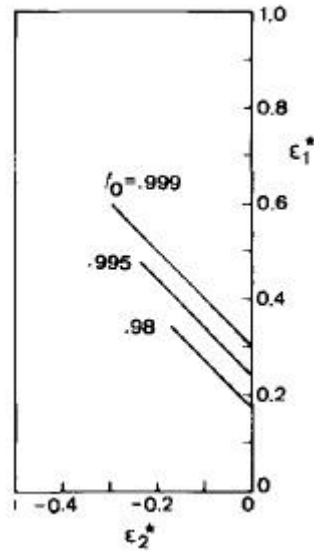


Figure 4.15. (a) Cont'd on next page)



(b)

Figure 4.15. Influence of f-value on FLD in (a) equi-biaxial tension loading path from Marciniak [20], and (b) tension-compression side from Lian et al. [49].

4.5.1.2 Effect of Groove Orientation

The effect of groove orientation was analyzed by computing FLDs with the same material constants and f-value but by varying the orientations of groove for a given stress ratio. These results, as shown in Figure 4.16, indicate that without considering the groove orientation ($\theta = 0$), there is no effect on biaxial tension side of FLD. However, for tension-compression side of FLD, calculated limit strain value is much higher than the experimentally measured value if $\theta = 0$ [63]. Therefore, it is important to include groove orientation into FLD calculations. However, as this will increase computing time significantly, it is important to determine a reasonable range for groove orientation. Figure 4.17 shows a plot of major strain versus groove orientation for several loading paths. As shown, the stress ratio greater than 0.5 (biaxial tension side of FLD), the

minimum limit strain value is always given by $\theta = 0$. When the stress ratio is between 0 and 0.5 (tension-compression side of FLD), the minimum limit strain value is given by $45^\circ > \theta > 0^\circ$. Therefore, the variation of groove orientation should be limited to the range $0^\circ - 50^\circ$ in FLD calculation for better efficiency.

These effects of groove orientation were also noticed in a fracture mechanics study [64]. Figure 4.18 indicate the nature of plastic slip processes and the planes of maximum stress that occur under mode I (normal stress) loading for plane stress and plane strain conditions. For plane stress condition, it shows that the maximum stress occur along at 45° to the plate surface, which means the material should fail along this direction, and the minimum limit strain should also occur along this direction. As uniaxial loading ($\theta = 0$) is a typical plane stress condition, this could explain why 45° of groove orientation gives the minimum limit strain value for FLD calculation along uniaxial condition. For plane strain condition, it shows that the maximum stress occur on planes perpendicular to the plate surface, where the groove orientation is 0° along this direction. This explains why the minimum limit strain in plane strain condition is given by $\theta = 0$.

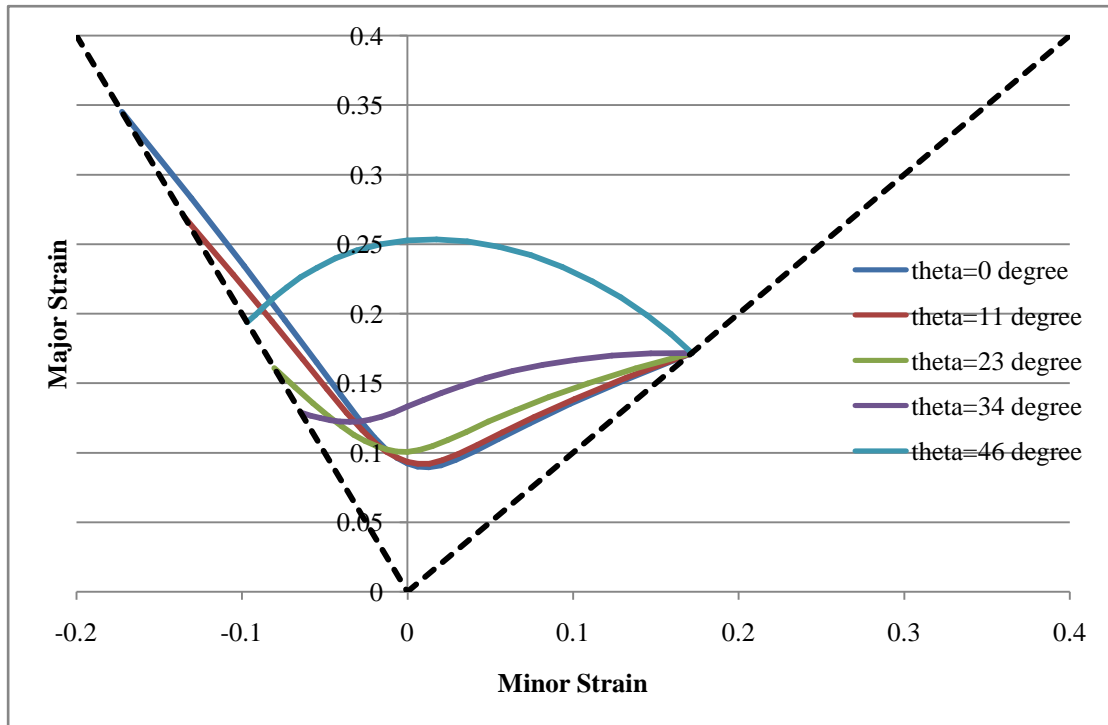


Figure 4.16. Calculated FLD for same material constants but alternative orientation of groove (θ).

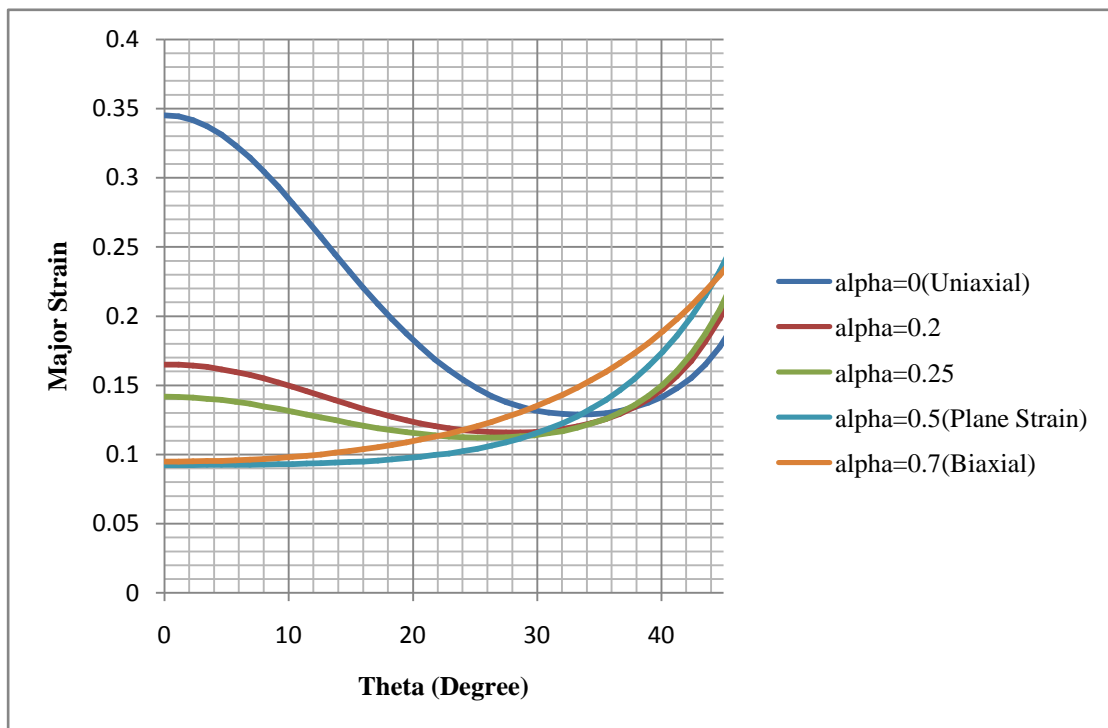


Figure 4.17. Variation of major strain with orientation of groove (θ) at different stress ratio (α).

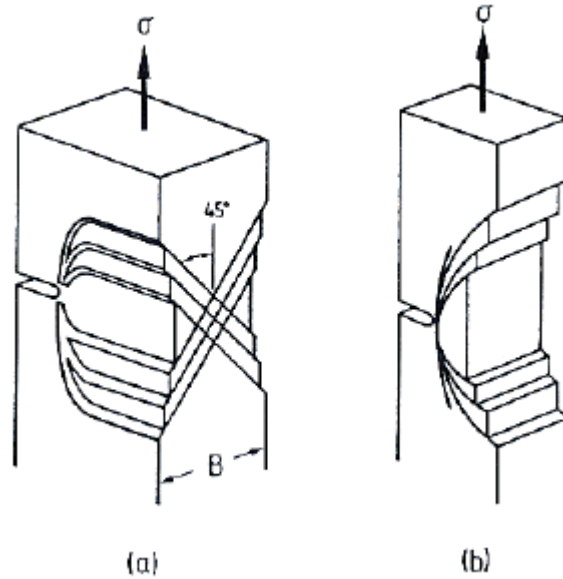


Figure 4.18. Slip-plane around a mode-I crack for (a) plane stress and (b) plane strain. It is to be noted that the sheet thickness is not to scale [64].

4.5.1.3 Effect of r-value

The influence of r-value (or strain ratio) is shown in Figure 4.19. The increasing in r-value about unity results in a reduction in limit strain along all loading paths. Similar to the effect of f-value, r-value influence both level and shape of FLD on the biaxial tension side, but only the level of FLD on the tension-compression side. However, the effect of r-value is opposite to that of the f-value, which means the limit strains are decreased when r-value is increased. This effect of r-value was also discovered by Marciniak [20] as shown in Figure 4.20, where the limit strain along equi-biaxial loading path decreases when r-value is increased. Furthermore, another effect of increasing r-value was to shift the location of lowest limit strain towards the biaxial-tension side of FLD. This phenomenon was also observed in the experimental FLDs presented earlier in Chapter 3,

where the lowest limit strain was located on biaxial-tension side of FLD.

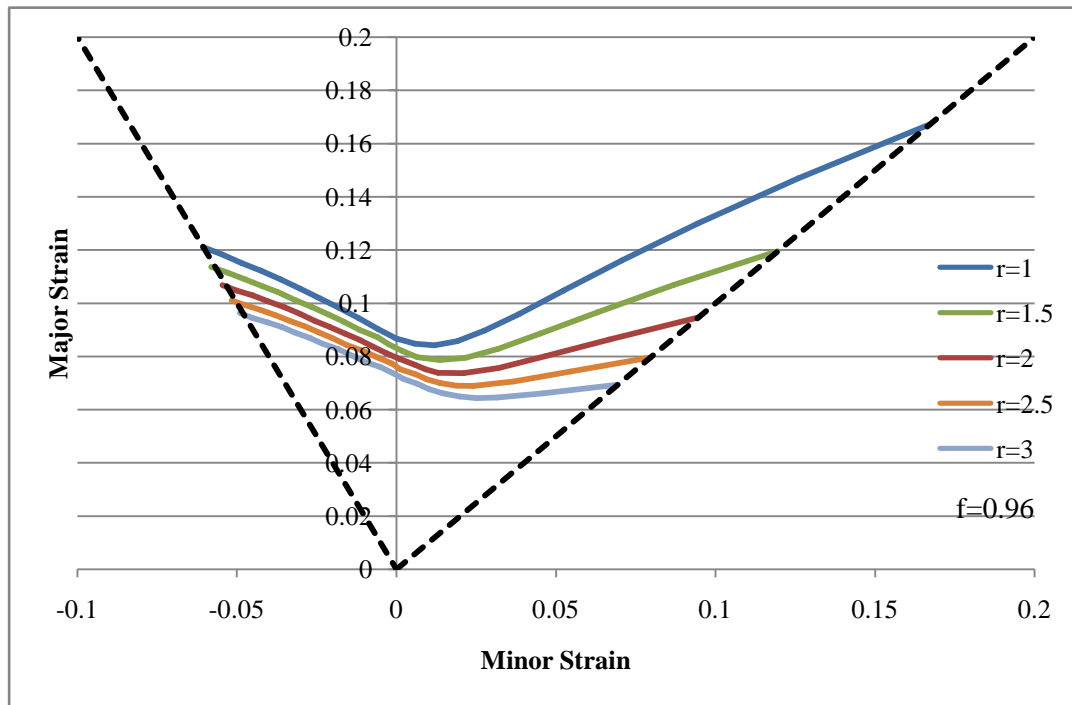


Figure 4.19. Calculated FLD for same material constants but alternative r-value.

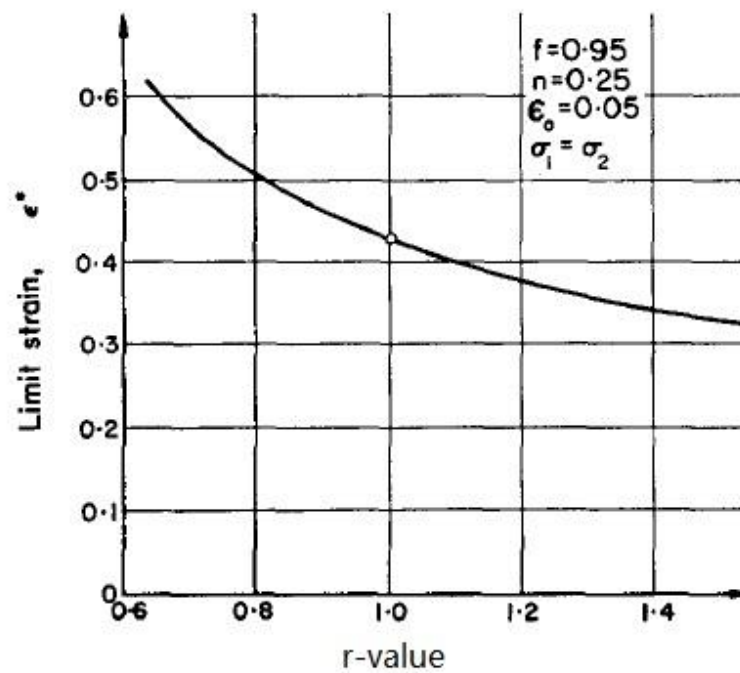


Figure 4.20. Influence of r-value on FLD in equi-biaxial tension loading path from Marciniak [20].

4.5.2 FLD Prediction of Fully-annealed AZ31 Mg

Figure 4.21 presents the calculated FLD of fully annealed AZ31 Mg sheet along with the earlier experimental FLD. In general, slope of the curve on right side of the plane strain limit of calculated FLD matches well with the experimental FLD. However, slope of the curve on uniaxial loading side of plane strain limit is slightly lower than the experimental FLD for most of the tension-compression region and then crosses over to a higher value near pure uniaxial tensile strain path. Furthermore, both calculated and experimental FLDs have the lowest limit strain slightly to the right of the plane strain limit, in the biaxial loading region. For the level of FLD, calculated limit strain values is quite close to experimental results. However, the calculated limit strain value in plane strain condition is somewhat larger than experimental results, and the calculated limit strain value at uniaxial loading path is smaller than experimental result. The largest difference occurs in biaxial loading region closer to the plane strain region, which is about 0.01.

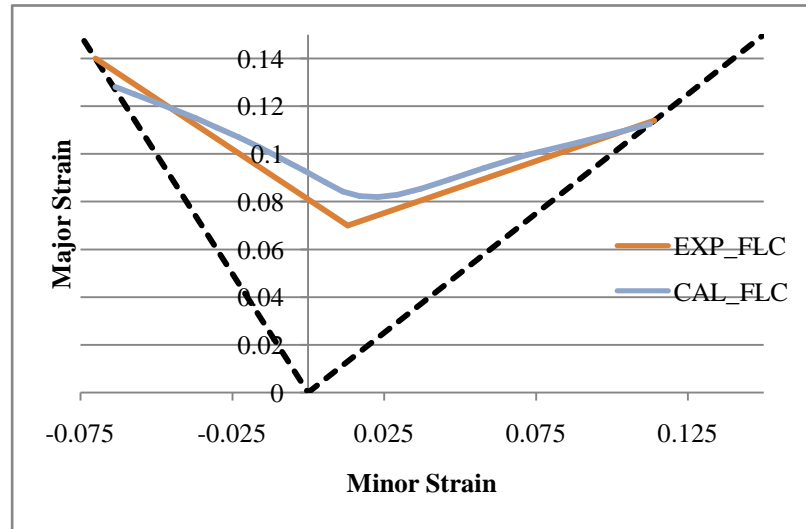


Figure 4.21. A comparison between calculated and experimental FLDs of fully annealed AZ31 Mg sheet.

4.5.3 FLD Prediction of PFSA AZ31 Mg

The calculated FLD for pre-strain annealed material is plotted along with the experimental determined FLD in Figure 4.22. The slope of calculated FLD is almost the same as the experimental FLD in uniaxial loading path. However, the slope of calculated FLD in biaxial loading path is slightly smaller than experimental FLD. For the level of FLD, calculated limit strain values is matched to experimental results at the equi-biaxial loading path. However, the level of calculated FLD is about 0.005 and 0.02 higher than experimental FLD in uniaxial loading path and plane strain condition. The largest difference occurs in biaxial loading region beside the plane strain region, which is about 0.03.

Comparing the two calculated FLDs, the one for fully annealed material has much better agreement compared to the pre-strain annealed material. This may be because the

calculation for pre-strain annealed material is more complex. Some material properties have been changed during the pre-strain process. For example, the initial f -value used in the calculation of second-stage forming is difficult to determine accurately. Even when the f -value is adjusted according to the result in calculation of first-stage forming, it may still have errors, which could affect the accuracy of final result.

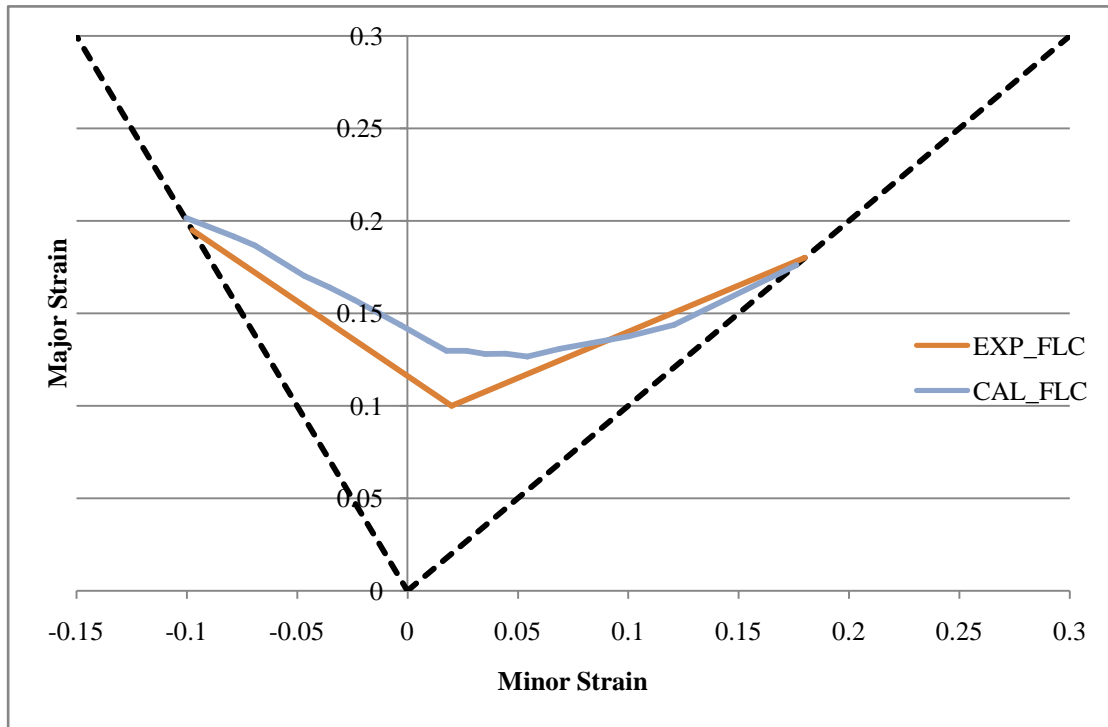


Figure 4.22. A comparison between calculated and experimental FLDs of PASF processed AZ31 Mg sheet.

4.6 Conclusion

Several modifications have been made to the well established M-K method to account for specific characteristics of AZ31 magnesium sheet such as evolution of r -value based on r -value versus axial strain data, and f -value based on peak-to-valley surface

roughness of initial AZ31 sheet surface. The method has also been adapted to simulate pre-strain annealed AZ31 sheet where 90% pre-strain rule has been implemented. The calculated FLDs for fully annealed and pre-strain annealed material show a reasonably good fit to the experimental determined FLDs. For fully annealed AZ31 Mg, the prediction is more accurate in most loading paths. For pre-strain annealed AZ31 Mg, the prediction matches shape of experimental results, while it has a large mismatch in limit strains along biaxial loading path.

During the FLD calculation with M-K theory, some features have also been verified for AZ31 sheet. Firstly, the influence of f -value and r -value on the FLD has been analyzed and compared with those presented in the literatures. Secondly, the effect of groove orientation on FLD calculation has been explored in detail and explained with fracture theory. Thirdly, a modified method of using M-K theory to calculate FLD of pre-strained material has been developed. However, this method may require further improvement for a better prediction of the tension-compression side of FLD.

CHAPTER 5

THEORETICAL PREDICTION OF FLD OF AZ31 MAGNESIUM SHEET AT HIGHER TEMPERATURES

5.1 Introduction

In a recent experimental study at McMaster, currently under review for publication in a journal, the experimental FLD of AZ31 Mg at 300°C has been determined by gas bulging tests using a novel specimen and die design [65]. Since all experimental details were provided in the above reference, they will not be repeated here. In this chapter, the M-K method developed in the previous chapter for FLD prediction of AZ31 at room temperature was utilized to calculate FLD at 300°C . As the basic M-K theory used for 300°C FLD calculation remained the same as room temperature FLD calculation, this procedure also will not be repeated here. However, revised yield and constitutive material model were implemented for FLD calculation at 300°C as described below.

5.2 Revised Calculation for High Temperature FLD Determination

At 300°C , the mechanical properties of AZ31 Mg sheet are changed significantly from room temperature. Therefore, it is essential to re-consider the models and parameters for FLD calculations. Firstly, the AZ31 Mg sheet exhibited near isotropic stress-strain response at 300°C [66, 67] as shown in Figure 5.1. The quality of fitting by

Mises and Hill's quadratic yield criteria were very close. Therefore, Mises yield model was suitable to describe the yield locus in place of Hill quadratic yield criterion.

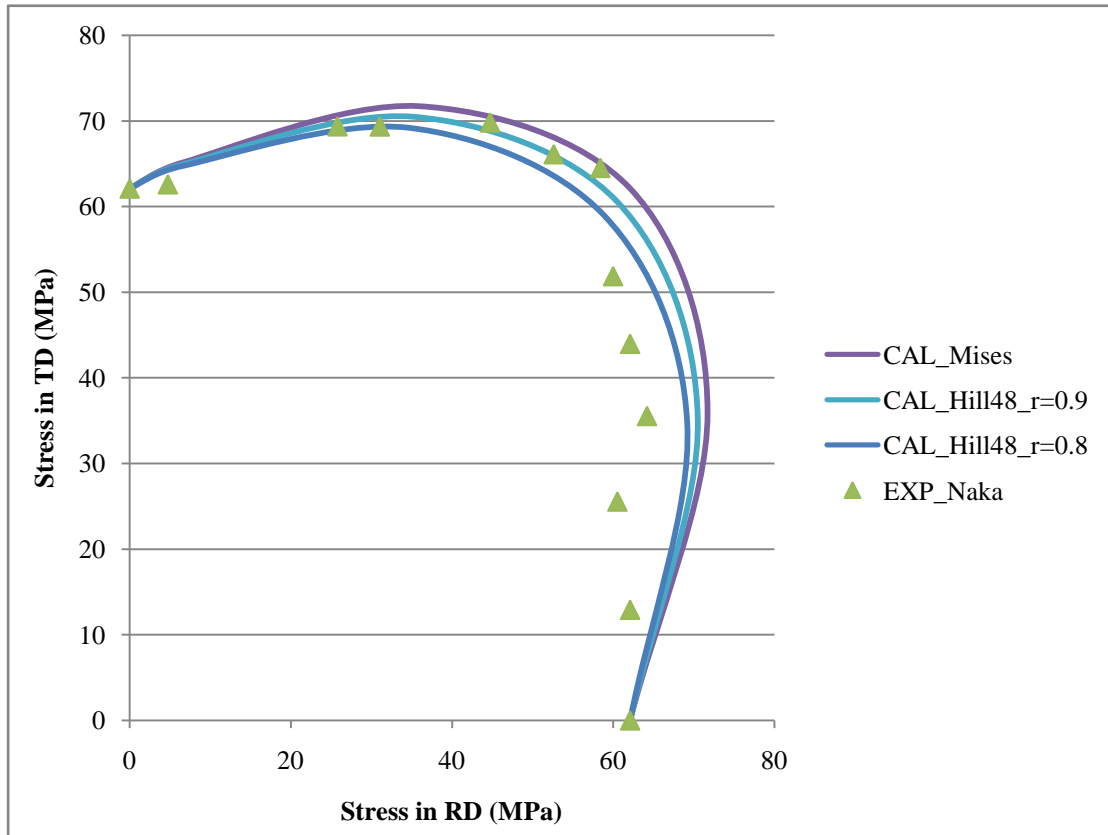


Figure 5.1. Yield loci of AZ31 at 300 °C . Triangle symbols are for experimental results and lines are for calculated results.

Secondly, AZ31 Mg exhibited softening at 300 °C . This softening phenomenon led to a decrease in yield stress as well as in reduction of slope of stress-strain curve immediately after the yield point. Consequently, the Voce hardening law could no long capture the stress-strain behaviour of the AZ31 sheet. Therefore, many other constitutive equations that include strain rate and temperature were attempted to fitting the stress-strain curve [68-78]. Among these equations, the one from Shida's et al. [69, 70],

was assessed for its applicability to deformation of AZ31 sheet at higher temperature.

Figure 5.2 shows a fit of the Shida's equation (eqn. 5.1 below) to the experimental true stress-true strain data of AZ31 at 300 °C . The Shida's equation is expressed as follows:

$$\sigma = a_3 * \exp\left(\frac{b_3}{T} - c_3\right) * \left[d_3 * \left(\frac{\varepsilon}{e_3}\right)^n - g_3 * \varepsilon\right] * \left(\frac{\dot{\varepsilon}}{h_3}\right)^m \quad (5.1)$$

where a_3 , b_3 , c_3 , d_3 , e_3 , g_3 , h_3 , m and n are non-linear fit parameters. As shown, a rather good fit to the experimental data was achieved. Therefore, the Shida's was selected as the constitutive model for 300 °C FLD calculation.

As the experimental FLD at 300 °C was determined by gas bulging tests that lacked adequate control of the gas pressure during the bulging process, the corresponding strain rates could not be exactly determined. In order to make a reasonable estimation, the following approach was followed. Since the constitutive model were fitted according to tensile test data, which were deformed along uniaxial loading path, the limit strain along uniaxial loading path was picked, which was 0.80. By dividing the strain over the total time of deformation (10 minutes), the average strain rate could be determined, which provided a value of 0.001333/second. Since the tensile test with strain rate of 0.001/second had the closest strain rate value to the gas bulging test, this stress-strain data set was used for 300 °C FLD calculation and to compare with the experimental determined FLD.

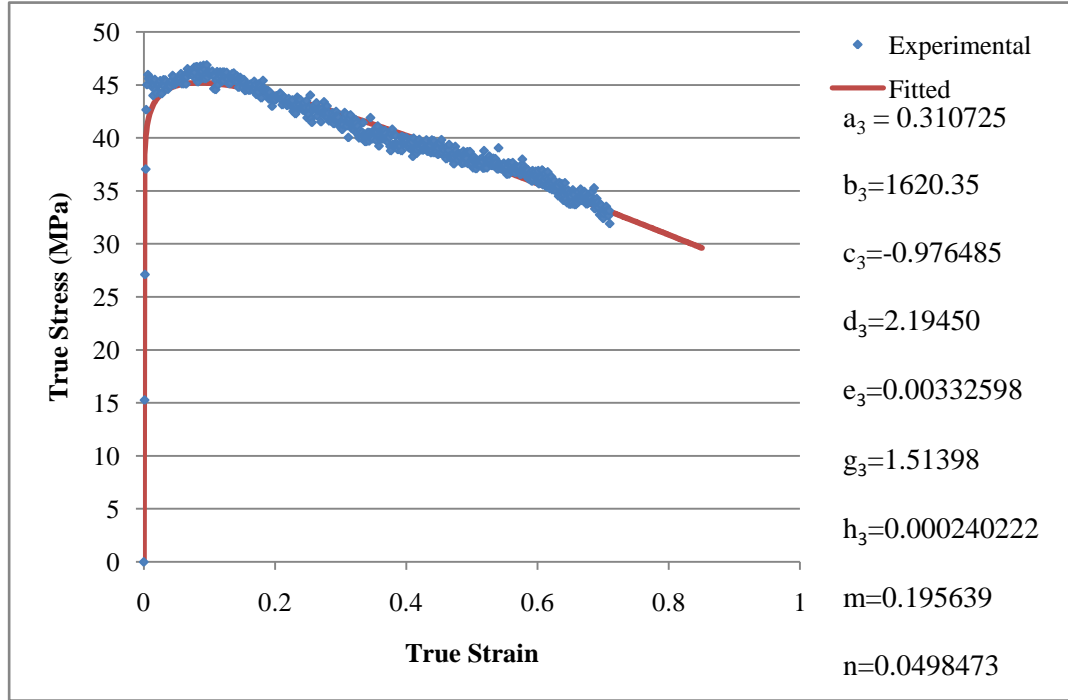


Figure 5.2. True stress-strain tensile response for fully annealed material. Dots are for experimental results and the line is for fit Shida's equation.

Thirdly, at 300°C , AZ31 Mg becomes much softer and more ductile, which makes the material more formable (larger failure strain). As the deformation process becomes longer, the influence of the initial imperfection (f-value) on the calculated FLD also becomes less. Therefore, in the high temperature FLD calculation, a higher f value of 0.999 was utilized. With above modifications, the procedure of FLD calculation for fully-annealed AZ31 Mg (of Section 4.4) was applied to calculate FLD of AZ31 at 300°C .

5.3 Results and Discussion

Figure 5.3 compares the calculated and experimental determined FLDs of AZ31 at

300 °C . In general, the calculated FLD matches well with the experimental FLD, with a small drop in the calculated FLD on the biaxial tension side. For the level of FLD, calculated limit strain values is quite close to experimental results in the compression-tension side and in the plane strain condition. Furthermore, both experimental and calculated FLD have the lowest limit strain in bi-axial tension side. However, lowest limit strain of calculated FLD is closer to the plane strain state than in the experiments. This may be because the material was assumed to be isotropic in calculation while it was likely somewhat anisotropic.

For the level of FLD, the calculated result is fairly close to the experimental result. The largest mismatch of about 0.05 occurred on bi-axial tension side.

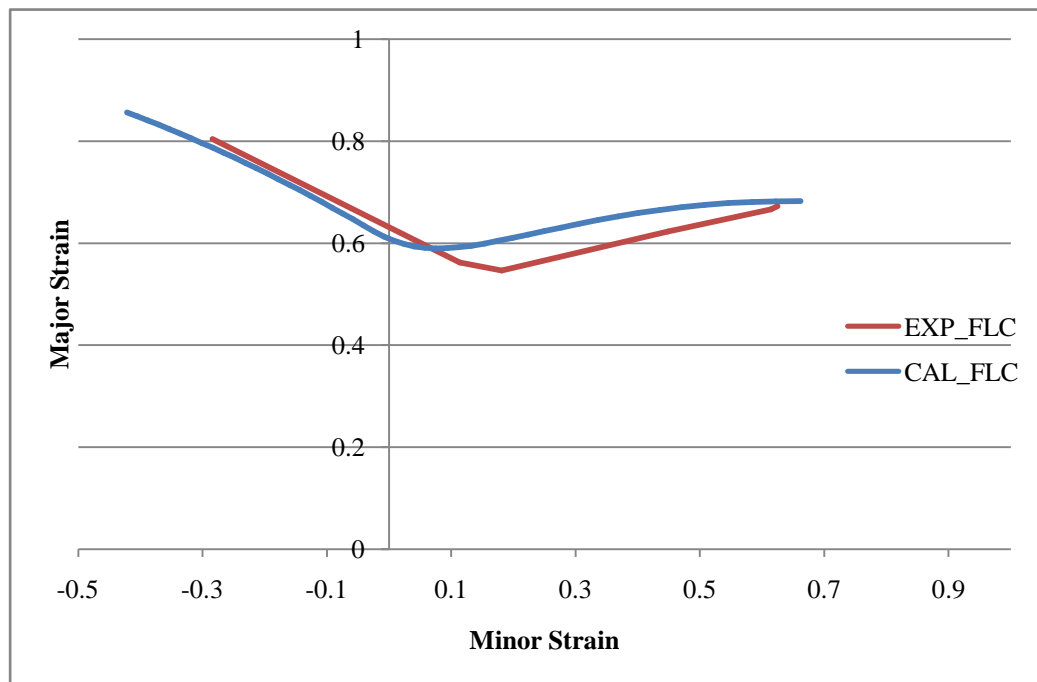


Figure 5.3. A comparison between calculated and experimental FLDs of AZ31 Mg sheet at 300 °C .

To analyze the influence of temperature and strain rate on calculated FLD, two additional FLDs were calculated, one at 300 °C with strain rate of 0.1/second, and another one at 200 °C with strain rate of 0.001/second. All 3 FLDs are shown in Figure 5.4. Since the purpose of this calculation was to gain a further insight into Shida's equation and its effectiveness for representing the FLDs of AZ31 at different temperatures and strain rates, the f-value used in all calculations was kept the same as in the earlier calculation (f=0.999). Therefore, the calculated FLD at 200 °C may not closely match the experimentally determined FLD at 200 °C. However, the results in Figure 5.4 illustrate that when the temperature is lower, not only the level of FLD but also the slope of FLD could be decreased significantly. This appears consistent with the data reported by Kim [23] and Antoniswamy [24] (see earlier Figure 1.4). Also, when the strain rate is higher at 300 °C (predicted blue curve at 0.001/second versus red curve at 0.1/second), both level and slope of the predicted FLD is decrease. This phenomenon could be explained by a decrease in strain rate sensitivity of AZ31 at higher strain rates as shown in Table 5.1. As smaller strain rate results in increased ductility for Mg sheet, it also leads to better formability.

Table 5.1. The variation of m-value with strain rate and true strain [79].

Temp. (° C)	m-value at 3 certain strain and different base strain rates					
	0.05		0.2		0.35	
	0.001	0.01	0.001	0.01	0.001	0.01
300	0.08	0	0.08	0.05	0.09	0.06
500	0.33	0.16	0.31	0.18	0.28	0.2

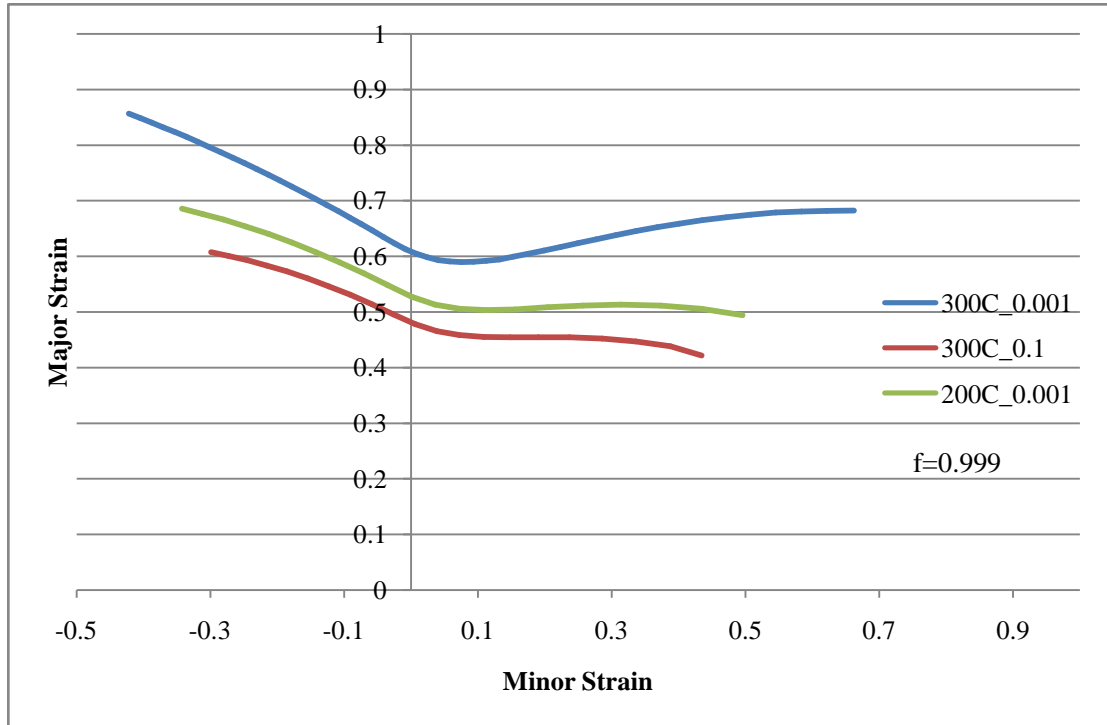


Figure 5.4. Calculated FLD for same material constants but alternative temperatures and strain rates.

5.4 High Temperature FLC Conclusions

FLD calculation methodology for room temperature was successfully modified by incorporating a strain rate and temperature dependent material hardening law to calculate FLD of AZ31 at 300°C. Good agreement was observed between the predicted and experimental FLD. The trends with respect to shape and position of the FLDs as a function of strain rate and temperature are consistent with the data from literature.

CHAPTER 6

CONCLUSIONS

In this research several experimental and theoretical studies were performed to understand the PASF method of improving formability of AZ31 Mg at room temperature. Results presented in this thesis confirm that PASF is an industrially viable method of improving the formability of AZ31 magnesium sheet at room temperature. Existing experimental and numerical methods of predicting forming limits in the literature have been expanded and adapted for the PASF process. The experimental and predicted FLCs for annealed and PASF processed materials have been compared and good agreement has been observed. Similarly, good agreement with experimental high temperature FLC data for AZ31 sheet has been obtained with the predictions made from Shida's strain rate and temperature dependent constitutive model and M-K analysis.

With respect to the 1st objective of this research following conclusions can be drawn:

1. PASF does affect the LDH value of AZ31 Mg. While two-step punch stretching in the same direction can improve the LDH value significantly, reverse punch stretching can only marginally improve the LDH value.
2. The optimum annealing temperature of 250 °C with an annealing time of 30 minutes appear to provide a suitable fully recovered and recrystallized microstructure consisting of evenly distributed uniform size grains in AZ31.

Annealing at 400°C with 2 hours results in significant grain growth and consequent reduction in formability as measured by reduced LDH value. In other words, the microstructure of AZ31 sheet has a significant influence on the formability as measured by LDH value.

With respect to the 2nd objective following conclusions can be drawn:

1. The experimental FLDs of fully annealed and pre-strain annealed AZ31 Mg at room temperature were constructed by punch stretching of specimens with different geometries.
2. A comparison of FLDs of annealed and PASF processed AZ31 magnesium sheet clearly indicate the room temperature formability improvement arising from the PASF process. The improvement in forming limit varies along the different loading paths, and typically, the maximum enhancement occurs along the equi-biaxial tension loading path.

With respect to the remaining objectives of this research, following conclusions can be drawn:

1. A modified M-K theory was coded in Matlab to incorporate the specific characteristics of AZ31 sheet such as its high r-value, PASF process, and strain softening at higher temperatures. The effects of f-value, r-value, and groove orientation on the calculated FLD were studied by comparing with results from the published literatures.
2. The calculated FLD based on modified M-K theory for fully annealed AZ31

Mg is close to the experimental FLD.

3. The calculated FLD for PASF processed AZ31 Mg is relatively close to the experimental FLD. While the shape of calculated FLD matches the experimental result, the level of calculated FLD has some deviation from the experimental results.
4. Shida's strain rate and temperature dependent constitutive equation fits the shape of the uniaxial stress-strain curve of AZ31 at 300°C quite well. This equation in conjunction with the M-K theory yields good prediction of shape and level of experimental FLD of AZ31 Mg sheet at 300°C . The trends in the shape and position of the FLDs with respect to strain rate and temperature are also consistent with the experimental data in the literature.

FUTURE WORK

Two additional activities as described below are suggested for further improving the FLD predictions for AZ31 sheet.

1. The r-value along rolling direction has been used in Hill's quadratic yield function for calculation of FLD of AZ31 sheet using the M-K method. However, it is preferable to use an average r-value in the following form:

$$\bar{r} = \frac{r_{RD} + 2r_{45} + r_{TD}}{4}$$

where r_{RD} , r_{45} and r_{TD} are strain ratios (or plastic anisotropy) along rolling and 45° and transverse to rolling directions respectively. This would entail additional measurements of r-values along transverse and 45° directions and slight modifications to the Matlab code to incorporate the average r-value. By using the average r-value in Hill's quadratic yield function, it may improve the FLD prediction compared to the experimental FLDs presented in this thesis.

2. It has been noted that both the experimental and theoretical determined FLDs have a shift in their minimum limit strain to the biaxial tension side. For experimental FLDs, the shift may be caused by the non-linear loading path due the out-of-plane (punch) and possibly due to friction between punch and sheet. For the theoretical determined FLDs assume in-plane deformation, so the shift is likely from sources other than out-of-plane deformation and friction. In the present work, r-value above unity as well as f-value are shown to cause shift in the minimum limit strain to the biaxial tension

side. However, there could be other factors as well that can that can lead to the shift.

This should be investigated.

REFERENCES

1. S. Toros, F. Ozturk, I. Kacar, *Review of warm forming of aluminum-magnesium alloys*. Journal of Materials Processing Technology, 2008. **207**: p. 1-12.
2. Kulekci, M.K., *Magnesium and its alloys applications in automotive industry*. Int. J. Adv. Manuf. Technol., 2008. **39**: p. 851-865.
3. M. Marya, L.G. Hector, R. Verma, W. Tong, *Microstructural effects of AZ31 magnesium alloy on its tensile deformation and failure behaviors*. Materials Science and Engineering A, 2006. **418**: p. 341-356.
4. L. Wang, Q. Qiao, Y. Liu, X. Song, *Formability of AZ31 Mg alloy sheets within medium temperatures*. Journal of Magnesium and Alloys, 2013. **1**: p. 312-317.
5. F. Chen, Y. Huang, *Formability of stamping magnesium-alloy AZ31 sheet*. Journal of Materials Processing Technology, 2003. **142**: p. 643-647.
6. M. Sivanandini, S.S. Dhami, B.S. Pabla, *Formability of magnesium alloys*. International Journal of Modern Engineering Research, 2012. **2-4**: p. 2464-2471.
7. S.R. Agnew, O. Duyguly, *Plastic anisotropy and the role of non-basal slip in magnesium alloy AZ31B*. International Journal of Plasticity, 2005. **21**: p. 1161-1193.
8. T. Zhou, G. Itoh, Y. Iseno, Y. Motohashi, *Deformation behavior of polycrystalline AZ31 alloy at room and elevated temperatures*. Materials Science Forum, 2005. **488-489**: p. 775-778.
9. M. Boba, M.J. Worswick, R. Mishra, J. Carter, *Formability of AZ31B and ZEK100 magnesium alloy sheets at elevated temperatures*. Mg2012: 9th International Conference on Magnesium Alloys and their Applications, 2012: p. 397-402.
10. K.F. Zhang, D.L. Yin, D.Z. Wu, *Formability of AZ31 magnesium alloy sheets at warm working conditions*. International Journal of Machine Tools & Manufacture, 2006. **46**: p. 1276-1280.
11. E. Doege, K. Droder, *Sheet metal forming of magnesium wrought alloys - formability and process technology*. Journal of Materials Processing Technology, 2001. **115**: p. 14-19.
12. R. Neugebauer, T. Altan, M. Geiger, M. Kleiner, A. Sterzing, *Sheet metal forming at elevated temperatures*. Annals of the CIRP, 2006. **55**: p. 793-816.
13. S.B. Kim, H. Huh, H.H. Bok, M.B. Moon, *Forming limit diagram of auto-body steel sheets for high-speed sheet metal forming*. Journal of Materials Processing Technology, 2011. **211**: p. 851-862.
14. S.P. Keeler, W.A. Backhofen, *Plastic instability and fracture in sheet stretched over rigid punches*. ASM Transactions, 1964. **56**: p. 25-48.
15. Goodwin, G.M., *Application of strain analysis to sheet metal forming in the press shop*. SAE paper, 1968. **No. 680093**.
16. *Metallic materials - guidelines for the determination of forming-limit-diagrams*.

International Standard. **ISO 12004-2**.

17. Hecker, S.S., *Simple technique for determine forming limit curves*. Sheet Metal Industries, 1975. **52**: p. 671-676.
18. T. Kikuma, K. Nakazima, *Effects of deforming conditions and mechanical properties on the stretch forming limits of steel sheet*. Proc. ICSTIS, Suppl. Trans. ISIJ, 1971. **11**: p. 827-831.
19. Z. Marciniak, K. Kuczinski, T. Pokora, *Influence of the plastic properties of the material on the forming limit diagram for sheet metal tension*. Int. J. Mech. Sci., 1973. **15**: p. 789-805.
20. Z. Marciniak, K. Kuczynski, *Limit strains in the processes of stretch-forming sheet metal*. International Journal of Mechanical Sciences, 1967. **9**: p. 609-620.
21. Raghavan, K.S., *A simple technique to generate in-plane forming limit curves and selected applications*. Metallurgical and Materials Transactions A, 1995. **26A**: p. 2075-2084.
22. B.L. Mordike, T. Ebert, *Magnesium properties - applications - potential*. Materials Science & Engineering A, 2001. **302**: p. 37-45.
23. H.J. Kim, S.C. Choi, K.T. Lee, H.Y. Kim, *Experimental determination of forming limit diagram and springback characteristics of AZ31B Mg alloy sheets at elevated temperatures*. Materials Transactions, 2008. **49**(5): p. 1112-1119.
24. A.R. Antoniswamy, A.J. Carpenter, J.T. Carter, L.G. Hector, E.M. Taleff, *Forming-limit diagrams for magnesium AZ31B and ZEK 100 alloy sheets at elevated temperatures*. ASM International JMEPEG, 2013. **22**: p. 3389-3397.
25. N. Abedrabbo, F. Pourboghrat, J. Carsley, *Forming of aluminum alloys at elevated temperatures - part 2: numerical modeling and experimental verification*. International Journal of Plasticity, 2006. **22**: p. 342-373.
26. Q. Situ, M.K. Jain, D.R. Metzger, *Determination of forming limit diagrams of sheet materials with a hybrid experimental-numerical approach*. International Journal of Mechanical Sciences, 2011. **53**: p. 707-719.
27. X. Duan, M.K. Jain, D.S. Wilkinson, *Development of a heterogeneous microstructurally based finite element model for the prediction of forming limit diagram of sheet metal*. Metallurgical and Materials Transactions A, 2006. **37A**: p. 3489-3501.
28. C.J. Neil, S.R. Agnew, *Crystal plasticity-based forming limit prediction for non-cubic metals: application to Mg alloy AZ31B*. International Journal of Plasticity, 2009. **25**: p. 379-398.
29. H. Wang, P.D. Wu, K.P. Boyle, K.W. Neale, *On crystal plasticity formability analysis for magnesium alloy sheets*. International Journal of Solids and Structures, 2011. **48**: p. 1000-1010.
30. M.K. Jain, J. Allin, X. Duan, D.J. Lloyd, *Effect of reverse dome stretching on dome height and forming limits of sheet materials*. Materials Science and Engineering A, 2005. **390**: p. 210-216.

31. C. Peng, W. Peng, P. Li, *Influence of annealing on tensile property and microstructure of AZ31 Magnesium Alloy*. Special Casting & Nonferrous Alloys, 2006. **26**(10): p. 661-663.
32. *Appendix F - Grain Size Determination*.
33. H. Zhang, G. Huang, J. Lin, L. Wang, *Influence of annealing temperature on microstructure and properties of warm-rolled AZ31 magnesium alloy sheets*. Materials Science Forum, 2013. **747-748**: p. 352-358.
34. S. Liang, P. Okrutny, X. Wang, H.S. Zurob, *Recrystallization nucleation sites in deformed AZ31*. Mg2012: 9th International Conference on Magnesium Alloys and their Applications, 2012: p. 663-668.
35. G.J. Griffiths, J. Robson, B. Davis, *Forming limit diagrams for Mg alloy ZEK100 in different microstructural conditions*. Mg2012: 9th International Conference on Magnesium Alloys and their Applications, 2012: p. 539-544.
36. J. Scott, M.P. Miles, D. Fullwood, B.L. Adams, A. Khosravani, R.K. Mishra, *Microstructure evolution of alloy AZ31B sheet at mildly elevated temperatures for different strain conditions*. Mg2012: 9th International Conference on Magnesium Alloys and their Applications, 2012: p. 391-396.
37. L.L. Chang, E.F. Shang, Y.N. Wang, X. Zhao, M. Qi, *Texture and microstructure evolution in cold rolled AZ31 magnesium alloy*. Materials Characterization, 2009. **60**: p. 487-491.
38. K. Nakajima, T. Kikuma, K. Hasuka, *Study on the Formability of Steel Sheets*. Yczwata Technical Report, 1968. **264**: p. 141-154.
39. R.K. Sahu, S. Majumdar, B.N. Prasad, *Forming limit diagram of high strength steel sheet (DP-590)*. MIT International Journal of Mechanical Engineering, 2011. **1**(2): p. 114-118.
40. J.T. Carter, R.K. Mishra, *Two-step forming with intermediate annealing of ZEK100 alloy sheet*. 9th International Conference on Magnesium Alloys and their Applications, 2012: p. 695-702.
41. Schenk, T., *Introduction to Photogrammetry*. 2005.
42. *ARAMIS – Optical 3D Deformation Analysis*. 2014.
43. Jain, M.K., *Formability enhancements of automotive CC and DC magnesium sheet materials using pre-strain annealing technology (Milestone 3)*. Project Report Submitted to General Motors of Canada, Ltd, 2012.
44. K. Yoshida, T. Kuwabara, M. Kuroda, *Path-dependence of the forming limit stresses in a sheet metal*. International Journal of Plasticity, 2007. **23**: p. 361-384.
45. M.N. Mekonen, D. Steglich, J. Bohlen, L. Stutz, D. Letzig, J. Mosler, *Experimental and numerical investigation of Mg alloy sheet forming*. Materials Science & Engineering A, 2013. **586**: p. 204-214.
46. A.A. Zadpoor, J. Sinke, R. Benedictus, *Formability prediction of high strength aluminum sheets*. International Journal of Plasticity, 2009. **25**: p. 2269-2297.
47. Z. Marciniak, J.L. Duncan and S.J. Hu, *Mechanics of sheet metal forming*. 2002.

Second edition (2002) ISBN: 978-0-7506-5300-8.

48. A.S. Khan, M. Baig, *Anisotropic response, constitutive modeling and the effects of strain-rate and temperature on the formability of an aluminum alloy*. International Journal of Plasticity, 2011. **27**: p. 522-538.
49. J. Lian, B. Baudelet, *Forming limit diagram of sheet metal in the negative minor strain region*. Materials Science and Engineering, 1987. **86**: p. 137-144.
50. M. Ganjiani, A. Assempour, *An improved analytical approach for determination of forming limit diagrams considering the effects of yield functions*. Journal of Materials Processing Technology, 2007. **182**: p. 598-607.
51. S.H. Choi, D.H. Kim, H.W. Lee, B.S. Seong, K. Piao, R. Wagoner, *Evolution of the deformation texture and yield locus shape in an AZ31 Mg alloy sheet under uniaxial loading*. Materials Science and Engineering A, 2009. **526**: p. 38-49.
52. M.O. Andar, T. Kuwabara, D. Steglich, *Material modeling of AZ31 Mg sheet considering variation of r-values and asymmetry of the yield locus*. Materials Science and Engineering A, 2012. **549**: p. 82-92.
53. F. Barlat, D.J. Lege, J.C. Brem, *A six-component yield function for anisotropic materials*. International Journal of Plasticity, 1991. **7**: p. 693-712.
54. Hill, R., *Constitutive modelling of orthotropic plasticity in sheet metals*. J. Mech. Phys. Solids, 1990. **38**(3): p. 405-417.
55. Stoughton, T.B., *A general forming limit criterion for sheet metal forming*. International Journal of Mechanical Sciences, 2000. **42**: p. 1-27.
56. O. Cazacu, B. Plunkett, F. Barlat, *Orthotropic yield criterion for hexagonal closed packed metals*. International Journal of Plasticity, 2006. **22**: p. 1171-1194.
57. R. Boissiere, P. Vacher, J.J. Blandin, A. Khelil, *Strain capacities limits of wrought magnesium alloys: tension vs. expansion*. Materials Sciences and Applications, 2013. **4**: p. 768-772.
58. M.G. Lee, R.H. Wagoner, J.K. Lee, K. Chung, H.Y. Kim, *Constitutive modeling for anisotropic/asymmetric hardening behavior of magnesium alloy sheets*. International Journal of Plasticity, 2008. **24**: p. 545-582.
59. M.C. Butuc, J.J. Gracio, A. Barata da Rocha, *A theoretical study on forming limit diagrams prediction*. Journal of Materials Processing Technology, 2003. **142**: p. 714-724.
60. J. Kang, D.S. Wilkinson, R.K. Mishra, W. Yuan, R.S. Mishra, *Effect of inhomogeneous deformation on anisotropy of AZ31 magnesium sheet*. Materials Science & Engineering A 2013. **567**: p. 101-109.
61. M.K. Jain, D.J. Lloyd, S.R. Macewen, *Hardening laws, surface roughness and biaxial tensile limit strains of sheet aluminum alloys*. Int. J. Mech. Sci., 1996. **38**(2): p. 219-232.
62. A. Graf, W.F. Hosford, *Calculations of forming limit diagrams*. Metallurgical and Materials Transactions A, 1990: p. 87-94.
63. K.S. Chan, D.A. Koss, A.K. Ghosh, *Localized necking of sheet at negative minor*

- strains. Metallurgical Transactions A, 1984. **15A**: p. 323-329.
64. Gdoutos, E.E., *Fracture Mechanics*. 2005. **Second edition ISBN 1-4020-3153-X**: p. 61.
 65. G. Mitukiewicz, K. Anantheshwara, G. Zhou, R.K. Mishra, M.K. Jain, *A new method of determining forming limit diagram for sheet materials by gas blow forming*. Submitted to Journal of Material Processing Technology, November 2013.
 66. M. Merklein, W. Hubnatter, M. Geiger, *Characterization of yield behavior of sheet metal under biaxial stress condition at elevated temperatures*. CIRP Annals - Manufacturing Technology, 2008. **57**: p. 269-274.
 67. W. Hubnatter, M. Merklein, M. Geiger, *Influence of temperature on yield loci of magnesium alloy*. Proceedings of the LANE 2007, 2007: p. 519-532.
 68. T. Naka, T. Uemori, R. Hino, M. Kohzu, K. Higashi, F. Yoshida, *Effects of strain rate, temperature and sheet thickness on yield locus of AZ31 magnesium alloy sheet*. Journal of Materials Processing Technology, 2008. **201**: p. 395-400.
 69. S.I. Kim, Y. Lee, S.M. Byon, *Study on constitutive relation of AISI 4140 steel subject to large strain at elevated temperatures*. Journal of Materials Processing Technology, 2003. **140**: p. 84-89.
 70. Shida, S., *Empirical formula of flow stress of carbon steels-resistance to deformation of carbon steels at elevated temperature*. 2nd Report, J. JSTP, 1969. **10**: p. 610-617.
 71. J. Guo, S. Zhao, R. Murakami, R. Ding, S. Fan, *Modeling the hot deformation behavior of Al alloy 3003*. Journal of Alloys and Compounds, 2013. **566**: p. 62-67.
 72. J. Luo, M. Li, X. Li, Y. Shi, *Constitutive model for high temperature deformation of titanium alloys using internal state variables*. Mechanics of Materials, 2010. **42**: p. 157-165.
 73. X. Chen, G. Chen, M. Sakane, *Modified Anand constitutive model for lead-free solder Sn-3.5Ag*. Inter Society Conference on Thermal Phenomens, 2014: p. 447-452.
 74. Klepaczko, J.R., *A practical stress-strain-strain rate-temperature constitutive relation of the power form*. Journal of Mechanical Working Technology, 1987. **15**: p. 143-165.
 75. Y.Q. Cheng, H. Zhang, Z.H. Chen, K.F. Xian, *Flow stress equation of AZ31 magnesium alloy sheet during warm tensile deformation*. Journal of Materials Processing Technology, 2008. **208**: p. 29-34.
 76. M.N. Mekonen, D. Steglich, J. Bohlen, D. Letzig, J. Mosler, *Mechanical characterization and constitutive modeling of Mg alloy sheets*. Materials Science and Engineering A, 2012. **540**: p. 174-186.
 77. Y. Peng, Y. Luo, D. Li, J. Yin, *Constitutive model development and the numerical study on the drawability of AZ31 sheet*. Materials Science Forum, 2005. **488-489**: p. 645-648.

78. W.H. Wu, Y. Lou, *Flow stress constitutive equation of AZ31 magnesium alloy for hot compression*. Advanced Materials Research, 2011. **328-330**: p. 1614-1618.
79. E. Karimi, A. Zarei-Hanzaki, M.H. Pishbin, H.R. Abedi, P. Changizian, *Instantaneous strain rate sensitivity of wrought AZ31 magnesium alloy*. Materials and Design, 2013. **49**: p. 173-180.